Universitat Autònoma de Barcelona

Low Gain Avalanche Detectors for the ATLAS High Granularity Timing Detector

Chiara Grieco

Low Gain Avalanche Detectors for the ATLAS High Granularity Timing Detector

Author:
Chiara Grieco

Supervisors:
Sebastian Grinstein
María del Pilar Casado Lechuga
Lucía Castillo García

Tutor:
María del Pilar Casado Lechuga

Ph.D. Thesis
June 2022

Institut de Física d'Altes Energies
EXCELENCIA SEVERO OCHOA
BIST Barcelona Institute of Science and Technology
Universitat Autònoma de Barcelona

"Colui che non sa niente, non ama niente.

Colui che non fa niente, non capisce niente.

Colui che non capisce niente è spregevole.

Ma colui che capisce, ama, vede, osserva...

La maggiore conoscenza è congiunta indissolubilmente all'amore...

Chiunque crede che tutti i frutti maturino contemporaneamente come le fragole,

non sa nulla dell'uva."

Paracelso

We are obsessed with ourselves. We study our history, our phsychology, our phylosopy, our gods. Much of our knownledge revolves aroud man himself, as if we were the most important thing in the universe.
I think I like physics because it opens a window through which we can see further. It gives me the sense of fresh air entering the house.

Carlo Rovelli

A Clara e Teresa.
Luogo sicuro della mia anima,
dove ritrovare me stessa ogni volta
dopo essermi persa.

Abstract

The Large Hadron Collider (LHC) at the European Organization for Nuclear Research (CERN), Geneva, will interrupt its operation in 2026, after the current Run 3, to be upgraded to the High Luminosity LHC (HL-LHC), providing $p-p$ collisions with a center of mass energy $\sqrt{s}$ =14 TeV and a luminosity of $7.5 \times 10^{34}\text{cm}^{-2}\text{s}^{-1}$.

A Toroidal LHC ApparatuS (ATLAS) is one of the two general purpose experiments at the LHC, will have to be upgraded in order to meet the requirements given by the larger luminosity. Among the several upgrades of the ATLAS sub-detectors, the current Inner Detector will be fully replaced by the Inner Tracker (ITk), based on silicon detectors with a finer granularity and improved radiation hardness. A second detector, the High Granularity Timing Detector (HGTD), will provide timing information of tracks and vertices.

The combination of the ITk and HGTD measurements will make possible the resolution of vertices close in space but separated in time, improving the ATLAS reconstruction performances. In the context of this thesis, a preliminary simulation study was carried out in order to understand the impact of the HGTD on the Vector Boson Fusion (VBF) analyses.

In this thesis the Low Gain Avalanche Detector (LGAD) technology, with which the HGTD detector will be instrumented, will be described. This technology consists of planar n-on-p silicon detectors with highly doped *p-type* electrode designed to increase the sensor gain through impact ionization. Thin LGAD sensors have shown a time resolution of about 30 ps on the detection of minimum ionization particles and this technology has been chosen as the baseline for the sensors of the HGTD detector. Studies of LGAD sensors produced with different approaches both before and after irradiation were performed in the context of this thesis.

Resumen

El Large Hadron Collider (LHC) de l'Organització Europea per a la Recerca Nuclear (CERN), Ginebra, interromprà el seu funcionament el 2026, després de l'actual Run 3, per actualitzar-se al High Luminosity LHC (HL-LHC), proporcionant $p-p$ col·lisions amb un centre d'energia de massa $\sqrt{s}$ =14 TeV i una lluminositat de 7,5 $\times$ $10^{34}\text{cm}^{-2}\text{s}^{-1}$.

A Toroidal LHC ApparatuS (ATLAS) és un dels dos experiments de propòsit general a l'LHC, s'haurà d'actualitzar per tal de complir els requisits donats per la major lluminositat. Entre les diverses actualitzacions dels subdetectors ATLAS, el detector interior actual serà completament substituït per l'Inner Tracker (ITk), basat en detectors de silici amb una granularitat més fina i una duresa de radiació millorada. Un segon detector, el High Granularity Timing Detector (HGTD), proporcionarà informació de cronometratge de pistes i vèrtexs.

La combinació de les mesures ITk i HGTD farà possible la resolució de vèrtexs propers a l'espai però separats en el temps, millorant les prestacions de reconstrucció d'ATLAS. En el context d'aquesta tesi, es va dur a terme un estudi de simulació preliminar per tal d'entendre l'impacte de l'HGTD en les anàlisis de Vector Boson Fusion (VBF).

En aquesta tesi es descriu la tecnologia Low Gain Avalanche Detector (LGAD), amb la qual s'equiparà el detector HGTD. Aquesta tecnologia consisteix en detectors planars de silici n-on-p amb un elèctrode *p-type* altament dopat dissenyat per augmentar el guany del sensor mitjançant la ionització d'impacte. Els sensors LGAD prims han mostrat una resolució temporal d'aproximadament 30 p en la detecció de partícules d'ionització mínima i aquesta tecnologia s'ha escollit com a línia de base per als sensors del detector HGTD. En el context d'aquesta tesi es van realitzar estudis de sensors LGAD produïts amb diferents enfocaments tant abans com després de la irradiació.

Contents

Introduction **1**

A new generation of semiconductor detector for High Energy Physics 1

1 The LHC accelerator complex **5**

1.1 Upgrade for HL-LHC 7

2 The ATLAS experiment **9**

2.1 Overview of the ATLAS detector 9

2.1.1 Inner detector 10

2.1.2 Calorimeters 13

2.1.3 Muon Spectrometer 16

2.1.4 Magnets 19

2.1.5 Forward detectors 21

2.1.6 Trigger System 23

2.2 ATLAS upgrade for HL-LHC 23

2.2.1 Inner Tracker 24

2.2.2 High Granularity Timing Detector 29

3 The High Granularity Timing Detector **31**

3.1 Physics motivation 32

3.1.1 Track to vertex association 33

3.1.2 Suppression of pile up jets 36

3.1.3 Lepton track isolation . . . 37
3.1.4 Other applications . . . 38
3.2 HGTD as a luminometer . . . 39
3.3 The HGTD detector . . . 41
3.3.1 Detector overview and requirements . . . 41
3.3.2 Detector Layout . . . 43
3.3.3 Time resolution . . . 45
3.3.4 Radiation hardness . . . 47
3.4 HGTD module . . . 49
3.5 Front-end electronics . . . 50
3.5.1 General ASIC requirements . . . 51
3.5.2 Contribution to the time resolution . . . 53
3.5.3 Single-channel readout electronics . . . 54
3.6 Sensors . . . 59

4 HGTD impact on VBF H analyses at HL-LHC 61
4.1 The Standard Model in a nutshell . . . 61
4.1.1 Standard Model particle content . . . 62
4.1.2 Open questions of the Standard Model . . . 65
4.2 Impact of the HGTD in physics analysis . . . 65
4.2.1 Vector Boson Fusion Higgs production . . . 66
4.2.2 Monte Carlo sample production . . . 68

5 Sensor Technology: from Solid State Detectors to Low Gain Avalanche Detectors (LGADs) 77
5.1 Solid State Detectors . . . 78
5.1.1 The band model . . . 78
5.1.2 Addition of doping materials . . . 80
5.1.3 The *pn*-junction . . . 82

5.2 Silicon detectors 85
5.2.1 Signal generation by photons 89
5.2.2 Detector Applications 90
5.2.3 Radiation damage 92
5.3 **L**ow **G**ain **A**valanche **D**etectors (LGADs) 97
5.3.1 Why low gain? 99
5.3.2 Why thin sensors? 100
5.3.3 Major effects on the time resolution 101
5.3.4 LGADs for the HGTD 102
5.3.5 CNM Production runs 102

6 Performance results for LGAD sensors before and after irradiation 105

6.1 Setups 106
6.1.1 Setup for measurements with ^{90}Sr β source 106
6.1.2 Transient Current Tecnique setup 110
6.1.3 Test beam setup 111
6.2 Investigation of CNM LGAD production with Boron, Boron plus Carbon and Gallium doping material 113
6.2.1 Electrical characterization and stability measurements 113
6.2.2 Measurements with ^{90}Sr β source 114
6.2.3 Transient Current Technique (TCT) measurements for Boron and Gallium doped single pad LGAD sensors 116
6.2.4 Performance in beam test 119
6.2.5 Conclusions 122
6.3 Characterization of Si-on-Si wafer LGAD sensors from CNM run 12916 124
6.3.1 IV, CV and Stability measurements 124
6.3.2 Measurements with ^{90}Sr β source 128
6.3.3 Inter pad distance of 2 $\times$ 2 B doped LGAD arrays 131
6.3.4 Conclusions and Outlook 135

6.4 Characterization of low resistivity epitaxial wafer LGAD sensors from CNM run 13002 136

6.4.1 IV, CV and stability measurements 136

6.4.2 Characterization with ^{90}Sr β source 140

6.4.3 Gain and time resolution measurements with TCT 142

6.4.4 Conclusions and comparison of results with Si-on-Si sensors . . 142

6.5 Outlooks 143

Conclusions and Outlook **145**

A Transient Current Technique **149**

Bibliography **155**

List of abbreviations and acronyms **167**

Introduction

A new generation of semiconductor detector for High Energy Physics

The Standard Model (SM) of particle physics describes accurately the interactions between particles through three of the four fundamental forces: the electromagnetic, the weak and the strong force, leaving out the gravitational one. Since its formulation, the SM has been validated through several discoveries, such as discoveries of heavy quarks (*bottom*, *top* and *charm*), the Z and $W^{\pm}$ bosons and gluons, whose properties were predicted by this model.

The last missing particle of the SM puzzle was the Higgs boson, finally observed for the first time by the A Toroidal LHC ApparatuS (ATLAS) and the Compact Muon Solenoid (CMS) experiments at the Conseil Europeen pour la recherche Nucleaire (CERN) Large Hadron Collider (LHC) in 2012 [1, 2].

There are still several open questions that the SM as it is cannot answer. A wide spectrum of models has been proposed from theoretical physicist to expand the SM, the so called Beyond the Standard Model (BSM) theories, with the purpose to address the open questions, such as gravity, dark matter and the observed neutrino masses.

It is expected that at the end of the LHC lifetime the statistical uncertainties will be the major contribution to the total uncertainty in the measurements of rare

phenomena. For this reason, the LHC will be upgraded to the High Luminosity LHC (HL-LHC), where the instantaneous luminosity will be about 7 times larger than the LHC design luminosity. An introduction on the LHC accelerator complex and its upgrade to the HL-LHC will be given in Chapter 1 of this thesis.

As the LHC is improved, also the experiments will have to be upgraded, in order to cope with the higher rate of particles. A description of the ATLAS detector will be given in Chapter 2, together with a general view of the upgrade for the HL-LHC. The upgraded Inner Tracker (ITk) detector will be briefly presented, together with its track reconstruction performances. However, the upgraded tracker will have limited resolution power in the forward region where an additional detector will be needed.

The HL-LHC luminosity increase will cause a large number of additional $p - p$ collisions (pileup) that have a determinate effect on the physical performance of ATLAS. To disentangle the primary interaction from the pileup event ATLAS plan to exploit the time information of the tracker with a High Granularity Timing Detector (HGTD).

The HGTD system, based on the Low Gain Avalanche Detector (LGAD) technology, will be installed in the forward region of the ATLAS experiment, with the main aim of reducing the number of pileup tracks and jets. The LGAD technology is a very recent sensor development that provides silicon devices for High Energy Physics with a timing resolution of , high granularity (a pitch of 1 mm), and with substantial radiation hardness. The HGTD will be described in detail in Chapter 3. The physics motivation of the detector will be introduced, a detailed description of detector requirements, layout and components will be given.

The HGTD aims to improve the physics performance of ATLAS in the forward region. This means that HGTD should have a positive impact on the Vector Boson Fusion (VBF) analyses. In the context of this thesis, preliminary simulation studies were carried out on the VBF $H \to \tau\tau$ process. These are presented in Chapter 4.

The HGTD detector will be instrumented with LGAD sensors, which are silicon detectors. Chapter 5 will be dedicated to the explanation of the basic principle of solid state detectors and to the description of silicon detectors in particular, considering especially their behaviour after irradiation. In the second part of the chapter, the LGAD technology will be described and an overview of the sensors which have been studied will be presented.

In Chapter 6, the core of this thesis work, the characterization and performance of the LGAD sensor fabricated at the Centro Nacional de Micróelectronica (CNM) are presented. In an attempt to improve the LGAD performance, several approaches and production were studied. The electrical characterization, time resolution, hit reconstruction efficiency and device stability of the sensor are presented. The measurements were conducted at the Institut de Fisica d'Altes Energies (IFAE) and CNM laboratories and in various test beams at CERN and Deutsches Elektronen-Synchrotron (DESY).

Finally, the work is discussed and the outlook presented in the conclusions.

Chapter 1

The LHC accelerator complex

The LHC [3] accelerator is located at the European Organization for Nuclear Research (CERN) in Geneva, Switzerland. The accelerator complex is a succession of machines that accelerate particles to increasingly higher energies. Each machine boosts the energy of a beam of particles before injecting it into the next machine in the sequence. The LHC became operational in September 2008, and is the last element in this chain, see Figure 1.1. The LHC is made up of a 27 km ring of superconducting magnets with a number of accelerating components along the way to raise the energy of the particles. Protons are accelerated at a speed close to the speed of light in bunches of 10^{11} particles with a 25 ns separation, in two different beam pipes which are kept at ultralight vacuum. The two particle beams run in opposite directions. A strong magnetic field maintained by the superconducting electromagnets guides the beams around the accelerator ring. The electromagnets are made up of coils of a special electric cable that operates in a superconducting condition, allowing electricity to flow without resistance or energy loss. This necessitates cooling the magnets to a temperature of $-271.3\,^{\circ}\mathrm{C}$, which is colder than the outer space. To cool the magnets and other supply services, a big part of the accelerator is connected to a liquid helium distribution system. To steer the beams around the accelerator, tens of thousands of magnets of various types and sizes are used. The beams are bent

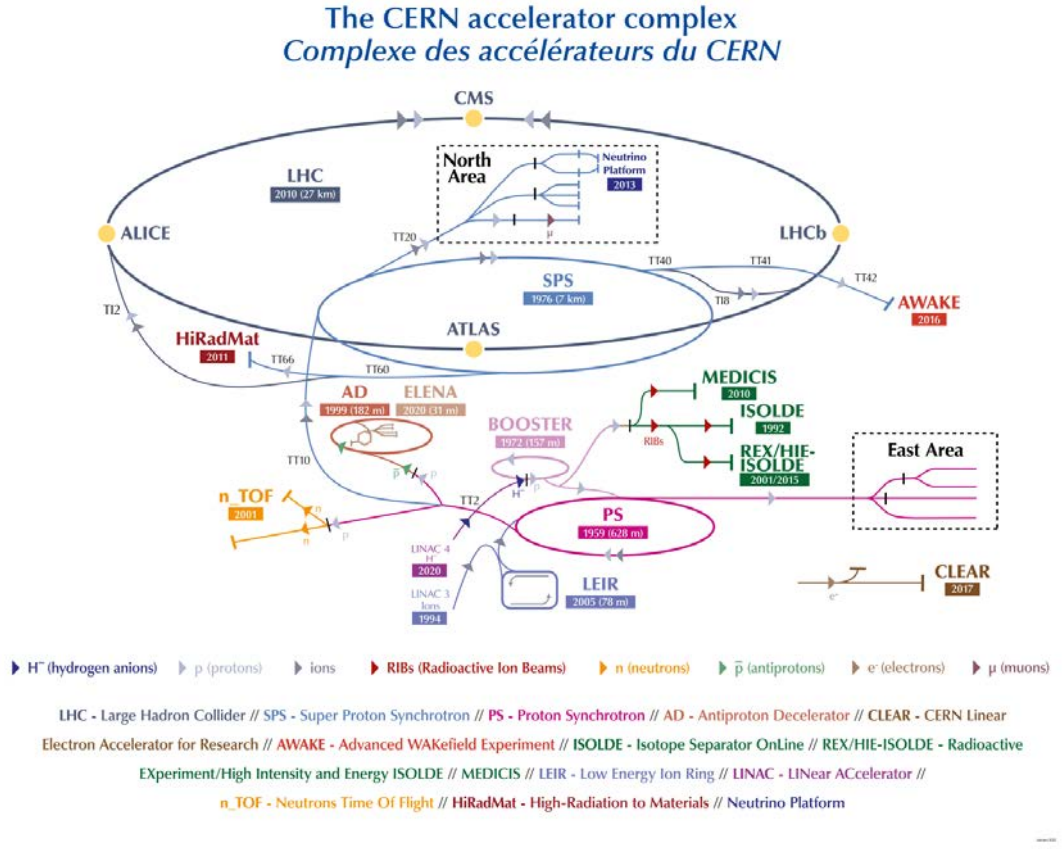

Figure 1.1: Schematic of the Large Hadron Collider accelerator complex [3].

by 1232 dipole magnets with a length of 15 m each, while they are focused by 392 quadrupole magnets with a length of 5-7 m each, generating a magnetic field of 8.3 T. Another sort of magnet is employed just before the collision to "squeeze" the particles closer together and improve the odds of collision. In the LHC, proton collision are generated at 40 MHz with a center of mass energy of 14 TeV at the design luminosity of 10^{34} $\mathrm{cm}^{-2}\mathrm{s}^{-1}$. Heavy ions collisions are also provided in the LHC, at 5.5 TeV per nucleon pair at a luminosity of $10^{27}\mathrm{cm}^{-2}\mathrm{s}^{-1}$. The beams inside the LHC are then made to collide at four points around the accelerator ring, which correspond to the location of the four bix experiments: ATLAS [4], CMS [5], A Large Ion Collider Experiment (ALICE) [6], and Large Hadron Collider beauty (LHCb) [7]. The ATLAS and the CMS are two multipurpose experiments placed at the two opposite sides of the LHC ring. Both experiments look at final states of p-p and heavy ions collisions

searching for new physics and to perform precise measurements of the SM parameters. ALICE is a detector dedicated to heavy-ion physics at the LHC. It is designed to study the physics of strongly interacting matter at extreme energy densities, where a phase of matter called quark-gluon plasma forms. The LHCb experiment investigates the differences between matter and antimatter by studying the "beauty"particle, or "b quark".

1.1 Upgrade for HL-LHC

The LHC restarted its operation at the beginning of 2022 after a mainteinance period where its experiments have been upgraded to "Phase 1"and are now ready to take data for a period of 4 years (Run 3). It will remain the most powerful accelerator in the world for at least the next two decades. To maintain scientific progress and to exploit the machine's full capacity, the LHC luminosity will be increased by a factor of $\sim$7 in what is called the Phase-II upgrade. The HL-LHC [8, 9, 10] era is foreseen to start in 2029. It will provide a revolutionary machine configuration, which will rely on a number of critical innovative technologies that constitute outstanding technological challenges. These include cutting-edge 11-12 T superconducting magnets, very small superconducting cavities for beam rotation with ultra-precise phase control, revolutionary beam collimation technology, and high-power superconducting links with low energy dissipation. The HL-LHC targets to reach a peak luminosity of 7.5×10^{34} cm^{-2}s^{-1} and an integrated luminosity of 250 fb^{-1} every year. In its entire lifetime, see Figure 1.2, the HL-LHC aims to collect up to 4000 fb^{-1}, which is almost ten times the luminosity reached for LHC in its first twelve years.

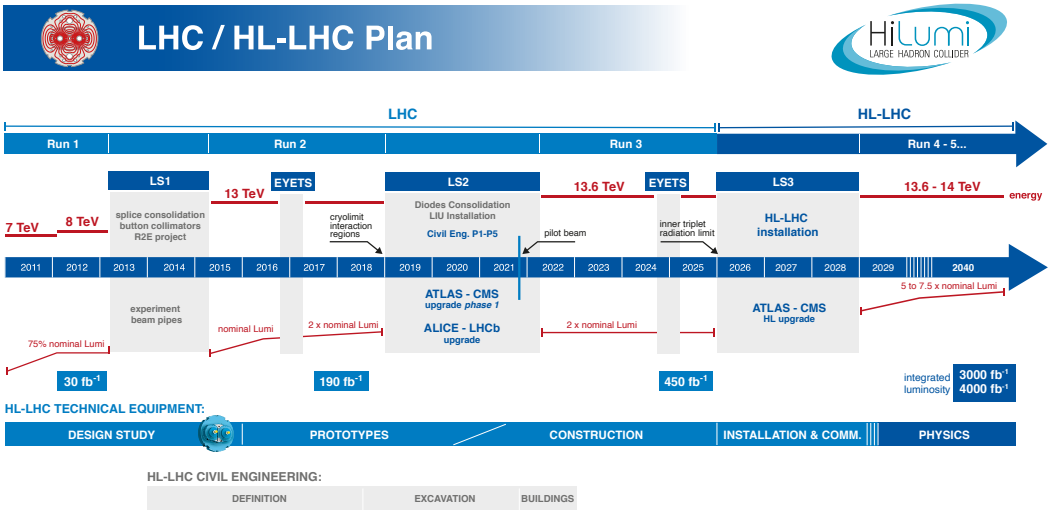

Figure 1.2: HL-LHC timeline updated in January 2022[11].

Chapter 2

The ATLAS experiment

2.1 Overview of the ATLAS detector

ATLAS is a general purpose detector located about 100 m underground at the interaction point 1 of the LHC. It has a shell-like structure and it has cylindrical and forward-backward symmetry with respect to the interaction point. Each detector component correspond to a specific sub-detector for tracking of charged particles, electromagnetic and hadronic calorimetry and muon detection. The entire detector has a length of 44 m and a diameter of 25 m for a total weight of 7000 kg, for which a sketch is shown in Figure 2.1. ATLAS has a magnet system which consists of a superconducting solenoid surrounding the inner detector cavity, and three large superconducting toroids, two at the end-caps and one barrel around the calorimeters. The detector uses a right-hand coordinate system with its origin in the nominal interaction point. The beam direction defines the $z-$axis and the plane $x-y$ is transverse to the beam. The positive direction of the $x-$axis is pointing to the centre of the LHC ring, while for the $y-$axis it is pointing upwards. The side A of the detector defines the positive $z-$axis and the side C the negative one. The azimuthal angle, ϕ, is measured around the beam axis and the polar angle, θ, is the angle from the beam

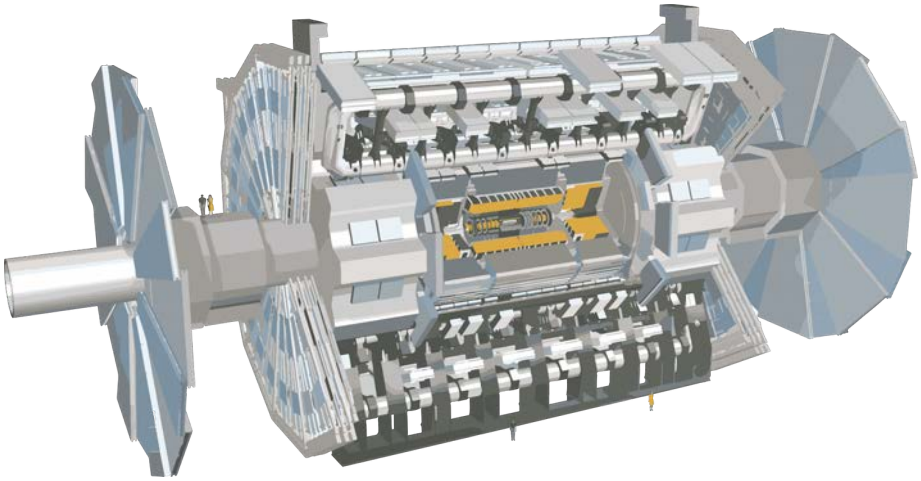

Figure 2.1: Cut-away view of the ATLAS detector. Its dimensions are 25 m in height and 44 m in length for a total weight of 7000 kg [4].

axis. The pseudorapidity is defined as $\eta = -ln\ tan(\theta/2)$. The transverse momentum, p_T, the transverse energy, E_T and the missing transverse energy, E_T^{miss}, are defined in the $x-y$ plane. The distance, ΔR, in the pseudorapidity-azimuthal space is defined as $\Delta R = \sqrt{\Delta\eta^2 + \Delta\phi^2}$ [4].

2.1.1 Inner detector

The Inner Detector (ID) is the most internal ATLAS detector system. It is designed to provide robust pattern recognition, excellent momentum resolution and primary and secondary vertex measurements for charged tracks produced in the $p-p$ collisions above a p_T threshold (nominally 0.5 GeV) and within the pseudorapidity region $|\eta| < 2.5$. It is immersed in a solenoidal magnetic field of 2 T which bends the particle trajectory giving information on their momentum. The layout of the ATLAS ID is shown in Figure 2.2 and it consists of three sub-detectors: the Pixel Detector [12] that includes the Insertable B-Layer (IBL) [13], the SemiConductor Tracker (SCT) [14] and the Trasition Radiation Tracker (TRT) [15]. The Pixel and SCT detectors provide precise track measurements at inner radii in the pseudorapidity region $|\eta| < 2.5$. The measurements from the TRT detector at larger radii provides continuous

tracking to enchance the pattern recognition and improves momentum quantification.

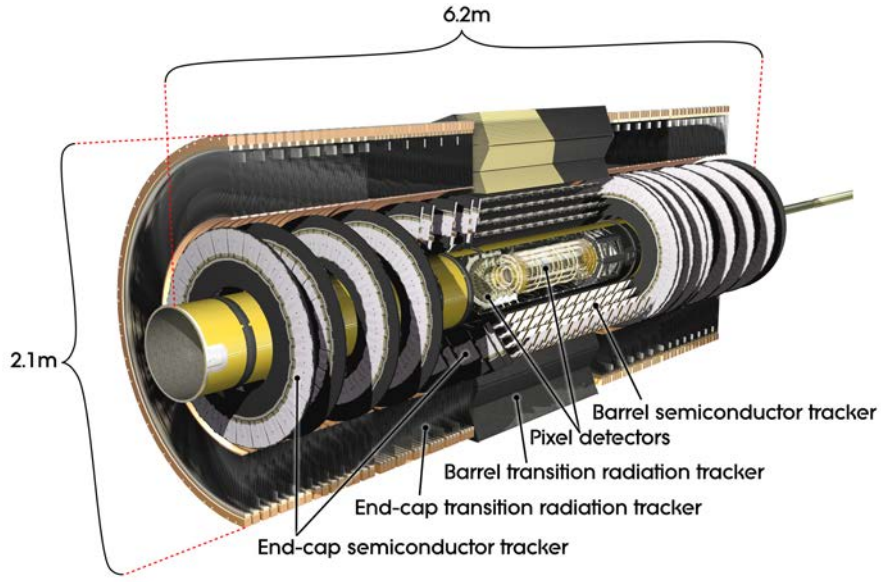

Figure 2.2: Cut-away view of the ATLAS ID [4].

Pixel Detector

Originally, the Pixel Detector consisted of three barrel layers at a radius r_1=50.5 mm, r_2=88.8 mm and r_3=122.5 mm with a length of 80 cm. Three end-cap discs are placed at the two ends of the Pixel detectors at $|z_1|$ =49.5 cm, $|z_2|$ =58.0 cm and $|z_3|$ =65.0 cm. The sensing material of the Pixel Detector are silicon sensors. The sensors are operated in the temperature range from $-5\,^{\circ}$C to $-10\,^{\circ}$C, in order to reduce leakage current, contain annealing effects and to meet charge requirements with respect to the level of irradiation. The sensors are n-in-n standard planar sensors with a pixel size of 50 μm $\times$ 400 μm. Each pixel module is made of 2×8 FE-I3 readout chips [16] bump-bonded to a sensor tile of an area of 63.4 mm $\times$ 24.4 mm and 250 μm-thick. A flexible printed circuit board connects the module with the readout system via a flex cable. In 2015, the IBL [13] was inserted as a fourth layer at a radius r=32.0 mm covering the region $|z|$ <33.2 cm. It was installed to improve the impact parameter

resolution of the detector and the robustness of the system against possible failures during operation. The central part of the IBL is made of n-in-n planar sensors, while at the ends of the barrel n-in-p 3D sensors are used. Both sensors have pixels of size 50 µm $\times$ 250 µm interconnected to a FE-I4 readout chip [17]. From beam test data, it has been calculated that the Pixel Detector has a resolution of 12 µm for normal incidence, which does not significantly degrade after irradiation. The resolution for an incidence angle of 10°-15° (expected given the IBL geometry) has been found to be 4.7 µm and 6.0 µm respectively before and after irradiation to $10^{15} \mathrm{n}_{eq}/\mathrm{cm}^2$ [18].

SemiConductor Tracker

The SCT detector consists of 4088 two-sided modules and more than 6 million readout strips. It covers an area of about 60 m^2 with silicon microstrip sensors distributed in four barrel layers and nine end-caps per side. The barrels have radii r_1=29.9 cm, r_2=37.1 cm, r_3=44.3 cm and r_4=51.4 cm and a length of 149 cm. The microstrip sensors are made of p-in-n silicon sensors. The barrel sensors have a pitch of 80 µm and the ones in the end-caps have a pitch in the range from 50.9 µm to 90.4 µm. The position of charged particles can be recorded with an accurancy of 17 µm per layer, in the transverse direction to the strips.

Transition Radiation Tracker

The TRT is a gas detector consisting of 4 mm diameter straw tubes, with 52544 straws in the barrel section with a length of 144 cm, and 122880 straws for each end-cap with a length of 39 cm, for a total volume of 12 m^3. The barrel straws cover a radius range from 56 cm< R <107 cm and the ones in the end-caps cover the interval 64 cm< R <100 cm in the region 85 cm< $|z|$ <271 cm. The straws are filled with a mixture of Xenon, Carbon Dioxide and Oxygen in percentage 70%/27%/3%. Each tube has a 31 µm diameter gold-plated Tungsten anode wire in the centre. Between

the edge of the tube and the wire there is a potential difference of 1500 V which allows the collection of ionization charges. The achieved position accurancy is 130 µm and the hit registration efficiency is 85% at a TRT operation threshold of 250-300 eV.

2.1.2 Calorimeters

Calorimeters are detectors whose aim is to measure the energy that a particle loses passing through the detector elements. In High Energy Physics (HEP) calorimeters are designed to absorb most of the energy of the particles coming from a collision, usually stopping them within their volume. Calorimeters can be homogeneous or sampling calorimeters. The first ones are made entirely of sensitive material and all the deposited energy contributes to the signal. Sampling calorimeters instead, consist of two different elements, a sensitive one which measure the energy of particles and a high density absorber material which stops them. This last approach allows to design more compact detectors but they have to be carefully calibrated in order to obtain the particle energy from the energy measured inside the sensing material, since the absorber element does not provide a measurement. Calorimeters can stop most of the known particles except muons and neutrinos. The ATLAS calorimeter system consists of three sampling calorimeter sub-detectors: the Electromagnetic, the Hadronic and the Forward calorimeters, with full ϕ-simmetry and coverage around the beam axis, and covers a pseudorapidity region $|\eta| < 4.9$. The full calorimeter system is shown in Figure 2.3.

Electromagnetic Calorimeter

The Liquid Argon (LAr) Electromagnetic CALorimeter (ECAL) [19] surrounds the ATLAS ID, measuring the energy of electrons, photons, and hadrons. It is designed to absorb the energy of electrons and photons in the range $50\,\text{MeV} < E < 3\,\text{TeV}$ and measures their impinging directions. In addition, it participates in the reconstruction

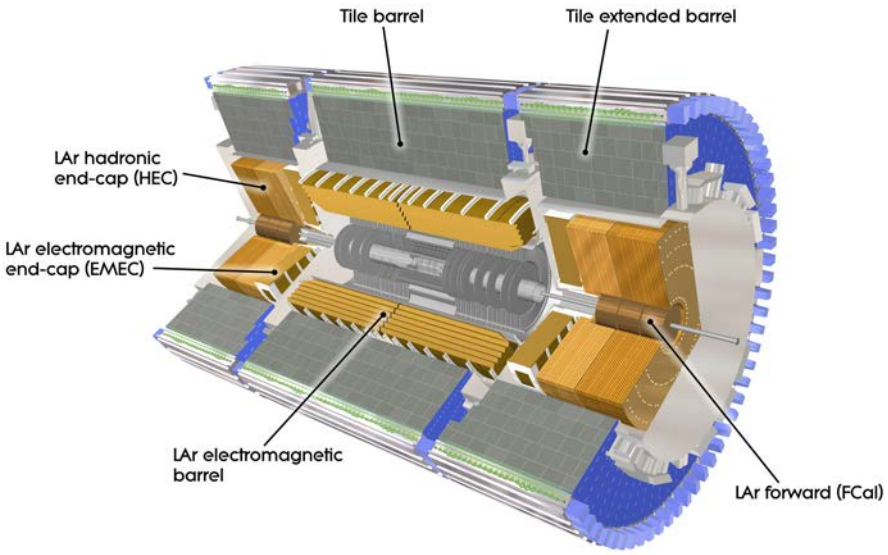

Figure 2.3: Cut-away view of the ALTAS Calorimeter system [4].

of the initial part of hadronic jets which start their shower in the electromagnetic calorimeter. The ECAL calorimeter consists of layers of tungsten, copper or lead, used as absorber, and liquid Argon, as the sensing medium. It is divided into a barrel and two ElectroMagnetic End-Cap (EMEC) components, covering the pseudorapidity range $|\eta|$ <1.475 and 1.375< $|\eta|$ <3.2 respectively, each of them housed in its cryostat. The impinging particles ionize the liquid argon sandwiched between the absorbing layers, resulting in a measurable electric current. The energy of the original particle that impacted the detector can be calculated by combining the observed currents. The calorimeter is kept at $-184\,^{\circ}\mathrm{C}$ to keep the Argon in liquid state. Electronic signals are sent from the cold liquid argon to the warm area where the readout electronics are placed via specially built, vacuum-sealed cylinders of cables. A half-barrel is made of 1024 accordion-shaped absorbers interleaved with readout electrodes, divided into 16 modules. The total thickness of each module is at least 22 radiation lengths (X_0), increasing from 22 X_0 to 30 X_0 between $|\eta|$= 0 and $|\eta|$= 0.8 (barrels) and from 24 X_0 to 33 X_0 between $|\eta|$= 0.8 and $|\eta|$= 1.3 (end-caps). This thickness ensures the full confinement of the electromagnetic showers in the calorimeter.

Hadronic Calorimeter

The Hadronic CALorimeter (HCAL) [20] samples the energy of particles which escapes the ECAL. These are usually jets with high energy originating from quark and gluon hadronization. The HCAL absorbs the remaining particles except muons which leave tracks in the muon spectrometer, and neutrinos which leave the detectors without depositing their energy. The HCAL consists of two parts: the Tile Calorimeter (TileCal) [20] in the central region and the Liquid Argon End-Cap (HEC) calorimeter in the forward region. The TileCal surrounds the LAr calorimeter and is a sampling calorimeter using steel as absorber and plastic scintillator as active medium. When a particle hits the steel layer a shower of new particles is generated. Photons are produced in the scintillator and are converted into an electric current which is proportional to the energy of the original particle. The TileCal is made of 420000 plastic scintillator and is the heaviest part of the ATLAS experiment, with a weight of about 2900 t. It covers the pseudorapidity region $|\eta| < 1.7$ with a central barrel in the $|\eta| < 1.0$ region and two extended barrels covering the region $0.8 < |\eta| < 1.7$. It extends radially from 2.28 m to 4.25 m and is split into three sections of 1.5, 4.1 and 1.8 λ[1] (interaction lengths) in the central barrel and 1.5, 2.6 and 3.3 λ in the extended barrels. The HEC calorimeter is a copper liquid-argon sampling calorimeter with a flat plate design, covering a pseudorapidity range $1.5 < |\eta| < 3.2$. It shares each of the two liquid-argon end-cap cryostats with the EMEC and the Forward Calorimeter (FCAL). It consists of two wheels with a radius of 2030 mm, each of them containing two longitudinal sections.

Forward Calorimeter

The FCAL consists of an electromagnetic calorimeter and two hadronic ones placed in a pseudorapidity range $3.1 < |\eta| < 4.9$ in order to maximize the detector acceptance

[1] λ is defined as the distance after which the number of elements of the hadronic shower is reduced by a factor $1/e$.

at low radii. Since they are located at high η, at a distance of about 4.7 m from the Interaction Point (IP), they are exposed to a high particle flux. This resulted in a design with smaller liquid-argon gaps than the 2 mm ones of the electromagnetic barrels to avoid ion build-up and to provide the highest possible density. Each FCAL is divided into three 45 cm deep modules, one electromagnetic and two hadronic. Liquid Argon is used as a detector medium and the absorber layers are Copper-based in the electromagnetic part and Tungsten-based in the hadronic ones. The depth of those calorimeters are 27.6 X_0 for the electromagnetic part and 3.62 λ and 3.55 λ for the hadronic ones.

2.1.3 Muon Spectrometer

Muons escape from barrel and end-caps calorimeters without showering, for this purpose a muon spectrometer forms the outer part of the ATLAS detector. The muon detector is designed to detect charged particles and to measure their momentum in the pseudorapidity range $|\eta| < 2.7$. It is also designed to trigger on these particles in the region $|\eta| < 2.4$. The ATLAS muon spectrometer [21] system is shown in Figure 2.4 and is composed by four sub-detectors. The Monitored Drift Tube (MDT) chambers covering the pseudorapidity range $|\eta| < 2.7$, and the Cathode-Strip Chambers (CSC) covering the range $2.0 < |\eta| < 2.7$, perform momentum measurements through the curvature of muon tracks in the magnetic field produced by toroid magnets described in Section 2.1.4. The muon spectrometer is completed by detectors capable to trigger on muon tracks: the Resistive Plate Chambers (RPC) in the barrel region ($|\eta| < 1.05$) and Thin Gap Chambers (TGC) in the end-cap ($1.05 < |\eta| < 2.4$). These two measure both coordinates of the track, both in the bending (η) and non-bending (ϕ) plane. If any ambiguity in η and ϕ-assignment is present, for example by a two body decay of low mass particles, this is resolved matching the muon track candidates with tracks in the inner detector.

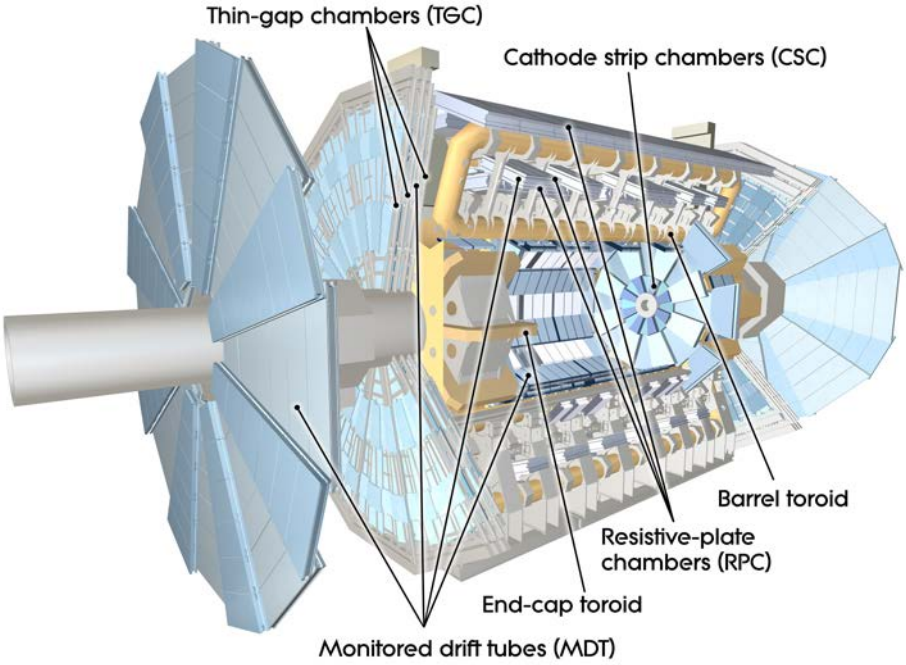

Figure 2.4: Cut-away of the ATLAS muon system [4].

Monitored Drift Tube chamber

MDT consists of three to eight layers of drift tubes, achieving an average resolution of 80 µm per tube. Their basic element is a pressurised 400 µm aluminium drift tube with a diameter of 29.970 mm filled with a mixture of Ar and CO_2 (93/7) at 3 bar. The length varies from 0.9 to 6.2 m, for a total of 1150 chambers. The achieved position resolution is about 35-50 µm for 6 or 8 layers chambers. When a charged particle passes through the tube, the electrons generated by the gas ionization are collected by the central tungsten-rhenium wire of 50 µm diameter at a potential of 3080 V. The operation of MDTs is limited in the first layer of end-cap, where the counting rates exceed the limit for safe operation in the detector. During the 2016/17 winter shutdown, new MDT drift tubes with diameter of 1.5 cm were installed to improve the muon momentum reconstruction [22].

Cathode-Strip Chamber

The CSC substitute the MDT of the first layer of the end-cap, covering the pseudo-rapidity range 2.0< $|\eta|$ <2.7. CSC combine high spatial, time (7 ns) and double track resolution with high-rate capability and low neutron sensitivity. CSC are multi-wire proportional chambers segmented in large and small chambers in ϕ, where the wires are oriented in the radial direction. The CSC system consists of two disks with eight chambers each, with each of them containing four CSC planes resulting in four independent measurements in η and ϕ along the track, reaching a position resolution of 60 µm. Both cathodes are segmented, one with the strips perpendicular to the wires (providing the precision coordinate) and the other with strips parallel to them (providing the transverse coordinate). The position of the track is obtained by interpolation between the charges induced on neighbouring cathode strips, while the CSC wire signals are not read out. The CSC chambers are filled with a mixture of Ar and CO_2 (80/20).

Resistive Plate Chamber

The RPC chambers offer quick information (1 ns time resolution) on muon tracks as they pass through the detector, allowing the L1 trigger logic to recognize their multiplicity and estimate their energy range. RPCs can be operated both in avalanche and streamer mode. In the LHC environment, the avalanche mode offers the benefit of higher rate capability and rate-independent time resolution and has therefore been selected as the operation mode. At the nominal operating voltage, a signal with a width of about 5 ns is generated by the track with a streamer probability of less than 1%. In the barrel region, the trigger system consist of three cylindrical layers around the beam axis. The arm between inner and outer RPC's permits the trigger to select high momentum tracks in the energy range 9-35 GeV (high-p_T trigger), while the two inner chambers provide the low-p_T trigger in the range 6-9 GeV. RPCs are gaseous

parallel electrode-plate detectors. The signal is read out through capacitive coupling to metallic strips mounted on the outer faces of the resistive plates, biased at about 10 keV. The gas used is a mixture of $C_2H_2F_4$/Iso-C_4H_{10}/SF_6 (94.7/5/0.3) which is a good combination between low operating voltage, non-flammability and low cost, with a safe plateau for avalanche operation. RPCs cover the pseudorapidity region $|\eta| < 1.05$.

Thin Gap Chamber

TGC provides muon trigger in the end-cap region of the muon spectrometer, but also the determination of an azimuthal coordinate to complement the measurements of the MDT's in the radial direction, measured by the radial strips. TGC need also good time resolution to tag the beam crossing with high efficiency and fine granularity. TGCs are multi-wire proportional chambers with a wire-to-cathode distance of 1.4 mm smaller than the wire-to-wire one (1.8 mm), covering the forward region in the range $1.05 < |\eta| < 2.4$. The gas mixture used is a highly quenching one of CO_2 and n-C_5H_{12} (55/45) which allows operation in a quasi-saturated mode with a gas gain of 3×10^5. The wire is biased at about 2.9 keV. Each chamber provides a spatial resolution of 1 mm and a time resolution of 5 ns.

2.1.4 Magnets

The ATLAS detector features a hybrid system of four superconducting magnets [23]. This system is 22 m in diameter and 26 m long, with a stored energy of 1.6 GJ. The magnet system consists of two sub-systems, a solenoid aligned with the beam axis providing 2 T axial magnetic field for the inner detector, and a barrel toroid and two end-cap toroids which produce a toroidal magnetic field of 0.5 T and 1 T for the muon detectors in the central and end-cap regions, providing the magnetic field over a volume of approximately 12 000 m^3. The four superconducting magnets of the

ATLAS detector are shown in Figure 2.5.

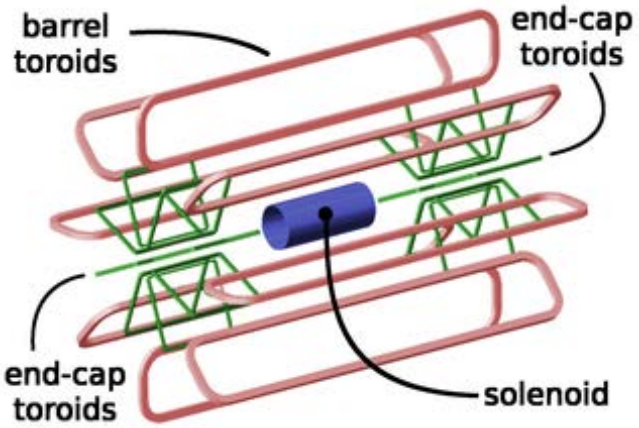

Figure 2.5: Illustration of the ATLAS detector superconducting magnets.

Central solenoid

The central solenoid is designed to provide 2 T axial magnetic field at the nominal operational current of 7.730 kA. The solenoid windings and LAr calorimeter share a common vacuum vessel in order to keep the material thickness in front of the calorimeter as low as possible, resulting in a total of $\approx$ 66 X_0 [24] for a normal incidence. The coils are wound with a Al-stabilized NbTi conductor developed in order to achieve high magnetic field with a reduced thickness. The inner and outer diameters of the solenoid are 2.46 m and 2.56 m for a length of 5.8 m, with a mass of 5.4 t and a stored energy of 40 MJ.

Barrel toroid

The barrel toroid provides magnetic field in the cylindrical volume surrounding the calorimeters and both end-cap toroids. The barrel toroid consists of eight coils encased in individual vacuum vessels. The coils conductor material is Nb/Ti/Cu and is the same used for the End-Cap Toroids. Those coils are 25.3 m-long and 10.7 m high, placed at about 9 m from the beam axis. The nominal current is about 20.5 kA generating a toroidal magnetic field with a maximum of 3.9 T and a stored energy of 1.08 GJ.

End-cap toroids

The end-cap toroids generate the magnetic field required for optimizing the bending power in the end-cap regions of the muon spectrometer system. Each end-cap consists of eight flat coils elements extending from a radius of 83 cm to 5 m for a weight of 239 per side. The magnetic field range is from 0.2 T to 3.5 T and the nominal current is 20.5 kA.

2.1.5 Forward detectors

Other detectors are located far away from the interaction point and very close to the beam axis. Those detectors have been designed for specific purposes, such as luminosity measurements and diffractive physics.

ALFA

The Absolute Luminosity For ATLAS (ALFA) [25] detector is located at $|z| = 240$ m. It consists of scintillating fibre trackers located in four Roman Pots, two per each side. Roman Pots can be moved towards the beam for dedicated data taking runs, until reaching a distance of about 1 mm from the beam. The purpose of ALFA is to

measure elastic p-p scattering in the very forward region. The elastic scattering in the very forward direction can also be used for luminosity measurements. Protons reaching the ALFA detector have an energy close to the one of the beam, and they can be detected with high position resolution (30 µm) in both directions.

AFP

The ATLAS Forward Proton (AFP) detector [26] looks for diffractive events where protons leave intact from the collision with a small diffractive angle. The AFP detector is placed at $|z| = 205\,\text{m}$ (NEAR stations) and $|z| = 217\,\text{m}$ (FAR stations) from the IP, with a total of four Roman Pots, two per each side of the ATLAS detector. Each Roman pot hosts tracking layers, while one Roman Pot on each side of the IP hosts a timing detector. The Silicon Tracker (SiT) is present in all four stations and it consists of four silicon 3D pixel detector planes mounted in each Roman Pot. They provide tracking with 10 µm and 30 µm position resolution in x and y, respectively. The 3D silicon pixel sensor technology is the same used for the IBL sensors. Time Of Flight (TOF) detectors are helded only in the FAR stations. They provide time information with 20 ps resolution to match the proton detected by AFP with the ATLAS primary vertex. In 2016 the first arm of the detector with SiT was installed in the tunnel and data to study tracker performances were recorded in dedicated low luminosity runs. In the 2016/2017 winter shutdown the silicon trackers were installed on both sides of ATLAS and in 2017 AFP participated in ATLAS high-luminosity data taking. A study of the performances of this detector during 2017 can be found in [27]. TOF detectors were finally installed in the 2019/2020 winter shutdown.

LUCID

The LUminosity Cherenkov Integrating Detector (LUCID) [28] is placed at $|z| = 17\,\text{m}$ from the IP. It detects the inelastic $p-p$ scattering in the forward region and measures

the integrated luminosity delivered to ATLAS. It is also the main ATLAS monitor for online luminosity. It is a Cherenkov light detector using aluminium tubes filled with C_4F_{10} surrounding the beam pipe.

2.1.6 Trigger System

Level-1 (L1), Level-2 (L2), and event filter are the three levels of the trigger system. Each trigger level refines the previous level's decisions and, eventually, adds more selection criteria. The L1 trigger looks for detector signals consistent with muons, electrons, photons, jets, and τ-leptons decaying to hadrons with high transverse momentum, as well as big missing and total transverse energy. It makes a choice on whether or not to analyze an event using a subset of the whole detector information, decreasing the data rate to around 75 kHz. It determines one or more Region of Interest (ROI) in each event, which are defined as the geographical coordinates in η and ϕ where the selection process has discovered interesting features. The ROI data includes details on the type of feature found and whether or not the requirements were met. The ROI information is fed into the L2 selection via a special data route provided by the L1 trigger. In roughly 40 ms, the L2 trigger drops the trigger rate to approximately 3.5 kHz. The event filter performs the final stage of event selection, reducing the data-taking rate to around 200 Hz.

2.2 ATLAS upgrade for HL-LHC

In order to cope with the increase of proton collision rate in the HL-LHC, the ATLAS experiment has planned a series of detector improvements [29]. The data collection for the HL-LHC is planned to begin in 2029, as shown in Figure 1.2, with an average pileup of about 200 collisions per bunch crossing. Detector improvements are required to maintain performance and thus to meet the ATLAS physics objectives. The luminosity increase also poses a significant challenge to the detectors (mostly

due to radiation hardness), trigger and data acquisition systems. The Phase-II upgrade programme foresees interventions in the following subdetector systems: pixel and strip trackers, LAr and Tile calorimeters, muon, trigger and data acquisition systems. Details of these improvements can be found in the technical design reports of each system [30, 31, 32, 33].

The ID will be replaced with a more radiation hard and with a finer granularity detector: a full silicon based ITk. This upgrade will be discussed in more detail in Section 2.2.1. Regarding the calorimeter system, the currently electronics is not compatible with Phase-II requirements for latency, trigger rate and radiation hardness. For this reason, a new front-end and back electronics will be installed. The Tile Calorimeter foresees a complete replacement of photomultiplier tubes in the most exposed region and also a full replacement of on-detector and off-detector electronics. The muon system upgrade will help to reduce triggers not coming from muons in the barrel and end-cap regions and to increase geometrical coverage in the barrel region where new MDTs and RPCs will be installed. RPC will also be installed on top of the existing MDT in large sectors. In the end-cap region, new TGC will be installed. These chambers will be based on a triple layer geometry (instead of a double one), in order to allow a more robust coincicende algorithm.

2.2.1 Inner Tracker

The ATLAS tracking system needs to be upgraded in order to maintain its performance after the HL-LHC upgrade, given the larger pileup and luminosity that have to be sustained. To face the larger pileup of approximately 200 inelastic p-p iterations per bunch crossing, finer granularity than the current detector will be used, while the large fluence requires more radiation hard detectors.
This section will discuss the baseline and the expected performance of the ITk detector, which will have to operate up to an integrated luminosity of $4000\,\mathrm{fb}^{-1}$.

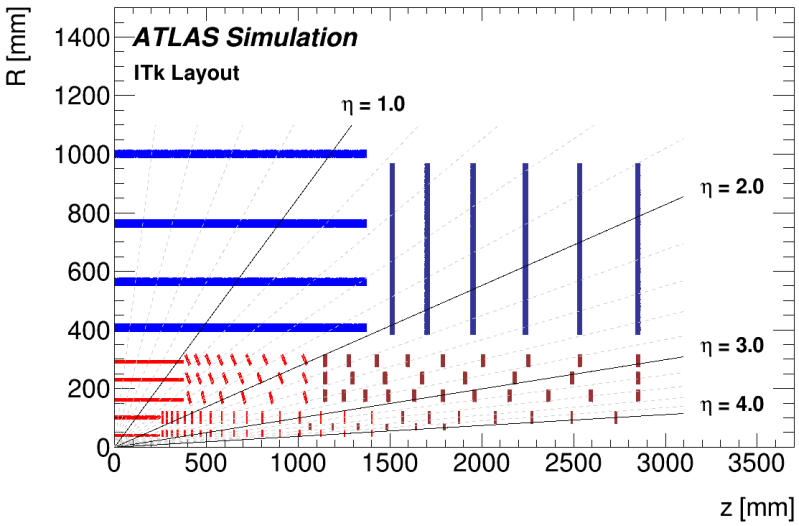

Figure 2.6: Schematic layout of the ITk detector. The active elements of the barrel and end-cap Strip Detector are shown in blue, sensors for Pixel Detector are shown in red for the barrel layer and in dark red for the end-cap rings. The horizontal axis is the beam axis with the zero being the interaction point [30].

Detector layout

ITk is a full silicon detector which consists of two sub-detectors: a Strip Detector surrounding a Pixel Detector. The strip detector is made of four barrel layers and six end-cap petal-design disks per side. The strip detector covers the region $|\eta|$ <2.7, and it is complemented by a 5 layer pixel detector which extends the coverage until $|\eta| = 4$. The schematic layout of the ITk detector is shown in Figure 2.6. The modules are placed on both sides of the mechanical structure of the Strip Detector, with the two strips sensors having a slight stereo angle between them. The modules are placed in the barrels in a way that the strips run nearly parallel to the beam axis, while the end-caps follow the radial direction to measure the ϕ coordinate with a high resolution. The stereo angle also enables the measurement of the z and R coordinates in the barrel and end-cap regions.

Radiation dose and fluence studies

Due to the increase in luminosity and in the rate of proton-proton collisions, the expected radiation level in the ATLAS ITk will increase by an order of magnitude compared to the present Inner Detector. Simulations for particle fluences and ionising dose for the ITk layout assume an integrated luminosity of 4000 fb^{-1}. Figure 2.7 shows the fluence and total ionising dose distributions for the Pixel Detector for 1 MeV neutron equivalent fluence and dose normalized to 4000 fb^{-1}. In the innermost layer of the ITk pixel barrel region, fluences are dominated by particles coming from the interaction point, while in the outer barrel layers and in the end-caps this is dominated by particles coming from secondary interactions in the detectors. In the

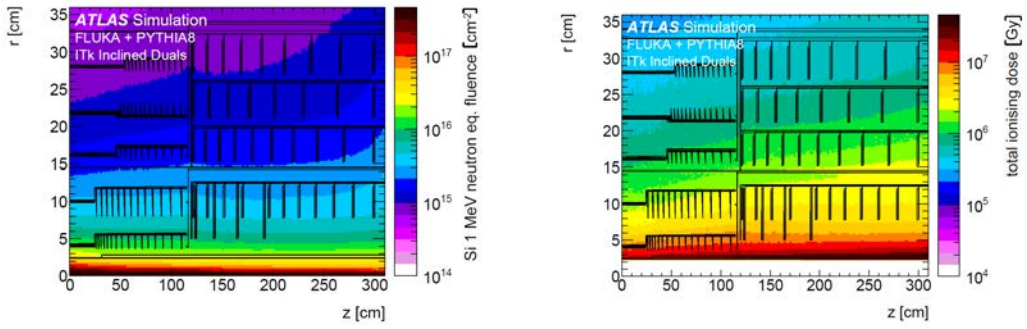

(a) (b)

Figure 2.7: Equivalent 1 MeV/cm^2 neutron fluence (a) and total ionising dose (b) maps in the ITk Pixel Detector normalized to 4000 fb^{-1} [30].

baseline scenario, the inner barrel and end-caps will be replaced after 2000 fb^{-1}, while outer pixel barrel and end-cap detector will not. A summary of the maximum 1 MeV neutron equivalent fluences and ionising doses is given in Table 2.1, where a safety factor of 1.5 is applied.

Pixel Detector sensors

The main change in sensor technology from the IBL to the ITk is the increase in radiation hardness requirements. In standard silicon sensors, the effect of radiation

Luminosity	Layer	Location	R [cm]	z [cm]	Fluence [10^{14}n$_{eq}$/cm^2]	Dose [MGy]
2000 fb^{-1}	0	flat barrel	3.9	0.0	131	-
			4.0	24.3	-	7.2
		inclined barrel	3.7	25.9	123	-
			3.7	110.0	-	9.9
		end-cap	5.1	123.8	68	6.3
2000 fb^{-1}	1	flat barrel	9.9	24.3	27	1.5
		inclined barrel	8.1	110.0	35	2.9
		end-cap	7.9	299.2	38	3.2
4000 fb^{-1}	2-4	flat barrel	16.0	44.6	28	1.6
		inclined barrel	15.6	110.0	30	2.0
		end-cap	15.3	299.2	38	3.5

Table 2.1: Maximal 1 MeV neutron equivalent fluences and total ionising doses for different parts of the Pixel Detector, for the baseline replacement scenario of the inner section. A safety factor of 1.5 is used [30].

is visible in a progressive reduction of the collected charge, which can be mitigated increasing the bias voltage. This leads to an increase of the leakage current which impacts the performances of the analogue front-end electronics, and can also cause a "thermal run-away". For this reason, it was important to make sensor design choices for each region of the ITk in order to guarantee stable thermal operation with high hit reconstruction efficiency.

For the ITk innermost layer, 3D sensors were chosen, while the rest will be instrumented by planar sensors. 3D sensors design differs from the standard planar in the orientation of the charge collecting electrodes, which are oriented perpendicularly to the sensor surface and penetrate through it, see Figure 2.8. 3D sensors offer excellent charge collection efficiency even in case of severe bulk damage induced by radiation. The first generation of 3D sensors with a pixel size of 50 µm×250 µm and a sensor thickness of 230 µm demonstrated radiation tolerance up to 9×10^{15} n$_{eq}$/^{2} [34]. However, in addition to an increased radiation hardness, ITk Pixel Detector requires 3D sensors with smaller pixel sizes and thinner active area to improve position resolu-

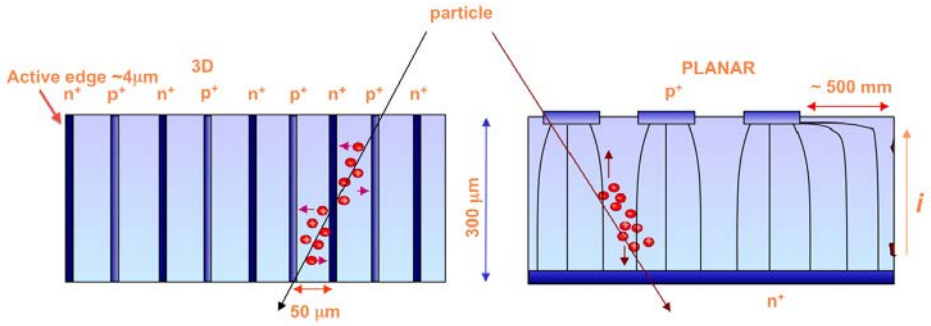

Figure 2.8: Schematic view of the electrode arrangement and charge collection in 3D (left) and planar (right) pixel sensors [30].

tion and to reduce detector occupancy in the innermost layer. Production of 3D devices with different thickness and pixel sizes of 25 µm×100 µm and 50 µm×50 µm have been carried out and characterized before and after irradiation. Test beam measurements resulted in hit efficiencies higher than 97% for sensors irradiated up to 1.4×10^{16} n_{eq}/cm^2 [35].

For the outer layers, planar sensors will be fabricated in the n-in-p technology, since this has advantages of simpler and cheaper fabrication procedures with respect to the n-in-n approach. A thickness of 150 µm has been chosen for the outer layers, while for Layer 1 a thickness of 100 µm will be used to guarantee performances after irradiation.

ITk tracking performance

ITk measurements will be fundamental in order to obtain the trajectory of particles, their momentum (p_T) measured from their curvature, and the polar (θ_0) and azimuthal (ϕ_0) angles of the tracks. The resolution of these parameters influence the performances of the detector in terms of $b-$tagging and lepton and jets reconstruction. The Pixel Detector is also fundamental for the determination of the transverse (d_0) and longitudinal (z_0) impact parameters of the tracks which are critical to associate efficiently charged particles to the correct production vertex. In Figure 2.9,

the track parameter resolution for a detector with 50 µm×50 µm pixels is shown as a function of η for a single muon. In the same plots, the performance of the ATLAS ID in Run-2 after the insertion of the IBL detector is also shown for comparison. An improvement can be seen for z_0 and θ_0 parameters due to the reduced pixel size along the beam axis. In the case of d_0 and ϕ_0 parameters, such an improvement is not seen. This can be related to the fact that there is no pixel size reduction along this direction, and also to the fact that ITk will be placed at 3.9 cm from the beam axis while the IBL is placed at 3.3 cm. The p_T resolution is improved in all the η region by a factor of 2, mostly because of the higher precision of the ITk Strip detector at large R compared to the TRT, and also to the reduced material. Another general improvement is the extension of the ITk coverage up to $|\eta| = 4$. However, in the forward region the ITk longitudinal resolution reaches 3 mm for particles with low transverse momentum, which is not good enough to face with the high level of pileup. For this purpose, another detector will be installed in the forward region: the HGTD.

2.2.2 High Granularity Timing Detector

HGTD will provide a time stamp for the tracks that hit HGTD, associated to the elapsed time between the time of the last bunch crossing clock signed and the arrival of the particle to the HGTD. The time information for each track will allow to separate the hard scattered from the pileup event, if the time resolution is good enough. The HGTD detector represents the core of this work and it will be fully described in the next chapter.

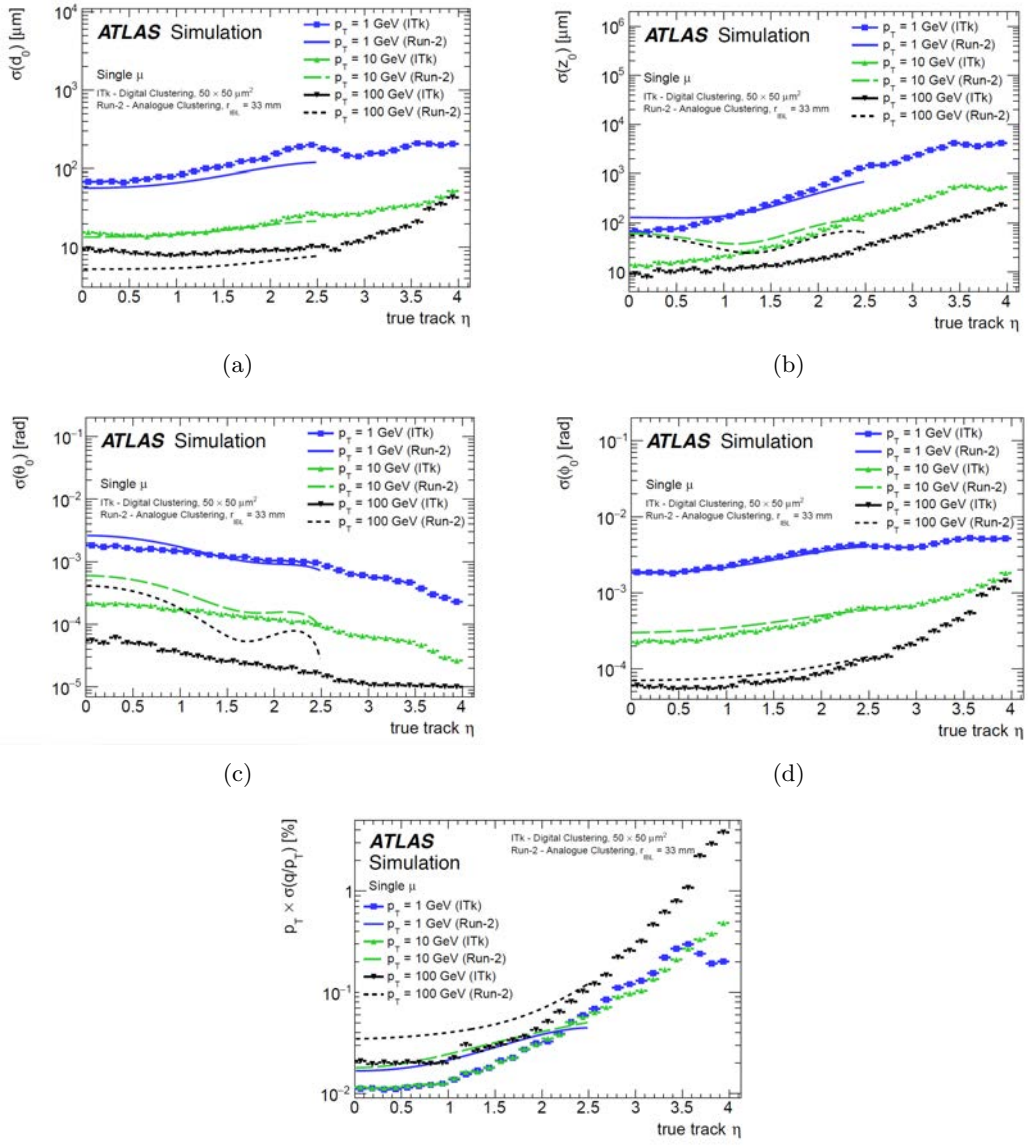

Figure 2.9: Track parameter resolution in d_0, z_0, θ, and p_T as a function of η for an ITk Pixel Detector with 50×50 mm^2 pixels. Results are shown for single muons of 1, 10 and 100 GeV in p_T. The reconstruction uses digital clustering information. For comparison, the resolutions for the Run 2 Inner Detector are also shown [30].

Chapter 3

The High Granularity Timing Detector

With the increase of the luminosity up to 7.5 $\times$ 10^{34} $cm^{-2}s^{-1}$ in the HL-LHC, there will be also an increase of pileup, with an average number of interactions per bunch crossing $< \mu >$ from 30 to about 200. This clearly means that pileup will be one of the major challenges in the HL-LHC scenario. In Figure 3.1, pileup density distributions for $< \mu >= 30$ and $< \mu >= 200$ are shown for comparison. With $< \mu >= 200$ an average of 1.8 vertices/mm is expected, degrading the vertex reconstruction and physics objects performance. To be able to associate efficiently charged particles to the correct production vertex, the resolution of the longitudinal track impact parameter z_0 has to be much smaller than 600 µm, which is the inverse of the average pileup density. In the central pseudorapidity (η) region, ITk detector provides a z_0 parameter well below this limit, but in the forward region the resolution reaches 3 mm for particles with low transverse momentum at $|\eta| \sim 4$, see section 3.1.1. Also, at high $|\eta|$ region, the Liquid Argon (LAr)[19] electromagnetic calorimeter has coarser granularity.

In this context, the time information can be used to distinguish the correct production

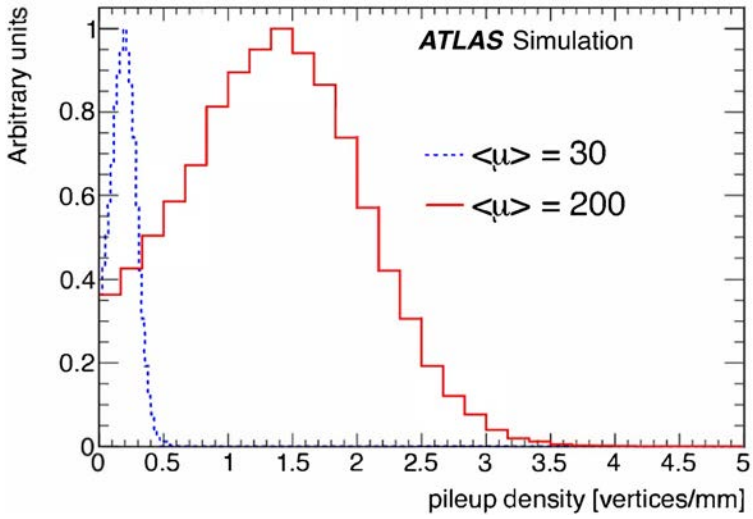

Figure 3.1: Local pileup vertex densities at generator level for $< \mu >= 30$ and $< \mu >= 200$.

vertex for charged particles, resolving ambiguities for nearby vertices whose distance is smaller than the track impact parameter resolution (if the time separation is sufficiently large). The development of silicon detectors with gain with a time resolution of a few tens of ps for HEP experiments offers a solution to reduce the detrimental effect of pileup in the forward region. The time information is complementary to the the track and p_T measured by the tracker and calorimeter, compensating the resolution degradation. A HGTD is proposed to mitigate the effect of pileup and improve the overall performances of the ATLAS experiment in the forward region by combining the HGTD time measurements with the position information from the tracker.

3.1 Physics motivation

Due to the large uncertainty of the longitudinal impact parameter for tracks in the forward region, the association of tracks to vertices with only spatial information is ambiguous in high pileup environments, especially for low transverse momentum tracks. The HGTD detector is a timing detector which will provide the charged track-

time information with a resolution of 30-50 ps per track. The ability to determine the time of the primary vertex of the hard-scattered process t_0 provides a new handle to enhance the capability of the ATLAS detector to remove pileup tracks contaminating physics objects originating from the hard-scatter vertex. The insertion of the HGTD detector will help in pile up jets reduction exploiting the vertex t_0 together with the forward tracks. This will have an impact in physics analysis through jet reconstruction, b-tagging and lepton isolation. In this section, the impact of the HGTD on detector performance will be briefly pointed.

3.1.1 Track to vertex association

The association of a track to the respective production vertex is a key element in the mitigation of pileup effects on the reconstructed event. Several processes, such as b-tagging and lepton isolation, depend strongly on the correct assignment of tracks to their primary vertices and jets. A track is associated to a vertex if the impact parameter z_0 is compatible with the vertex position z_{vertex}. To evaluate the compatibility the following equation is considered:

$$\frac{|z_0 - z_{vertex}|}{\sigma_{z_0}} < s, \tag{3.1}$$

with σ_{z_0} the longitudinal impact parameter resolution of ITk and s is a significance cut. In Figure 3.2, the behavior of σ_{z_0} parameter is shown with respect to $|\eta|$. For a track with p_T =1 GeV at $|\eta|$ =3 the resolution of the longitudinal impact parameter is about 1 mm. With an average vertex density of 1.8 vertices/mm at $< \mu >= 200$, a track with such a low p_T can be compatible with up to 9 near-by vertices, becoming ambiguous at large pseudorapidity and high luminosity. In this context, the track-to-vertex association will critically suffer from pileup contamination. Introducing timing information is a powerful way to address this issue. Figure 3.3 shows the time dispersion as a function of the truth iteration z position from simulation, in a

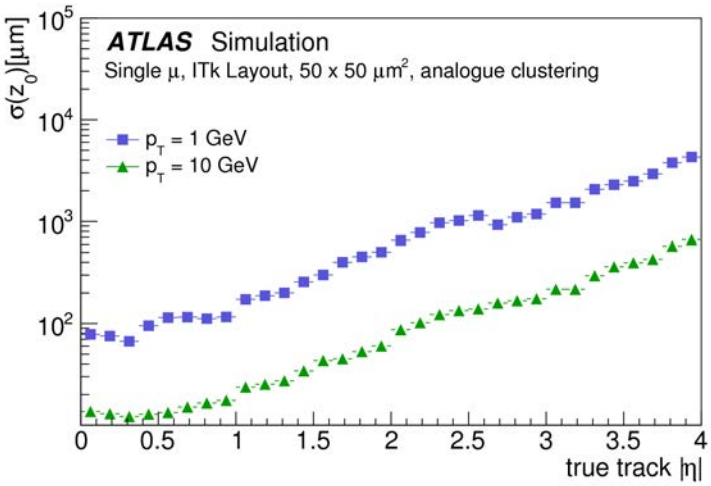

Figure 3.2: Resolution of the longitudinal track impact parameter, z_0, as a function of η for muons of $\mathrm{p}_T = 1\,\mathrm{GeV}$ and $\mathrm{p}_T = 10\,\mathrm{GeV}$ using ITk alone.

single bunch crossing. By requiring that all the tracks within a certain time window around the primary vertex have a common time compatible with the time of the hard scattered vertex[36], the effect of pileup can be reduced. There are two main strategies

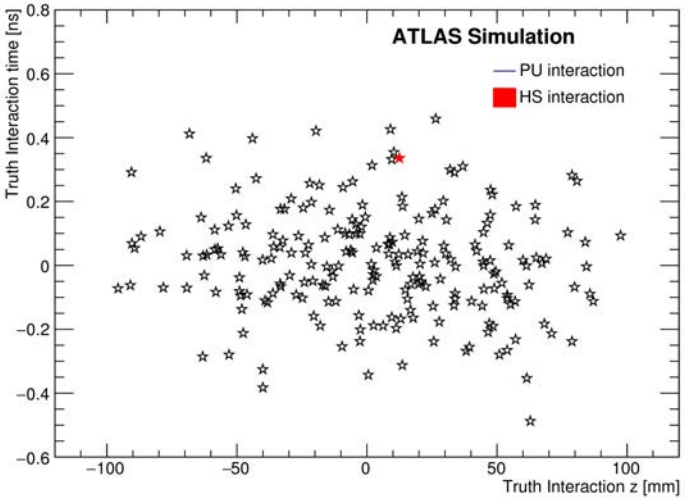

Figure 3.3: Truth interactions in a single bunch crossing in the $z-t$ plane, showing the simulated hard scattered event interaction with the pileup superimposed ones for $<\mu>= 200$.

to use timing information in order to improve the reconstruction performance: space-time track-to-vertex reconstruction and self-tagging.

Space-time track-to-vertex reconstruction

This is a natural extension of the track-to-vertex association in 4 dimensions. In this approach, the time t_0 of the hard scattered vertex is determined as a global reference to check the compatibility of the time of the tracks associated to physics objects in that event. Once a time vertex t_0 is found, tracks have to satisfy the following

$$\frac{t_{trk} - t_0}{\sigma_t} < s \tag{3.2}$$

where σ_t is the sum in quadrature of t_0 and the track-time, t_{trk}, and s is a significance cut. This approach is limited by the boundaries on the determination of vertex t_0. The experimental determination of the time vertex t_0 is challenging. The key factors which affect the accurate determination of the hard scattered vertex time are two: firstly, the hard scattered interaction needs to have enough high-p_T tracks in the HGTD acceptance region. Secondly, hadrons have a limited efficiency for correct track-time association, reducing the number of tracks accessible to calculate the time t_0. In the VBF H(inv) sample, these two effects limit the availability of the global vertex time to approximately 65% [37].

Self-tagging

This second approach checks if the times of all tracks associated to the same physics object are consistent to each other. More generally, it entails locating clusters of compatible tracks within a jet and then dividing the jet into smaller sub-jets with consistent timings. However, this approach is limited by several factors, since it requires that a physical object has at least two tracks associated with an assigned time. It can be also addressed in the case of stochastic pileup contamination, since opposed to hard-QCD pileup interactions. This method assumes that a jet is an object with a group of tracks with a common time, plus an additional track, coming from pileup interaction, from nearby which is out of time. In a hard-QCD pileup jet this method

is not applicable, since the tracks coming from the jets have a common time. Since the fraction of hard-QCD pileup jets increases with the increasing of p_T, the self-tagging method works better for low p_T tracks. In any case, this approach can have an important role in other applications, such as $b-$tagging or particle flow jet reconstruction, where there are many tracks available, and it can be used complementary to the global t_0 method discussed above, to maximize performances across the jet p_T.

3.1.2 Suppression of pile up jets

The high quantity of pileup jets which will be present during HL-LHC period can have an impact on the precision of Standard Model physics measurements. Their efficient identification is a key point to enhance the physics potential of the HL-LHC. Pileup jets can increase the number of background events passing a selection criteria, and also reduce the potency of kinematics variables or discriminant used to separate signals from background. Two main processes can be the origin of pileup jets: they can be produced from a hard QCD process from a pileup vertex or from a random combination of particles from multiple vertices. At low jet p_T, the second process is dominant while at high jet p_T the majority of pileup jets come from QCD jets. The precise linkage of jets with tracks and primary vertices is a critical element to suppress pileup in jets. The R_{pT} jet variable is a basic but effective discriminant. It is defined as the sum of all tracks inside the jet cone with their origin in the hard scattered vertex PV_0 divided by the fully calibrated jet p_T:

$$R_{p_T} = \frac{\sum p_T^{trk}(PV_0)}{p_T^{jet}} \tag{3.3}$$

The tracks used to calculate R_{pT} are required to have p_T >1 GeV. Hard scatter and pileup jets are distinguished by their matching to truth jets. The reconstructed hard scatter jets are required to be within $\Delta R = \sqrt{(\Delta\eta)^2 + (\Delta\phi)^2} < 0.3$ of a truth jet with p_T >10 GeV.

With a moderate level of pileup, the track impact parameter measurements can be used to assign track to vertices with small ambiguity. In this case, small values of R_{pT} correspond to jets that have a small proportion of charged particle p_T coming from the hard-scattered vertex PV_0 and are likely to be pileup jets. However, the power of this discriminant is lowered during high pileup conditions, particularly in the forward region. In this condition the longitudinal impact parameter resolution deteriorates (see Figure 3.2) and the pileup tracks could have a greater chance to be incorrectly included in the numerator of R_{pT}.

3.1.3 Lepton track isolation

In the forward region, the large z window required to associate tracks with their primary vertex results in an increased pileup contamination, with a degradation of the isolation efficiency. The efficiency of the track-based lepton isolation is defined as the probability to have no additional tracks reconstructed within ΔR <0.2 of the lepton track with a p_T >1 GeV. The association of a time to the lepton track can be then utilised to reject tracks within the isolation cone which come from pileup interactions with spatial vertex close to the hard scattered one. If the time difference between the electron track and all the tracks with p_T >1 GeV and ΔR <0.2 is larger than twice the quadratic sum of both tracks, the track is discarded. In Figure 3.4, the isolation efficiency as a function of the pileup density is shown for both ITk only and ITk + HGTD scenarios. In the only ITk case the efficiency drops as the pileup density increases. This drop is reduced with the use of the HGTD timing information, and the efficiency is kept above 85% up to high pileup densities for both the beginning and the end of its lifetime. HGTD timing information improves by about 10% the electron isolation efficiency for a local pileup density of 1.6 vertices/mm. These results show that the expected HGTD performance is good enough to achieve a similar level of lepton track isolation efficiency to the one achieved in the central region.

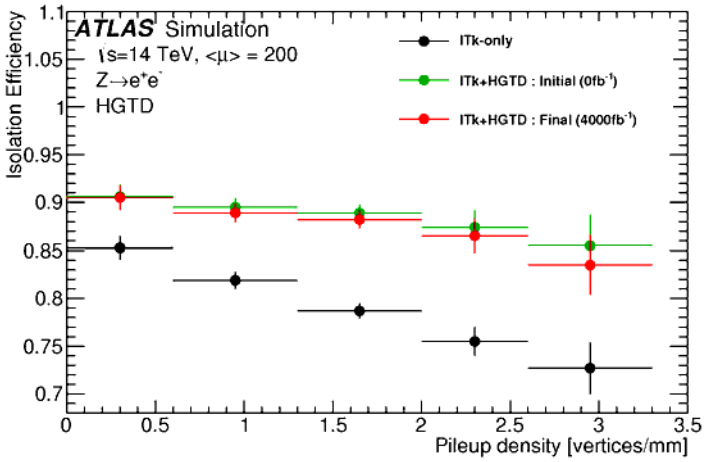

Figure 3.4: The efficiency for electrons to pass track-isolation criteria, denoted as $\epsilon(p_T^{iso})$, as a function of the local vertex density, for the ITk-only and ITk+HGTD scenarios. The isolation efficiency is shown for both the "initial" time resolution of the detector as well as the "final" time resolution at the end of the HGTD lifetime [37].

3.1.4 Other applications

The addition of time information to the whole suite of ATLAS physics object event reconstruction is likely to increase performance in areas not considered yet. With the addition of timing information, the beam spot can be determined in four dimensions, providing an extra tool for understanding the beam. This can result in improvements in multiple uses, such as for example tracking and flavor-tagging in the online trigger system, offline reconstruction and calibration processes. Particle-flow jet energy reconstruction, transverse missing E_T, and forward b-jet tagging are also likely to benefit from the HGTD.

Particle-flow jet energy reconstruction relies on the ability to match charged particle tracks with calorimeter signals and primary vertices. Improving the jet energy resolution can lead to further improvements of sensitivity in other channels, such as VBF analysis. However, the full integration of the HGTD into the particle flow reconstruction is a long term goal.

HGTD can be potentially utilised to enchance the resolution of the missing E_T. This would mean to use HGTD at first to improve the jet energy resolution from particle flow reconstruction, and then reducing the pileup contamination in the track-based soft-term of the missing E_T. At last, the improved pileup suppression in the forward region will be directly correlated to an improvement on the missing E_T resolution, through the rejection of jets which appear to belong to the primary vertex but do not belong to the hard scatter interaction.

HGTD will be also very useful in the mitigation of the impact of pileup track contamilation on $b-$tagging. In a harsh pileup environment, the presence of pileup tracks with large z impact parameter with respect to the hard scatter vertex can create fake secondary vertices which will be then translated into a reduction in light-quark rejection. The lost of $b-$tagging performances at high pileup densities could be compensated by a combination of self-tagging (for high multiplicity jets) and vertex t_0. However, the full incorporation of timing information for heavy-flavour tagging will require more infrastructure and is left for future studies. A preliminary study on the mitigation of the pileup through the insertion of the time information from the HGTD detector on the $Z \to \tau\tau$ background of the $H \to \tau\tau$ process will be given in Chapter 4.

3.2 HGTD as a luminometer

A precise determination of the luminosity delivered by the HL-LHC will be crucial for physics analysis. In fact, the uncertainty on the integrate luminosity can limit the precision of several cross-section measurements. Apart the normalisation of the signal, this can also affects the normalisation of any background not determined from data. The precision of the luminosity measurement is critical for measuring several Standard Model processes, such as W and Z boson production and single and pair production of top quarks. More detailed informations on the expected performances

of the luminosity determination during HL-LHC program can be found in [38]. For cross section measurements like gluon-fusion (ggH) production of Higgs boson with decays to $\gamma\gamma$ and ZZ^* and combined gluon-fusion and VBF) production of Higgs with decay to $\tau\tau$ an uncertainty of 2% on luminosity would be the largest source of uncertainty on the results. This make clear the importance of a precise luminosity measurement for the Higgs boson physics programme at the HL-LHC. The HGTD detector provides unique capabilities for measuring luminosity at the HL-LHC. The high granularity of the HGTD gives an excellent linearity between the average number of simultaneous pp interactions over the full range of luminosity expected at HL-LHC. From simulations, a linear relationship between number of hits and number of interactions was extrapolated for $\mu \sim$200 where the predictions can be compared to the hit multiplicities extracted from fully simulated high-pileup samples. The charged particle multiplicities within the acceptance can be determined accurately for each individual bunch crossing. The HGTD will provide both online and offline luminosity measurements. It will be done in a reduced $|\eta|$ range, and it has been proposed to read out the Application-Specific Integrated Circuit (ASIC) for sensors at 430 mm$< r <$640 mm (or $2.4 < |\eta| < 2.8$). The time resolution of the HGTD allows measuring and subtracting some backgrounds in the high-radiation environment. The uncertainties of those backgrounds can limit the precision of methods relying on hit-or track-counting techniques. The HGTD will have a dedicated readout path to send occupancy data for each module at 40 MHz allowing bunch-per-bunch luminosity measurements online without trigger bias. HGTD is designed to be capable to constrain many systematic uncertainties in the luminosity determination, with the goal of reducing the total uncertainty on the integrated luminosity measurements in HL-LHC compared with respect to those in Run 2, despite the harsh experimental conditions.

3.3 The HGTD detector

3.3.1 Detector overview and requirements

The HGTD has been designed for operation with 200 proton-proton collisions per bunch crossing and for a total integrated luminosity of 4000 fb^{-1}. The detector will be installed in the region between the ITk detector and the end-cap calorimeter, at a distance from the nominal interaction point (IP) of $z = \pm$ 3.5 m on both sides of ATLAS detector. This place is currently occupied by the Minimum-Bias Trigger Scintillator (MBTS), which will be removed. The position of the two vessels for the HGTD within the ATLAS detector is shown in Figure 3.5. The detector area has a

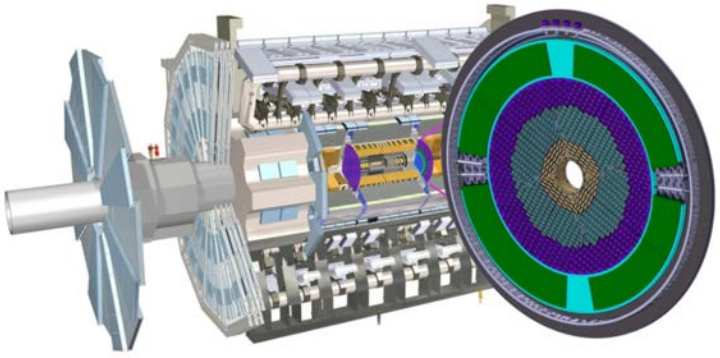

Figure 3.5: Position of the HGTD within the ATLAS detector. HGTD acceptance is defined as the surface covered by the HGTD between a radius of 120 mm and 640 mm at a position of $z = \pm$ 3.5 m along the beamline, on both side of the ATLAS detector [37].

radial extension from 110 mm to 1000 mm, with an extension in z of 125 mm including moderator, supports and vessels covers, and its active area will cover the psesudo-rapidity range $2.4 < |\eta| < 4.0$ (120 mm $< r <$ 640 mm). A 50 mm-thick moderator made of borated polyethylene will be placed behind the detector to reduce the back scattered neutrons created by the calorimeters. The tight space available is one of the main motivation to make the HGTD in a compact silicon technology, with sensors required to be thin and configurable in arrays while providing excellent time resolution ($\sim$30 ps). LGAD [39] with pads of a size of 1.3 mm$\times$1.3 mm and an active thickness

of 50 µm were chosen for the HGTD. The reason of this choice will be explained in the next section. To mitigate the impact of irradiation, sensors will be operated at −30 °C. A custom ASIC, ATLAS LGAD Time Read Out Chip (ALTIROC), will be bump-bonded to the sensors and it is currently being developed to meet the HGTD requirements in terms of time resolution and radiation hardness. The ASIC will also provide functionality to count number of hits registered in the sensors and transmit it at 40 MHz to allow bunch-per-bunch luminosity measurements, and the implementation of a minimum-bias trigger. Other features about HGTD as luminometer have been discussed in section 3.2.

Each HGTD end-cap is made of one hermetic vessel, two instrumented double-sided layers mounted on cooling and support disks, and two moderator pieces both inside and outside the hermetic vessel. The two layers are rotated in opposite directions with respect to the other by 15° to 20° in order to maximise the hit efficiency. HGTD is based on a three ring layout with active regions of 120 mm$< r <$230 mm, 230 mm$< r <$470 mm and 470 mm$< r <$640 mm. Beyond the third ring, for $r >$640 mm there will be the peripheral electronic. The reason for the three ring layout is explained in section 3.3.4. The global view of the HGTD is shown in Figure 3.6 and its requirements are listed in Table 3.1.

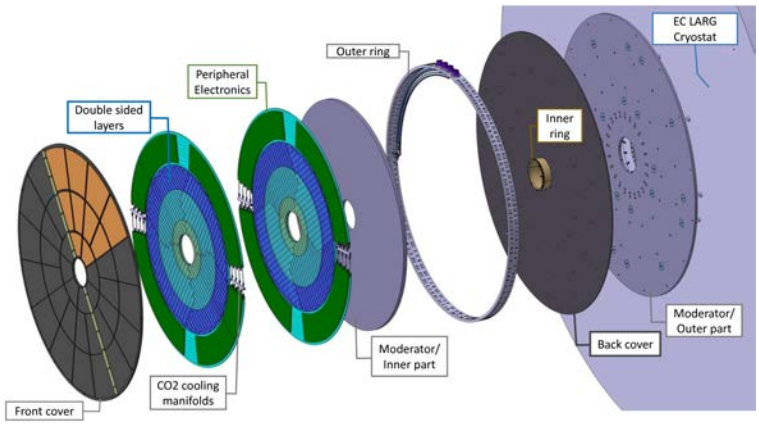

Figure 3.6: Global view of the HGTD to be installed on each of the two end-cap calorimeters. The various components are shown: hermetic vessel (front and rear covers, inner and outer rings), two instrumented double-sided layers (mounted in two cooling disks with sensors on the front and back of each cooling disk), two moderator pieces placed inside and outside the hermetic vessel [37].

Pseudorapidity coverage	$2.4< \|\eta\| <4.0$
Thickness in z	75 mm (+50 mm moderator)
Position of active layers in z	± 3.5 mm
Weight per end-cap	350 kg
Radial extension	
Total	110 mm$< r <$1000 mm
Active area	120 mm$< r <$640 mm
Pad size	1.3 mm×1.3 mm
Active sensor thickness	50 μm
Number of channels	3.6 M
Active area	6.4 m^2
Module size	15×15 pads (2 cm×2 cm)
Modules	8032
Collected charge per hit	>4 fC
Collected hit per track	
$2.4< \|\eta\| <2.7$ (470 mm$< r <$640 mm)	$\approx$2.0
$2.7< \|\eta\| <3.5$ (230 mm$< r <$470 mm)	$\approx$2.4
$3.5< \|\eta\| <4.0$ (120 mm$< r <$230 mm)	$\approx$2.6
Average time resolution per hit	≈ 35 ps($start$), ≈ 70 ps(end)
Average time resolution per track	≈ 30 ps($start$), ≈ 50 ps(end)

Table 3.1: Main requirements of the HGTD detector. Average time resolution is listed for both start and end of lifetime.

3.3.2 Detector Layout

HGTD aims to provide the best possible time resolution in order to be able to suppress pileup effects in the forward region. The capacity to link tracks to primary vertices is determined by the longitudinal impact parameter of ITk, as discussed in Section 2.2.1.

The LGAD pads size is the same for the entire HGTD, 1.3 mm×1.3 mm. This pad size ensure occupancies below 10% at the highest expected instantaneous luminosity, small dead areas between pads, low double hit probability for same sensor in one bunch crossing, and low sensors capacitance, which is important for time resolution. Moreover, for small pad sizes electronics noise and physics occupancy are smaller, while number of channels and total inactive area between the pads are larger. As a

baseline, an active thickness of 50 µm was adopted, as the best compromise between capacitance and deposited charge (favouring large thickness) and signal slope and Landau fluctuations (favouring a small one). Each HGTD module consists of 15×15 LGAD pads, with a total area of 2 cm $\times$ 2 cm. The total amount of module in HGTD is 8032. The module layout has been designed in order to maximize the coverage and minimizing the non-instrumented region. The HGTD module will be discussed in detail in Section 3.4.

The HGTD detector geometry has been optimized in order to achieve a flat time resolution as a function of η. Due to radiation damage, the time resolution will be degraded as the integrated luminosity increases. The radiation level in the detector depends strongly with r, where higher radiation level is closer to the inner radius. This will be discussed in Section 3.3.4.

Each layer of the detector is double-sided, with sensors mounted both in the front and back sides of the cooling disk. As shown in Figure 3.7, the modules on the two sides are arranged to overlap. Simulation studies were performed to determine the optimal overlap between the modules in the three rings to fulfill requirements for time resolution. For the inner ring an overlap of 70% is expected, for the middle ring an overlap of 54% and for the outer ring an overlap of 20%.

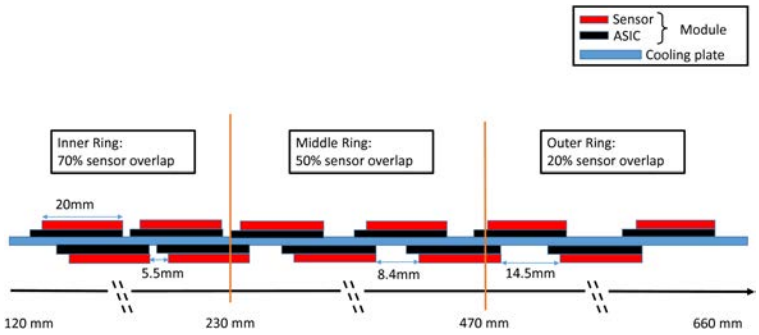

Figure 3.7: The schematic drawing showing the overlap between the modules on the front and back sides of a cooling disk [37].

The expected number of hits per track as a function of the radius is shown in Figure

3.8, with an average of 2.6 for the inner ring, an average of 2.4 for the middle ring ans 2.0 for the outer ring.

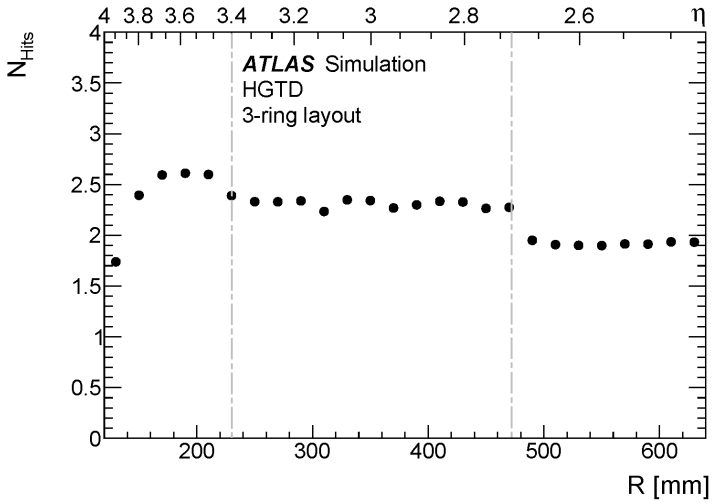

Figure 3.8: Hit multiplicity as a function of r. The figure was made using a simplified simulation, resulting in a 10% uncertainty compared to the full simulation studies of the HGTD. The vertical dashed line are representative of the separation between the rings [37].

The time resolution per hit and per track as a function of the radius are shown in Figure 3.9. The plot is made for several values of integrated luminosity during the HL-LHC lifetime, corresponding to the different replacement scenario of the detector. That will be described in Section 3.3.4.

3.3.3 Time resolution

The time resolution provided by the LGAD sensors is a key parameter of the HGTD. To ensure a good timing performance, the front-end electronics requires a minimum charge value of 4 fC for irradiated sensors. This will be discussed in Section 3.4. The target time resolution per track is 30 ps at the start and 50 ps at the end of lifetime, as shown also in Table 3.1. This means that the time resolution per hit should be around 35 ps at the start and 70 ps at the end of lifetime, given the number of hits

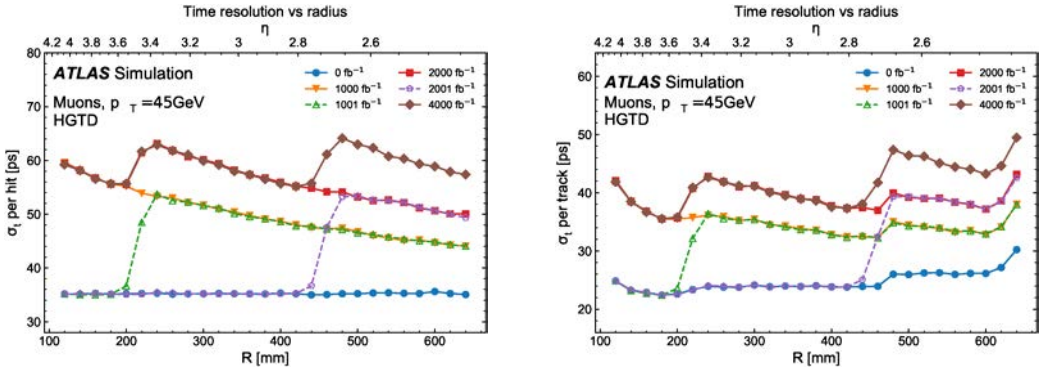

(a) (b)

Figure 3.9: Time resolution per hit (left) and per track (right) within HGTD acceptance region as a function of the radius. The time resolution is shown for different integrated luminosities. The improvement at high luminosity corresponds to the replacements of the innermost rings during the detector lifetime [37].

per track (see same Table).

The main contributions to the time resolution of a detector are:

$$\sigma^2_{total} = \sigma^2_{Landau} + \sigma^2_{Electronics} + \sigma^2_{Clock} \tag{3.4}$$

where σ^2_{Landau} indicates the Landau fluctuations in the deposited charge, $\sigma^2_{Electronics}$ is the contribution from the electronics (jitter and time walk) and σ^2_{clock} is the contribution from the non-deterministic jitter contribution from the clock distribution.

From test beam results, it has been understood that thin sensors help to reduce the contribution from Landau fluctuations. For 50 µm-thick LGAD, the Landau contribution is about 25 ps, which will be discussed again in Chapter 5.

The electronics contribution can be kept around 25 ps with a fast detector with high signal-to-noise ratio, for a **MIP!** (**MIP!**) particle at the beginning of the HL-LHC period. Electronics contribution to the time resolution will be explained in more detail in Section 3.5.2.

The clock contribution can be kept below 15 ps. There are several contributions to it coming from the readout system, such as the front-end electronics and the FLEX

cables. A preliminary plan for this correction consists in using conservative values of clock jitter contributions. If other unknown sources of jitter are present, the timing correction procedure can reduce the total jitter to 20 ps. This procedure also assumes no correlation between time offsets from different channels as a worst case scenario, even if some correlations from both global and local effects are expected.

The detector design has been tweaked to get close to a flat time resolution as η increases. The time resolution of the detector will deteriorate as the integrated luminosity delivered by the LHC increases owing to radiation degradation. This radiation is significantly influenced by r, with more radiation closer to the beam axis. The expected radiation level for the HL-LHC lifetime will be examined in the next section.

3.3.4 Radiation hardness

One of the most essential parameters of the HGTD detector is the radiation hardness of both sensors and electronics. The HGTD will be installed at $2.4 < |\eta| < 4.0$. It is important that the detector can withstand the radiation level throughout the HL-LHC operation period in order to ensure sufficient performance of sensors and electronics. At r =120 mm, the neutron equivalent fluence is expected to reach 5.6×10^{15} $\mathrm{n}_{eq}\mathrm{cm}^{-2}$ and a total ionising dose (TID) of about 3.3 MGy, as shown in Figure 3.10. After applying a safety factor of 1.5 for sensors and 2.25 for electronics (which is more sensitive to the TID), the HGTD detector needs to withstand 8.3×10^{15} $\mathrm{n}_{eq}\mathrm{cm}^{-2}$ and 7.5 MGy.

Through an intense R&D campaign carried out during the last years, a minimum charge of 4 fC can be reached up to a radiation damage of 2.5×10^{15} $\mathrm{n}_{eq}\mathrm{cm}^{-2}$ and 2.0 MGy. Since the radiation is influenced by the r, this has been translated into a three ring layout, already described in Section 3.3.2, with different replacements intervals for each ring. Sensors and electronics at lowest radius ($r < 230$ mm) will be replaced after each 1000 fb^{-1}, for a total of three times in the HGTD lifetime, while the ones in the middle region (230 mm $< r <$ 470 mm) will be replaced once after

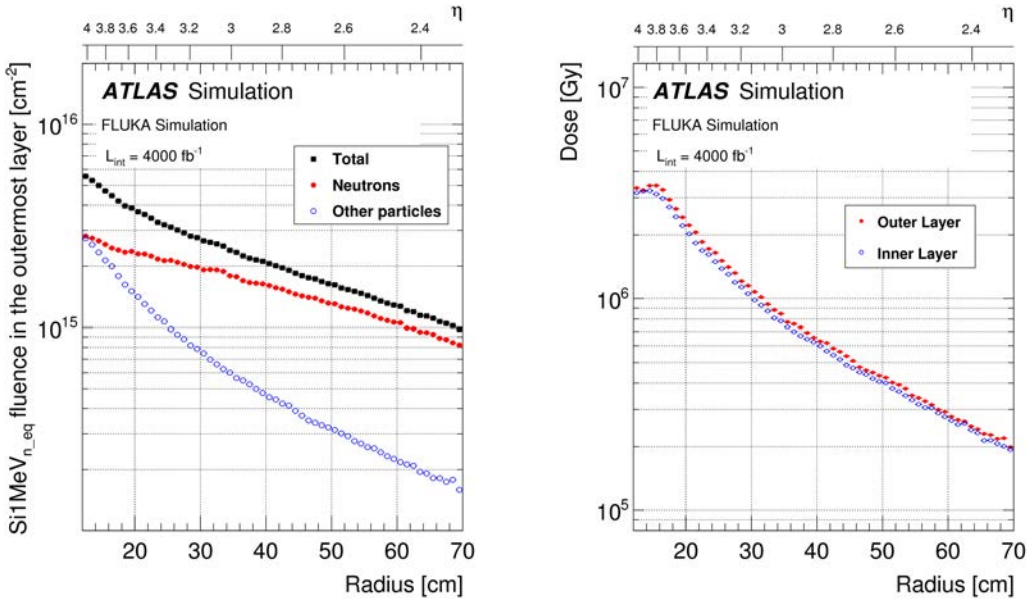

(a) (b)

Figure 3.10: Expected nominal Si1MeV$_{n_{eq}}$ fluence (a) and ionising dose (b), using Fluka simulation, as a function of the radius in the outermost sensor layer of the HGTD for 4000 fb^{-1}, before includig safety factors. The contribution from hadrons is included in "Others"[37].

2000 fb^{-1}. In this way, maximum fluence and TID do not exceed 2.5×10^{15} n$_{eq}$cm^{-2} and 2.0 MGy. In Figure 3.11, maximum fluence (a) and TID (b) as a function of the radial position, including the replacement of the three rings, are shown. The total fluence is a combination of neutrals and charged particles with different contribution in different regions. In the innermost region, the contribution from neutral and charged particle is similar, but the charged particle contribution decreases with radius, being the field dominated by neutron in the outer part because of back-scatter from the calorimeter. The maximum fluence from charged particles is around 1×10^{15} n$_{eq}$cm^{-2} while for neutrons is 2×10^{15} n$_{eq}$cm^{-2}.

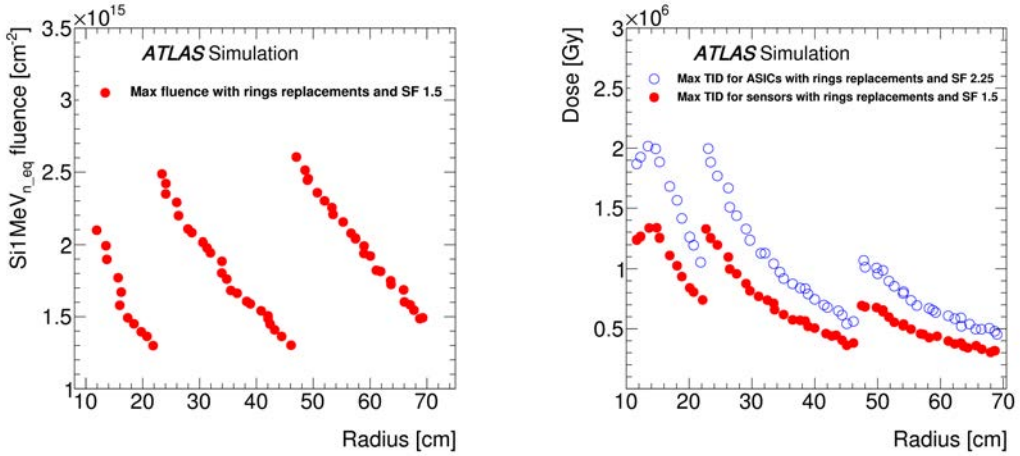

(a) (b)

Figure 3.11: Expected Si1MeV$_{n_{eq}}$ fluence (a) and ionising dose (b) in HGTD, using Fluka simulations, as a function of the radius considering the replacements of the inner ring every 1000 fb^{-1} and of the middle ring after 2000 fb^{-1}. The contribuion from charged hadrons is included in "Others". To account for simulation uncertainties, those plot includes a safety factor of 1.5. An additional 1.5 is applied to the TID to account for low dose-rate effects on the electronics, leading to a safety factor of 2.25 [37].

3.4 HGTD module

The HGTD module consists of two hybrid (or bare module) made of LGAD sensors (with 15 × 15 of 1.3 mm × 1.3 mm pads) connected to ALTIROC (of 15 × 15 channels) held together by a single flexible printed circuit board (the module flex). The sensor and the ASIC are connected through a flip-chip bump bonding process, also called hybridization. The back side (ohmic side) of the two sensors are glued to the module flex, the signal lines to the ASIC are wire bonded to the module flex, and the bias voltage is provided to the back-side of the sensors through holes in the module flex. The bare module consists in 225 channels or pads (15 × 15), with a size of 2 cm × 2 cm. Each pad will be connected to the ASIC through an 80 µm diameter solder bump. The module size has been defined in order to optimize the coverage at the inner radius and to provide a good yield for the hybridization process. HGTD will consists of 8032 bare modules. In Figure 3.12, a stave with three modules is shown. The

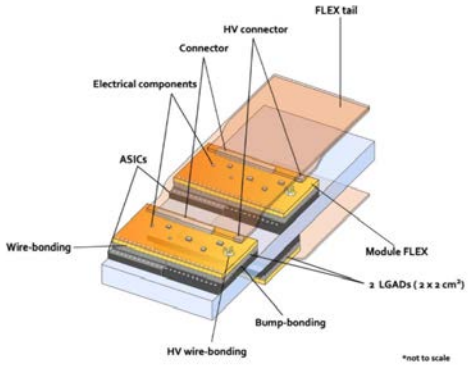

Figure 3.12: View of three HGTD hybrid modules (not to scale and qualitative) mounted on a cooling playe (grey plate). The wire-bonds for both ASICs and sensors HV are indicated.

flex cable provides the connections between the ASIC and the peripheral electronics. It transits the signal from the module to the peripheral electronics boards, as well as the power, clock and bias voltage are sent to the module from the pheripheral electronics. They can be long from 3 cm up to 60 cm depending on the position of the module inside the detector. The module flex uses two connectors to reduce the possibility of interference on the high voltage (HV) lines with the rest of the signals. One connector is dedicated to the HV connection, while the second one is used for other signals such as clock, data, monitoring, analog and digital power.

3.5 Front-end electronics

The performance of the silicon detector, which are the main topic of this thesis and will be discussed in Chapter 6, are strongly linked to the performance of the front-end electronics. Its main challenge will be to have a small enough contribution to time resolution in order to match with LGAD's performances. This contribution, as introduced in Equation 3.4, comes mainly from time walk and jitter components. Those contributions will be analyzed and discussed in Section 3.5.2. The measurements of the Time Of Arrival (TOA) and Tome Over Threshold (TOT) are digitized by two Time to Digital Converter (TDC) and stored in a local memory at channel level.

Finally, and End Of Column (EOC) logic is implemented to collect information. The largest part of the ASIC will be occupied by the 15 × 15 channel matrix which will have an area of 19.5 mm × 19.5 mm on a total ASIC area of 19.9 mm × 21.7 mm. The space left will be needed to accomodate the EOC logic and the digital blocks. The ASIC have been designed using 130 nm TSMC[1] technology. This has been tested up to 4 MGy even though a radiation hard digital library is not available. However, the ASIC has been designed to ensure its radiation hardness. The ASIC digital part is composed by several blocks necessary to generate and align the clocks, receive the slow control commands and configure the ASIC to be able to transmit the digitized data. Up to now, several versions of the ALTIROC have been produced and tested. The first prototype was ALTIROC0, a 2 × 2 channel array which included the analog part of a single channel readout, composed by preamplifier and disciminator. Results of this version from test beams and test bench studies show that using unirradiated 2 × 2 LGAD sensors a charge of 20 fC was achieved for a time resolution of 46 ps and a jitter of 39 ps [40]. The second prototype, ALTIROC1, consisted of a 5 × 5 matrix with the addition of digital components to the single channel readout with respect to the previous version. The last prototype, ALTIROC2, integrates all the functionality of the final ASIC and have the final size of a 15 × 15 pixel matrix.

3.5.1 General ASIC requirements

ASIC requirements are divided into two main areas: its operational environment, such as powering and electrical connections, and its performances to reach the target time resolution. The latter are listed in Table 3.2.

The ASICs have to withstand high radiation levels. As for sensors, some ASICs will be replaced during HL-LHC period, as presented in Section 3.3.4. Each channel readout will fit with a sensor pad, it will be capable to handle up to a leakage current of 5 µA without degrading ASIC performances. Since the sensor performances will

[1] Taiwan Semiconductor Manufacturing Company

Maximum leackage current	5 µA
Single pad noise (ENC)	<3000 e^- = 0.5 fC
Cross-talk	< 5%
Threshold dispersion after tuning	<10%
Maximum jitter	25 ps (70 ps) at 10 fC (4 fC)
TDC contribution	<10 ps
Time walk contribution	<10 ps
Minimum threshold	2 fC
Dynamic range	4 fC-50 fC
TDC conversion time	<25 ns
Trigger rate	1 MHz L0 or 0.8 MHz L1
Trigger latency	10 µs L0 or 35 µs L1
Clock phase adjustment	100 ps

Table 3.2: ASIC's performance requirements. The values for noise, minimum threshold and jitter consider a detector capacitance of $C_d = 4$ pF.

degrade with irradiation, it should be possible to set the discriminator threshold for small enough value of input charges. A minimum threshold of 2 fC should provide hit efficiency above 95% for an input charge of 4 fC. The main target for the electronics is to be able to read out signals from 4 fC to 50 fC for the entire HGTD lifetime. The electronics jitter is required to be smaller than 25 ps for a charge of 10 fC. This is equivalent to the deposited charge of a MIP in a 50 µm-thick LGAD with a gain of 20. A detector capacitance of 4 pF is considered. The TDC contribution to the time resolution should be negligible (<10 ps), this leads to a 20 ps TDC bin for the TOA measurements and a 40 ps for the Time Over Threshold TOT one. The time walk should be smaller than 10 ps over the range after correction. Both TOA and TOT information are transferred to the data acquisition system only upon L0/L1 trigger reception with a latency up to 35 µs, necessitating a large memory. The global phase adjustment of the clock should be guaranteed with a precision of 100 ps in order to center the 2.5 ns measuring window at the bunch-crossing. The ASIC will also need to handle the information to perform luminosity measurement computing the number of hits per ASIC on a bunch-by-bunch basis. Only the information of a subset of all the ASIC will be used, in order to limit the global bandwidth required. Finally, the power dissipation should be kept as low as possible, in order to limit the size required

for a single CO_2 cooling unit.

3.5.2 Contribution to the time resolution

The electronics contribution to the time resolution is given by Equation **??** can be described as the sum of three components:

$$\sigma^2_{Electronics} = \sigma^2_{Jitter} + \sigma^2_{Time\ Walk} + \sigma^2_{TDC} \tag{3.5}$$

The jitter describes the uncertainty in the time measurement due to the presence of noise in the signal, as shown in Figure 3.13 (a). It can be defined as:

$$\sigma_{Jitter} = \frac{N}{(dV/dt)} \sim \frac{t_{rise}}{(S/N)} \tag{3.6}$$

The time walk effect, described in Figure 3.13 (b), is related to the fact that larger signals cross the threshold earlier than smaller ones. This happens when the time is measured using a fixed threshold, producing a dependence of the measurements on the amplitude of the signal. It can be corrected using a Constant Fraction Discriminator (CFD) method. Time walk effect can be defined as:

$$\sigma_{TimeWalk} = \left[\frac{V_{th}}{\frac{S}{t_{rise}}} \right] \tag{3.7}$$

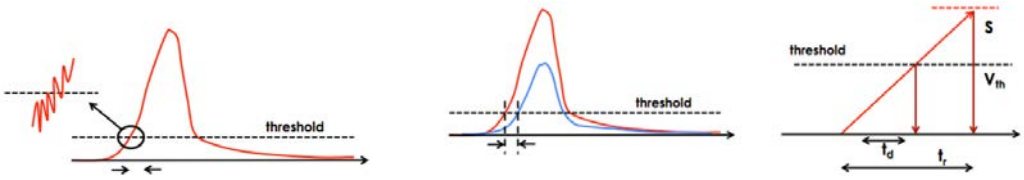

(a) (b)

Figure 3.13: Jitter (a) and time walk (b) effects in the time measurement using a constant threshold discriminator.

Both jitter and time walk as given in Equations 3.6 and 3.7, depend on the inverse of

the signal slope dV/dt, where S is the signal (proportional to the gain), N the noise, t_{rise} the rise time and V_{th} the threshold voltage. Jitter contribution optimization is discussed in Section 3.5.3. The time walk effect can be corrected by the measurements of the width of the pulse above the threshold level, also known as TOT, which is well correlated to the pulse amplitude. HGTD choose as baseline for the time walk correction a TOT measurement with a constant threshold discriminator. With it a residual error less than 10 ps is present after correction, for which the time walk effect is considered negligible. An alternative method to correct the time walk effect is the CFD method, where the time walk is minimised by defining the time of arrival as the time when the signal crosses a constant fraction of its maximum amplitude. Although, this method cannot be realistically implemented in a readout circuit, due to the fact that the maximum value is reached once the threshold has been already crossed. The CFD method will be used for the time resolution analysis of laboratory and test beam data, included in Chapter 6. The last component of equation 3.5 introduced an error due to the binning of the TDC circuit. This contribution is given with the following equation:

$$\sigma_{TDC}^2 = \frac{T_{bin}}{\sqrt{12}} \tag{3.8}$$

where T_{bin} is the bin size, assuming all the bins with the same size for an ideal TDC. HGTD will provide ∼20 ps fine binning for TOA and 40 ps for TOT.

3.5.3 Single-channel readout electronics

The ALTIROC ASIC is a 225 channel matrix. The architecture of each individual readout channel can be divided into two parts, as shown in Figure 3.14. The analog front-end consists of a preamplifier, a discriminator and a TDC stage of the readout which are crucial elements for the overall electronics time performances. The digital part is responsible of the identification and storage of the hits and it contains also a separate block which is used to process luminosity information. The time of the pulse is determined using a discriminator following the preamplifier using a fixed threshold.

Offline a correction on the time walk is applied in order to account for the different TOA of the different pulse heights. Two TDCs are needed at the end to digitize the discriminator outputs. In this section, the components of the analog front-end will be discussed.

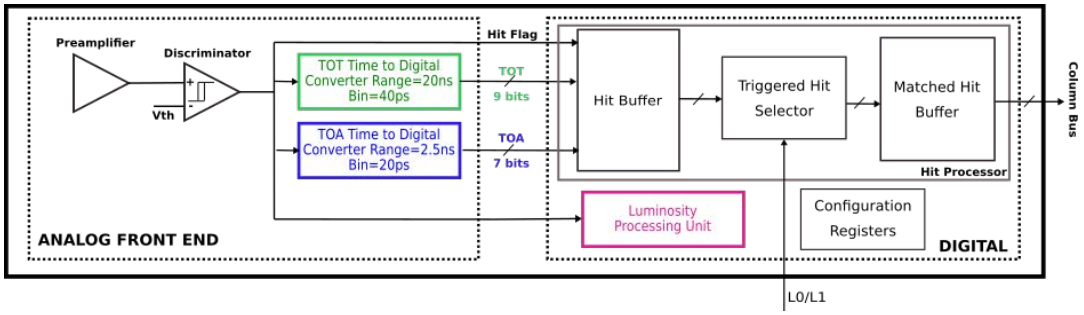

Figure 3.14: Schematic of the single-channel readout electronics. Two main blocks are identified, the analog and the digital part. The input pulse from the sensor enters the preamplifier on the left. The TOA and TOT data are read out by the column bus on the right [37].

Preamplifier

From Equation 3.6 the jitter contribution to time resolution depends by the ratio between the noise and the slope of signal pulse, such as an inverse dependence on the Signal-to-Noise ratio. Since the noise scales with the bandwidth as $\sqrt{BW}$ and the rise time grows with amplitude as S/BW, the first level of optimization relies on using a fast preamplifier. Over the last years, measurements in particle beam were performed with broadband amplifiers, which are voltage sensitive ones with $50\,\Omega$ input impedance. Timing optimization has been published for a trans-impedance configuration in [41, 42]. For a voltage sensitive amplifier, the jitter can be calculated assuming that the detector current is a short pulse with a characteristic time t_d. The input charge is the corresponding integral of the current over the time t_d. The jitter of the preamplifier can be then written as:

$$\sigma_{jitter} = \frac{e_n C_d \sqrt{t_d}}{Q_{inj}} \tag{3.9}$$

with e_n the noise spectral density and C_d detector capacitance. However, the jitter dependence on this is not very strong. Simulations show that for a sensor with $t_d \sim$ 600 ps, if the preamplifier rise time is reduced or increased by a factor of 2 with respect the optimal matching value, the jitter would deteriorate by just 12%. With those considerations, in order to minimise the jitter, the sensor should have a small capacitance, a short pulse duration and be capable to provide a large charge. The design of the ALTIROC chip uses a voltage sensitive preamplifier, shown in Figure 3.15. This is broadband preamplifier with a cascoded Common Source configuration, which consists of an input transistor (M1) and a follower transistor (M2). The R_2 resistor is connected to a feedback to ensure the biasing of preamplifier input. To adjust the fall time of the output, the value of R_2 can be modified. A pseudo-transimpedance configuration (TZ), shown in Figure 5.14b, has also been integrated in some channels of the ALTIROC prototypes, in order to choose the best performing preamplifier version. The configuration is very similar to the voltage one except that the R1 resistor is now in the feedback of the amplifier and it corresponds to the resistive component of Z f in Figure 3.15 (b). As mentioned before, detector capacitance is a key element to calculate the input voltage for a given input charge, depending on the relation $V_{in} = Q_{in}/C_d$. To compensate the irradiation effect on the rise time of LGAD sensors, which becomes smaller with fluence, the rise time of the preamplifier is tunable. This can be done adjusting the pole capacitance C_p.

Discriminator

The time measurement is performed by a discriminator which follows the preamplifier and provides the measurement of the TOA on the rising edge of the pulse, and the Time Of End (TOE) on the falling edge of the pulse from the detected particles. The subtraction of the two times provides the TOT measurement. To ensure a jitter smaller than 10 ps, the discriminator is built around a high speed leading edge architecture with hysteresis to avoid re-triggering effects. Two differential stages with

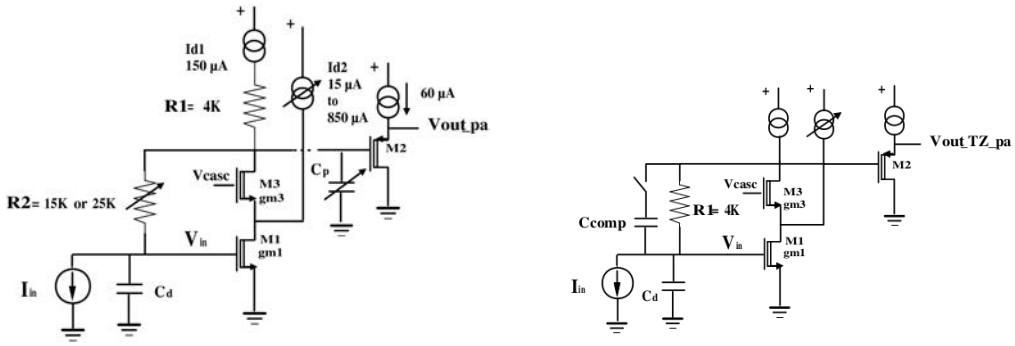

Figure 3.15: Schematic of the preamplifier implemented in the ALTIROC1 design [37]. Both voltage sensitive preamplifier (a) and pseudo-transimpedance (b) one are shown.

small input transistors are used to ensure a large gain and large bandwidth (approximatively 0.7 GHz). The discriminator threshold V_{th} is set by an external 10-bit DAC common to all channels. An additional 7-bit DAC (not present in ALTIROC0) allows to make small V_{th} corrections individually for each channel in order to compensate for differences among them or for different values of leakage current.

Time-to-Digital Converter

The time measurement provided by the discriminator is digitised through two TDC, one dedicated to the TOA and the other to the TOT measurements. The representation of the working principle of the TDC is shown in Figure 3.16. Since the target quantisation for the TOA is 20 ps, the Vernier delay line configuration is used. Its configuration consists of two lines each of them composed by a series of delay cells, controlled by a voltage signal (V_{ctrl}) that determines their delay. The timing resolution is determined by the difference in the delays of the cells in each line. The delay of the two lines is set differently, one to a smaller one (FAST) with a delay of 120 ps, and the other to a larger delay value (SLOW) where the delay is fixed to 140 ps. The TOA will be measured within a 2.5 ns window centered at the bunch crossing, with a quantisation step of 20 ps. The working principle of the TDC is the following.

The START signal (rising edge of discriminator) enters the SLOW delay line and the STOP signal (next rising edge of the 40 MHz clock) enters the FAST delay line. Each delay cell along the line brings the START and STOP signal closer to each other by an amount equal to the difference between the FAST and SLOW cell delays, which is 20 ps. The number of the cells necessary to the STOP signal to surpass the START signal results in the time resolution measurement with 20 ps step quantisation. The reverse START-STOP scheme is also used as power-saving strategy. The TOT TDC provides a 9-bit digitization of the discriminator width on a 20 ns range. It uses a coarse delay line made of 160 ps delay cells to extend the measurement range to 20 ps, while a Vernier delay line provides the requested resolution of 40 ps. The START and STOP signals are given by the rising and falling edge of the discriminator.

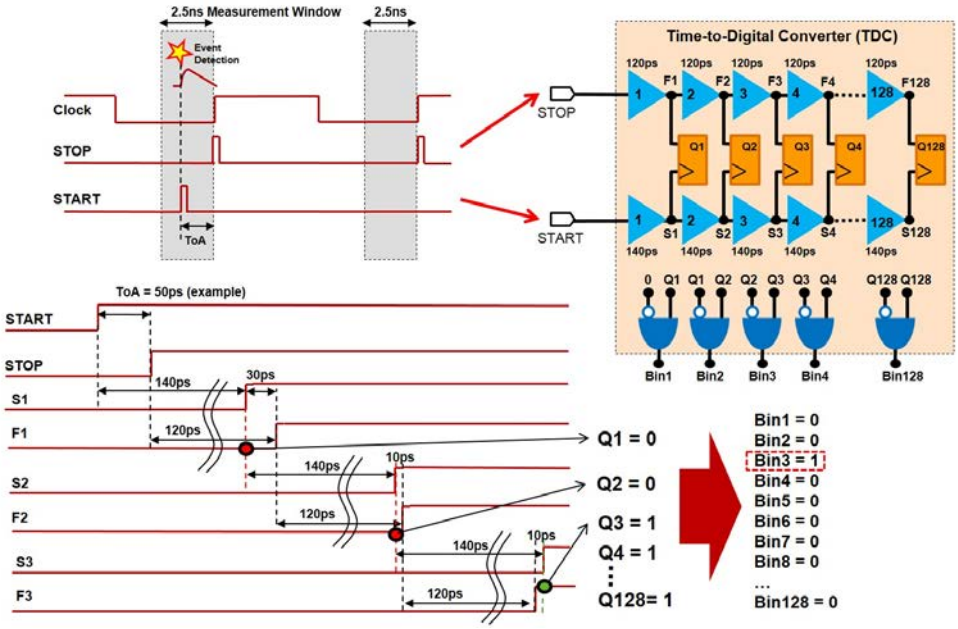

Figure 3.16: Graphic representation of the working principle of the TDC. The drawing on the top left shows how the START and STOP signals are generated, the first with the discriminator output upon event detection, the second corresponding to the next clock edge. The gray area indicates the 2.5 ns detection window. On the top right, the schema represents the TDC, with the 'slow' delay line (140 ps cells) that propagates the START signal, and the fast delay line (120 ps cells) in which the STOP signal is propagated. The difference between delays defines the bin. After each cell the signals are compared (QX), and the bin number provides the converted measurement [37].

3.6 Sensors

HGTD will be instrumented with LGAD silicon sensors. The characterization of LGAD sensors before and after irradiation, in charged particles beams and in laboratory with radioactive source or laser is the core of the work presented in this thesis. The LGAD technology will be explained in Chapter **??** while measurements and results will be presented in Chapter 6.

Chapter 4

HGTD impact on VBF H analyses at HL-LHC

4.1 The Standard Model in a nutshell

The theories and discoveries over the 20^{th} century have yielded a remarkable understanding of matter's underlying structure: everything in the universe is made from few basics blocks, the so called fundamental particles, which are governed by four fundamental forces. The theoretical framework which allows to describes the dynamics of those particles and of three of the forces is the SM of particle physics [43]: the electromagnetic force, governing interactions between charged particles, the weak interaction, responsible for the weak decays of particles and weak neutral currents, and the strong interaction, acting on quarks and responsible or their confinement in nuclei. The last remaining of the four fundamental forces, gravity, is currently understood in the domain of classical physics through General Relativity. Unfortunately, making this force compatible in a quantum field theory has proved to be a difficult challenge. Luckily, at the energies where the SM is tested experimentally the effect of gravity can be considered negligible. This theory was finalized in the 1970s, and it

has successfully explained almost all experimental results and predicted a wide range of phenomena, being established as a well tested theory. The last missing part of the puzzle, the Higgs boson, has been discovered by ATLAS [1] and CMS [2] experiments of the LHC in 2012, roughly 60 years after its prediction.

4.1.1 Standard Model particle content

The elementary particles in Figures 4.1 are the building blocks of the matter and are considered to have no substructure. The 12 fermionic particles of spin $\frac{1}{2}$ are separated in two families, the so called *leptons* and *quarks*, each of them consisting of six particles. All of them are arranged into three "generations" of matter, each of them consisting by two types of quarks and two types of leptons. The types differs for their mass between generations but have a similar behavior respect to the interactions. The SM also includes the antimatter variant of each particle, which differs from the particle by the sign of the charge and is denoted by the same symbol of the particle with a bar over it.

Quarks are particles that interact through the electromagnetic, weak and strong force. Up type quarks have a positive electric charge $Q = \frac{2}{3}$ while down type have a negative charge $Q = -\frac{1}{3}$. Each generation includes one up-type quark and one down-type one. In the first generation, they are u (up) and d (down), in the second c (charm) and s (strange) and in the third b (bottom) and t (tau). In addition to the electric charge, quarks also carry a colour charge, source of the strong field, existing in three states: green, red and blue. Colour charged particles have never been observed experimentally as free particles. Combination of colour charged particles can build neutral charge states when combining the three colours together or combining colour and anti colour. Hadrons can be either a combination of a quark and anti quark pair ($q\bar{q}$), called mesons, or as a three quarks states (qqq) called baryons.

Leptons are also arranged into three generation, each of them made of one electrically

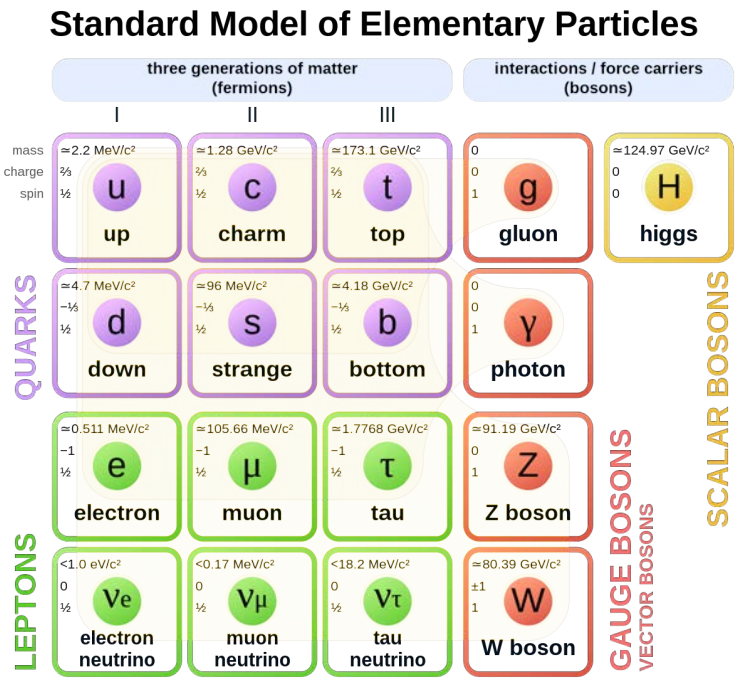

Figure 4.1: Overview of the Standard Model particle content. Properties like mass, charge and spin are also listed.

charged particles and a neutral one, called neutrino. The three charged particles e (electron), μ (muon) and τ (tau) have an electric charge $Q = -1$ and a sizeable mass, while the ν_e (electron neutrino), ν_μ (muon neutrino) and ν_τ (tau neutrino) are electrically neutral and have very little mass. Charged lepton and its associated neutrino carry the same lepton number. In the classical formulation of the SM, neutrinos were considered massless. However, experimental observation of neutrino oscillation [44, 45, 46] have shown that neutrinos must have a non-vanishing mass value, although very small. Charged leptons interact both electromagnetically and weakly, while neutrinos only interacts weakly. Due to this characteristic neutrinos usually pass through solid matter with very low changes to interact and are very difficult to detect.

In the quantum field theory, the different interactions are mediated by other particles which are called Gauge bosons, which are particles with integer spin value.

The strong force is mediated through gluons, which are massless bosons but contrary to the photons carry a color charge. The introduction of the strong interactio n was born from the need to explain the force that keeps together the protons inside nuclei and the quark bound inside hadrons. The postulation of the colour charge was motivated by the need to give an explanations of particles made of three identical quarks being consistent with Fermi-Dirac statistics. A new quantum number C, the colour charge, was the introduced. It can takes three different values: red (R), green (G) and blue (B). In this way, quarks can carry a colour charge while anti quarks carry an anti-colour charge. The gauge theory which describes the strong interactions between quarks and gluons is called Quantum cromodynamics (QCD).

The electromagnetic force is mediated by the photon, a massless particle which couples to all electrically charged particles and does not have charge. The $W^{\pm}$ and Z^0 bosons are carries of the weak force. $W^{\pm}$ particles have an integer charge and mediates interaction where charge is also transferred, while Z^0 is electrically neutral and it can only transfer spin, momentum and energy. The SM theoretical framework that describes the electromagnetism and the weak force it was introduced by Glashow, Weinberg and Salam [47, 48, 49]. Those forces unify at the electroweak scale into the Electroweak interaction (EW). While the photon only couples to electric charge, the massive $W^{\pm}$ and Z^0 bosons couple to the weak isospin carried by left-handed particles. Thus in its pure form, the SM theory works with only massless gauge bosons, which is in clear disagreement with the short range property of the weak interaction as well as the measured masses of the W and Z bosons. The solution to this problem is given by the introduction of Spontaneous symmetry breaking (SSB).

The requirement of a symmetry breaking ground state lead to an invariant formulation of the masses of both the electroweak gauge bosons as well as the fermions. This is what is known as the Brout-Englert-Higgs mechanism [50, 51]. As a consequence, an additional massive and scalar boson is predicted to exist, the Higgs boson. In 2012 of a new scalar boson was observed by the ATLAS and CMS experiments at CERN.

This particle appeared to be in good agreement with the SM prediction [1, 2].

4.1.2 Open questions of the Standard Model

Even though the SM is considered a very successful theory of particle physics and is currently the best description of the subatomic world, it does not explain everything. There are still a number of inconsistencies for which further extension of the SM are needed, such as the unification of forces, the dark matter, dark energy and the matter-antimatter asymmetry.

4.2 Impact of the HGTD in physics analysis

There are three main areas in which the HGTD dector is expected to enhance the physics capabilities od ATLAS by exploiting the new dimension of timing information to other detector measurements. The first area is the improve of the physics object reconstruction such as forward jets and leptons, which are key elements in VBF, Vector Boson Scattering (VBS), and lepton based forward-backward asymmetry measurements. The HGTD will aslo new features on the data from the use of timing information uncorrelated with other detector measurements, and a new capability for online and offline luminosity measurements at ATLAS to help achieve the 1% goal of uncertainty on the luminosity for the Higgs precision programme at the HL-LHC. The primary way in which HGTD can improve the VBF physics event reconstruction is in the reduction of the impact of the pileup. VBF final states are characterized by two tagged jets with a large rapidity gap with most of the time at least one of them in the HGTD acceptance region. This process will be discussed in the next section. In addition, a precise timing information is a completely new feature at hadron colliders experiments. It is expected that, using more precise machine learning algorithms and physics analyses with time information will result in both further improvements and new applications.

4.2.1 Vector Boson Fusion Higgs production

VBF Higgs boson production is the second largest production mechanism at the LHC. The cross section measurements of the VBF process $VV \rightarrow H$ followed by the Higgs boson decay into $\tau\tau$, WW and $\gamma\gamma$ will significantly extend the possibility of Higgs boson coupling measurements. This cross section is the highest one after the gluon-gluon fusion and provides key features in the trigger and offline in separating signal from the background.

The analysis of the VBF Higgs production is one of the major component of the physics programme at the HL-LHC. In this process, a quark from each of the incoming LHC protons radiates off a heavy vector boson. These bosons interact or "fuse"to produce a particle, such as a Higgs boson. The initial quarks that first radiated the vector bosons are deflected only slightly and travel roughly along their initial directions. They are then detected as jets in the different hemispheres of the detector. In Figure 4.2 the Feynman diagram of this process is shown. The main characteristic of a VBF event is the presence of two jets with a large rapidity gap. Most of the time, at least one of them is in the HGTD acceptance region, thus this final state can benefit from the improvement on jet reconstruction and pileup suppression provided by the HGTD.

The final state of this decay can be characterized by two leptons (ll), tho hadrons (hh) or a lepton-hadron couple (lh). One of the dominant backgrounds is due to the QCD $Z + jets$ production, here discussed, where the final state often contains a hard scattered jet plus at least one additional forward pileup one produced in a different interaction close to the hard scattered vertex. In Figure 4.3 both signal (a) and background (b) diagrams are shown. In this situation, timing information provided from the HGTD can help in overcoming the limitations of the tracking-based pileup jet suppression algorithm in the forward region. Reducing the effect of the pileup and improve the jet transverse momentum reconstruction can bring other improvements

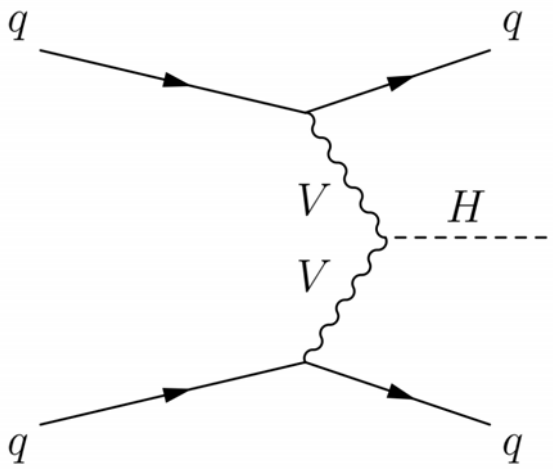

Figure 4.2: Feymann diagram of the VBF $H \to \tau\tau$ decay process.

in the signal to background ratio (S/B). In the HGTD Technical Design Report [37], a representative study for the invisible decays of the Higgs produced through VBF was chosen as representative analysis to illustrate the impact of the detector on VBF topologies. For the study of the impact pf the HGTD presented in this document, the $H \to \tau\tau$ channel with its main background $Z \to \tau\tau + jets$ are considered. Unfortunately, the signal sample was not available at the time of this study, which is then performed considering only the effect of the HGTD detector on the background sample.

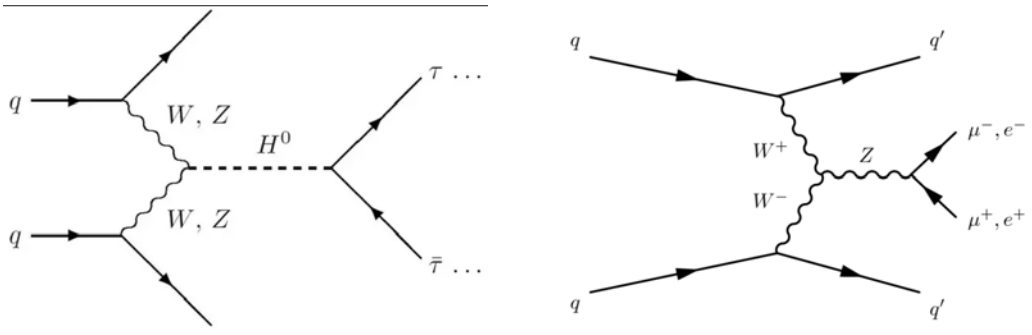

(a) (b)

Figure 4.3: VBF $H \to \tau\tau$ decay (a) and $Z \to \tau\tau + jets$ background (b) Feymann diagrams.

Existence of a jet	$n_{jets} > 0$
p_T leading jet	$p_{t_{jet1}} > 40\,\text{GeV}$
η leading jet	-4.0 $< \lvert\eta_{jet1}\rvert <$ 4.0
Existence of a second jet	$n_{jets} > 1$
p_T subleading jet	$p_{t_{jet2}} > 30\,\text{GeV}$
η subleading jet	-4.0 $< \lvert\eta_{jet2}\rvert <$ 4.0
Jets rapidity	$\lvert\Delta\eta_{jets}\rvert > 3$
Jets invariant mass	$m_{j1j2} > 400\,\text{GeV}$
Jets in two different emisphere	$\eta_{jet1} \cdot \eta_{jet2} < 0$ height

Table 4.1: Cuts used for the preliminary study presented in this chapter. Those are inspired to the ones in reference [59].

4.2.2 Monte Carlo sample production

The study presented in this document was performed using a full simulation based on GEANT4 [52, 53]. The $Z \to \tau\tau + jets$ sample was simulated with POWHEG-BOX [54, 55, 56] (v1r2856) interfaced with PYTHIA8 [57, 58] (v8.186). The study considers the QCD $Z \to \tau\tau + jets$ background only. Due to the challenge of Monte Carlo generation at $< \mu >$=200, the number of event is limited, but this study can illustrate potential gains that could be achieved once an analysis with more Monte Carlo statistic can be performed.

In this study, only three channels for the τ decays are accepted in the final state, such as $e\mu$, hh and lh for which the $Z \to \tau\tau + jets$ background is more important. The cuts listed in Table **??** and used for the selection of this sample are inspired to Run-2 analysis presented in [59]. Events are required to have at least two jets with p_T^1 >40 GeV and p_T^2 >30 GeV, both of them verifying the condition -4< $|\eta_{1,2}| < 4$. In addition, the two jets are required to have a large rapidity gap $\Delta\eta(j_1, j_2) > 3$. At the end of selection, an invariant mass $m_{j_1 j_2}$ >400 GeV and jets in two different emisphere ($\eta_{j_1} \cdot \eta_{j_2} < 0$) are required. In the following section, four baseline scenario used for the selection cuts will be presented.

Different baseline scenarios

The selection cutflow explained in the last section has been applied on four different scenarios with different starting condition, they are considered as baseline for the study of the cutflow selectionn. The four scenarios are the following:

- Scenario no ITk: all available jets are considered for the cutflow without any exception.
- Scenario ITk: the ITk detector has been turned on. This means that a cut on the reconstructed p_T of the jets is required at the beginning of the cutflow.
- Scenario ITk + remove all PU: the ITk detector has been kept on. In addition, all the Pile Up (PU) jets are rejected using truth information.
- Scenario ITk + perfHGTD: the ITk detector has been kept on. In addition, all the PU jets are rejected using truth information in the HGTD acceptance region 2.4< $|\eta|$ <4.0.

When the ITk detector is considered on, the jets are required to pass an ITk-only R_{p_T} pileup jet tagger operting at 85% hard-scattered efficiency. This means R_{p_T} >0.15. This variable is defined as in equation (3.3) in chapter 3:

$$R_{p_T} = \frac{\Sigma_k p_T^{trk_k}(PV_0)}{p_T^{jet}} \tag{4.1}$$

In the following Table 4.2, the number of entries for each of the fours baseline scenarios is shown with the cutflow inspired to Run 2 analysis. It can be seen from the cutflow number of events how the insertion of a perfect HGTD detector in the forward region 2.4< $|\eta|$ <4.0, which rejects 100% of the PU jets, reduces the number of entries of a factor ∼2.8 with respect to the ITk only scenario.

Cut	Scenario A	Scenario B ITk only	Scenario C ITk + no PUjets	Scenario D ITk + perfectHGTD
N_{events}	157762	157762	157762	157762
n_{jets} >0	136177	58263	24045	52049
$p_{T_{jet1}}$ >40 GeV	99395	39853	18485	36223
-4.0< $\|\eta_{jet1}\|$ |4.0	96295	39737	18470	36105
n_{jets} >1	81179	14338	4038	10940
$p_{T_{jet2}}$ >30 GeV	81179	14338	4038	10940
-4.0< $\|\eta_{jet2}\|$ <4.0	78055	14288	4026	10896
$\|\Delta\eta_{jets}\|$ >3	18844	2534	562	1140
m_{j1j2} >400 GeV	8743	1133	263	409
$\eta_{jet1} \cdot \eta_{jet2} < 0$	8546	1104	253	399

Table 4.2: Number of eventss for the cuts inspired to Run 2 analysis in the four baseline scenarios A, B, C and D.

Association of time information to reconstructed tracks

The algorithm used to associate the time information to a reconstructed track is based on a progressive extrapolation of tracks to the HGTD surface. Firstly, tracks reconstructed in the ITk are extrapolated to HGTD using the last measurement of the track in ITk as a starting point. With a progressive Kalman filter, tracks are extended to the HGTD surfaces. In each layer of the HGTD, clusters around the extrapolated position of the track are evaluated in order to see if they are compatible with it. Between all the spatially compatible hits, the one with the lower χ^2 is accepted as an extension of the track. This process is iterated in all the HGTD layers, always using the last step information as a starting point of the extension. In order to compare the reconstructed track time with the truth one, the individual hit times are corrected taking into account the TOF from the track origin to the hit position. A cleaning procedure is used to reduce the rate of misassociation of the track extension, the procedure removes track-times of tracks without hits on the surface close to the HGTD as well as filtering out hits that don't pass an intercompatibility check. This helps to reduce the probability of associating a random pile up time to a particle that showered before reaching the sensor surface of HGTD. The track-time is then calculated as the arithmetic mean of the times of the individual associated HGTD

hits. To reconstruct the time of the primary vertex t_0, an iterative time-clustering algorithm is used. The tracks within a window in z around the selected hard scattered vertex in the event are clustered, and checked to see if they are compatible with it. Time consistency betweek tracks and cluster is considered in a $3\sigma_t$ window, with σ_t the square root sum of the two track times under consideration. Next, a Boosted Decision Tree (BDT) algorithm is used to identify the most probable hard scattered cluster. After all the compatible tracks are chosen to belong to the cluster, the vertex t_0 is defined as weighted average time of all the tracks belonging to the cluster. The time of the jet[60] is then computed with respect to the vertex time t_0 as following:

$$t_{jet} = \sum \frac{t_{track}\ p_{Ttrack}}{\sum p_{Ttrack}} \tag{4.2}$$

for the sample under study, the time information is provided in the 60% of the total cases. The reconstructed time of the jet is then calculated for all the jet in the HGTD acceptance region for which time information is provided. A distribution of the jet time calculated with respect to the internal t_0 is shown in Figure 4.4 (a) for the ITk only scenario at the end of the cutflow. For each iteration the resolution is calculated as:

$$reso_{t\ jet} = \frac{\sqrt{\sum (reso\ t^2_{track} \times pT^2_{track})}}{\sum pT_{track}} \tag{4.3}$$

whose distribution is shown in Figure 4.4 (b). In addition, jets significance has been defined as:

$$sign_{jet} = \frac{t_{jet}}{reso_{t\ jet}} \tag{4.4}$$

with its distribution shown in Figure 4.4 (c). New scenarios where cuts on the significance distribution are considered will be presented in the next section, in order to study a more realistic impact of the HGTD.

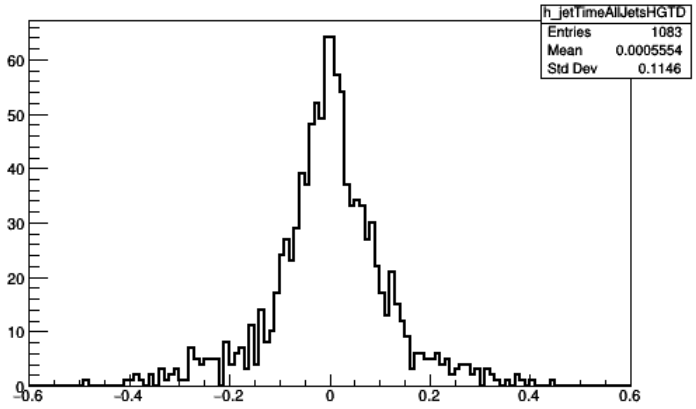

(a)

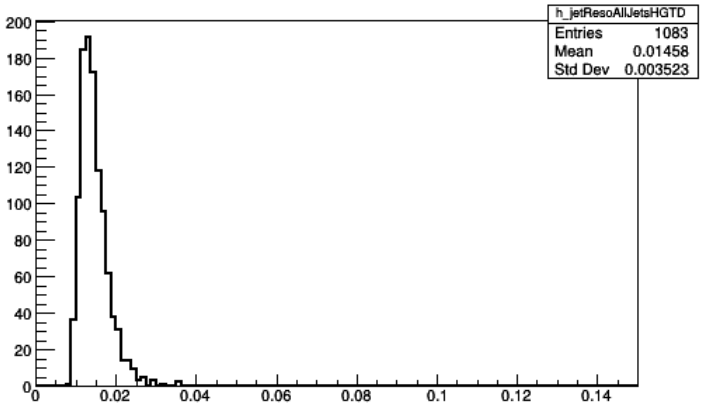

(b)

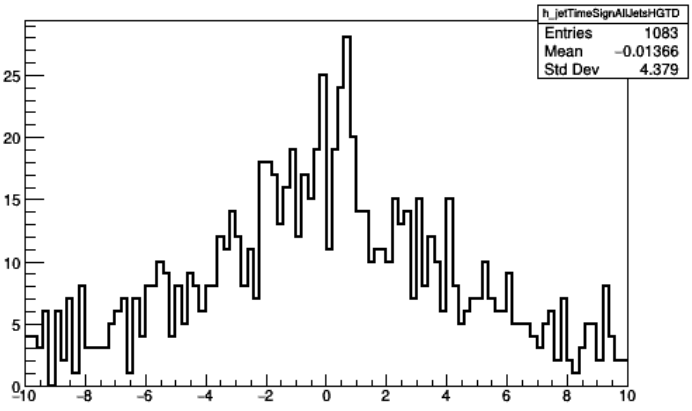

(c)

Figure 4.4: Jet time distribution respect to the internal time t_0 (a) and jet resolution distribution (b) for the jets at the end of the cutflow in the ITk only scenario. In Figure (c), a distribution of the significance of the jets in the same conditions.

Insertion of time for jets

The insertion of a time information for the jets bring us to make other consideration on a more realistic approach for the HGTD detector in the rejection of PU jets. Three new scenarios are considered, for which the time information is used in the jets rejection process. As a common baseline, the ITk detector is considered to be on as in Scenario B of the previous section. The scenarios where time information is considered are the following:

- HGTD1σ: PU jets for which time is $\pm 1\sigma$ away on the jet time significance are rejected.

- HGTD1.5σ: PU jets for which time is $\pm 1.5\sigma$ away on the jet time significance are rejected.

- HGTD2σ: PU jets for which time is $\pm 2\sigma$ away on the jet time significance are rejected.

The corresponding cutflow for the different timing scenarios can be seen in Table 4.3, where the cutflow for the ITk only scenario and for the perfect HGTD ones also given. It can be seen from the number of events in the cutflow how, with respect to the ITk only scenario, the HGTD 1σ scenario gives a reduction of events with a factor $\sim$2.59, the HGTD 1.5σ gives it with a factor $\sim$2.3 and the HGTD 2σ with a factor $\sim$2.05 In Figure 4.5, distribution for both leading (left) and subleading (right) jets both at beginning (top) at the end of the cutflow (bottom) are shown for a comparison between the ITk only scenario, the perfect HGTD and the HGTD 2σ ones. In these plots it can be seen how much the PU jets in the forward region are reduced in the three different scenarios.

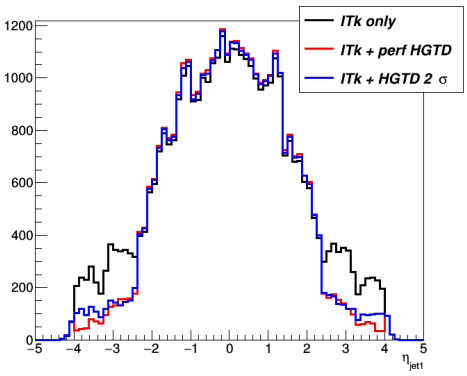

(a)

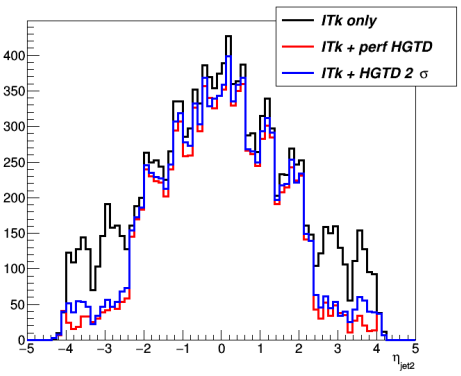

(b)

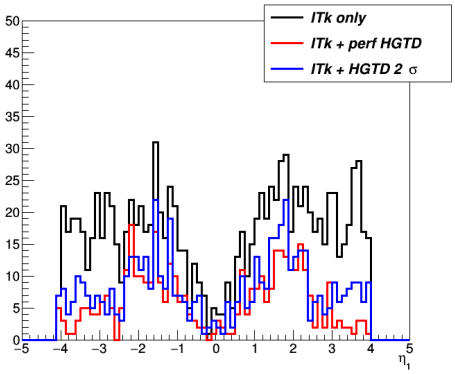

(c)

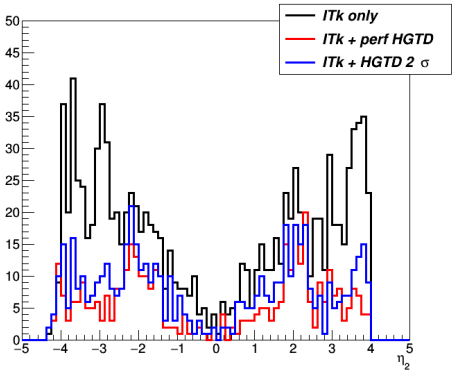

(d)

Figure 4.5

Cut	ITk only	Perfect HGTD	HGTD 2σ	HGTD 1.5σ	HGTD 1σ
N_{events}	157762	157762	157762	157762	157762
n_{jets} >0	58263	52049	53160	52599	51964
$p_{T_{jet1}}$ >40 GeV	39853	36223	36570	36182	35742
-4.0< $\lvert\eta_{jet1}\rvert$ |4.0	39737	36105	36452	36064	35624
n_{jets} >1	14338	10940	11577	11291	10971
$p_{T_{jet2}}$ >30 GeV	14338	10940	11577	11291	10971
-4.0< $\lvert\eta_{jet2}\rvert$ <4.0	14288	10896	11533	11247	10927
$\lvert\Delta\eta_{jets}\rvert$ >3	2534	1140	1453	1343	1230
m_{j1j2} >400 GeV	1133	409	553	493	433
$\eta_{jet1} \cdot \eta_{jet2} < 0$	1104	399	537	480	426

Table 4.3: Number of events for the cuts inspired to Run 2 analysis in the three different HGTD timing scenarios, compared also with the ITk only (B) and perfect HGTD ones.

Conclusions

A simplified VBF jet selection based on full jet reconstruction information has been applied to a QCD Z + jets Monte Carlo Sample. The original purpose of the study was VBF H -¿ tau tau but the results applied to any physics channel in which QCD Z + jets is a dominant background. The ideal performance of HGTD can be checked with truth information and it has been estimated that the background reduction is a factor XXX with respect to ITk only scenario. The use of timing information has been shown to be very effective in suppressing QCD Z + jets events, with a reduction of XXX with respect to ITk only scenario when discarding jets with time significance greater that two. The potential of this method will be evaluated a VBF H -¿ invisible signal sample.

A simplified $VBF\ H \to \tau\tau$ cutflow selection based on full reconstruction information of jets in the event has been set up for a MonteCarlo sample $Z \to \tau\tau + jets$. Using truth information it was possible to suppress PU jets, where maximum suppression is given when all the PU jets in ATLAS have been removed from the ITk only scenario chosen as baseline.

Respect to the ITk only scenario, the insertion of a perfect HGTD detector would be

able to suppress PU jets by a factor ∼2.8 on the number of events.

The use of time information associated to charged tracks in jets made possible to estimate a more realistic effect of the HGTD detector on the reduction of the $Z \rightarrow \tau\tau + jets$ background as it was shown in the previous section.

The very important aspect of the effect of the HGTD on the $H \rightarrow \tau\tau$ signal remains to be studied. Unfortunately, the eventual production of MonteCarlo samples for the $H \rightarrow \tau\tau$ signal channel was not compatible with the timescale of this thesis.

Chapter 5

Sensor Technology: from Solid State Detectors to Low Gain Avalanche Detectors (LGADs)

Solid state detectors have been introduced in the field of experimental particle physics since 1970s. In the following decades they become more and more common thanks to their outstanding performances in terms of position resolution and radiation hardness, which are crucial factors for HEP experiments. Nevertheless, gas-based tracking detectors have not been totally replaced by solid state detectors, since their cost make them more suitable for outer layers of big experiments. This is the case of the LHC, where large volumes have to be covered and time resolution and radiation requirements can be relaxed as the distance from the IP increases.

In the past decades the scientific community made many progress in the solid state detectors field. To meet the demands of experiments the manufacturing techniques also improved allowing to produce different thickness wafers and detectors with finer segmentation and better radiation hardness performances. At the same time, the progress of ASICs from electronic industry has been crucial to provide an adequate

readout system.

In the first part this chapter, the fundamental aspects of silicon detectors will be summarized. In the second one, an overview on the LGAD technology, with which the HGTD detector will be instrumented as said in Chapter 3, will be presented.

5.1 Solid State Detectors

In solid state detectors the signal is generated by the current associated to the drift of ionization charged produced by the passing of a charged particle through the sensor. Their characteristics such as high density, fast readout and high segmentation make them suitable for high energy particle detection of collider experiments.

5.1.1 The band model

The fundamental theory below the solid state detector is the band model of solids. The discrete energy levels of the atoms in which electrons are confined are called bands. Due to Pauli exclusion principle, each band can host a finite number of electrons. Thus, the lowest energy level are fully filled, while bands above a certain limit will not be occupied. The highest fully filled energetic band is the so called valence band, while the next higher level which is partially filled or empty is the so called conduction band. When this last band is partially filled the electrons of the material are free to move in the crystalline lattice and the solid is a conductor. In the other case, the energy gap $E_g = V_C - V_V$ between valence and conduction bands defines if the material is a conductor or insulator [61]. The most common semiconductor used in radiation detector is Silicon, for which $E_g \sim 1.2\,\text{eV}$ and $3.6\,\text{eV}$ are needed to create an $e - h$ pair, as it will be discussed in the next section. Both electrons and holes contribute to the charge carrier concentration inside the material. Electrons can be excited from the valence to the conduction band moving freely in

the crystal lattice and leaving vacancies in their original position. Holes, move in the crystal lattice as well, acting as positive charges. Through thermal excitation $e-h$ pairs are continuously generated as well as destroyed, since they recombine between themselves. In general, the concentration of electrons in the conduction band can be calculated with the following equation:

$$n = \int_{E_C}^{\infty} g_e(E) f(E) dE \tag{5.1}$$

with $g_e(E)$ density of states, $f(E)$ the Fermi-Dirac distribution and integral calculated from the minimum energy level E_C to infinity. In a similar way, the concentration of holes can be calculated, this time integrating from zero the the energy of the maximum energy level in the valence band:

$$p = \int_{0}^{E_V} g_h(E) f(E) dE \tag{5.2}$$

The Fermi-Dirac distribution used in both calculations is given by:

$$f(E) = \frac{1}{1 + e^{(E-E_F)/k_B T}} \tag{5.3}$$

with k_B the Boltzmann constant, T the absolute temperature and E_F the Fermi energy, which for a semiconductor is placed approximately at the middle of the energy gap:

$$E_F \sim \frac{E_C - E_V}{2} \tag{5.4}$$

Is it possible to calculate the density of states for both electrons and holes assuming them free to move inside the semiconductor but cannot escape it. This is represented by an infinitive potential box which can be written as:

$$g_e(E) = \frac{1}{2\pi} \left(\frac{m_n}{\hbar^2}\right)^{3/2} \sqrt{E - E_C} \text{ with } E \leq E_C \tag{5.5}$$

$$g_h(E) = \frac{1}{2\pi} \left(\frac{m_h}{\hbar^2}\right)^{3/2} \sqrt{E_V - E} \text{ with } E \geq E_V \tag{5.6}$$

where m_n and m_h are the effective masses of electrons and holes[1], and $\hbar$ the reduced Planck constant. From the integral of equations 5.1 and 5.2 the electrons and holes concentration can be calculated:

$$n = 2\left(\frac{m_n k_B T}{2\pi\hbar^2}\right)^{3/2} e^{-(E_C - E_F)/(k_B T)} = N_C e^{-(E_C - E_F)/(k_B T)} \tag{5.7}$$

$$p = 2\left(\frac{m_p k_B T}{2\pi\hbar^2}\right)^{3/2} e^{-(E_F - E_V)/(k_B T)} = N_C e^{-(E_F - E_V)/(k_B T)} \tag{5.8}$$

with N_C and N_V the effective density of states in the conduction and valence band. The product of electrons and holes density gives:

$$np = n_i^2 = N_C N_V e^{-E_g/k_B T} \tag{5.9}$$

where n_i is the intrinsic charge carrier concentration[2], and E_g the energy gap. Typical values for n_i in silicon at room temperature are of the order of $1.5 \times 10^{10}\text{cm}^{-3}$ [62].

5.1.2 Addition of doping materials

The balance between the two charge carries in intrinsic semiconductor can be modified with the addition of a doping material to the pure crystal. With the introduction of atoms with one more on one less valence electron creates an excess of electrons or holes. From the silicon band structure point of view, doping process can consist of introducing an element with more valence electrons (n-type) or more holes (p-type). Elements which are used with silicon are:

- n-type: elements from the group V of the periodic table, such as Phosphorous or Arsenic. These elements introduce an extra electron in the conduction band and are called *donors*.
- p-type: elements from the group III of the periodic table, such as Boron and

[1]For Silicon at T=300 K: m_n =1.09m_e and m_h =1.15m_e with m_e being the mass of the electron.
[2]For semiconductor, the assumption $n = p = n_i$ is made.

Gallium. These elements introduce an energy level above the valence band that can be populated by free electrons creating an excess of holes. Due to this reason, they are called *acceptors*.

Acceptors (donors) add an energy level above (below) the valence (conduction) band, which is called E_A (E_D), as shown in Figure 5.1.

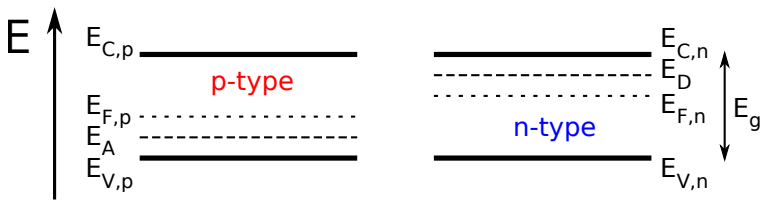

Figure 5.1: Energy levels for p-type (left) and n-type (right) silicon. In the p-type silicon, another energy level E_A slightly above the valence band energy is added, while in n-type silicon an energy level E_D slightly below the conduction band energy is added. The Fermi Energy E_F is close to the middle of the band gap and shifted towards the energy level introduced by the doping. Picture taken from [63].

Doped semiconductor remain electrically neutral, since the electric charge of the extra electrons or holes is balances by the nuclei having one more or less proton than silicon. The sum of positive and negative charges is then equal. If N_A and N_D are the acceptors and donor concentration, this can be written as:

$$N_D + p = N_A + n \tag{5.10}$$

In a p-type semiconductor $p \gg n$ and $N_D = 0$. Combining 5.10 with 5.9 the charge carrier density can be written in terms of dopant concentration as

$$p \simeq N_A \text{and} n \simeq \frac{n_i^2}{N_A} \tag{5.11}$$

On the other hand, in a n-type semiconductor $n \simeq N_D$ and $p \simeq n_i^2/N_D$. This means that in a doped semiconductor the concentration of the majority charge carriers in approximately equal to the dopant concentration. Drift velocity of electrons and holes

under the electric field E will be:

$$v_{e/h} = \mu_{e/h} E \tag{5.12}$$

with $\mu_{e/h}$ the mobility of electrons or holes. For a high purity silicon at room temperature, these values are $1350\,\mathrm{cm}^2/\mathrm{Vs}$ and $450\,\mathrm{cm}^2/\mathrm{Vs}$ respectively [62, 64]. The drift velocity reaches a saturation value for large electric field. In an intrinsic semiconductor electrons and holes have the same density n_i and both contributes to the current density as $J = en_i(\mu_e + \mu_h)E$. The current density can be expressed as $J = E/\rho$ where ρ the resistivity, which can be written as

$$\rho = \frac{1}{en_i(\mu_e + \mu_h)} \tag{5.13}$$

In doped semiconductors the current contribution of the minority charge carriers can be neglected and the charge carrier density can be replaced by the dopant density as in equation (5.11). From 5.13 can be written

$$\rho_{n-type} = \frac{1}{eN_D\mu_e} \tag{5.14}$$

$$\rho_{p-type} = \frac{1}{eN_A\mu_h} \tag{5.15}$$

Both intrinsic and doped semiconductor have a too large density of free carries in order to be used as particle detectors. Although, combining semiconductors with opposite doping, a region without free charges can be created and exploited for particle detection. This is the principle of what is called the *pn*-junction, which will be discussed in the following section.

5.1.3 The *pn*-junction

When two semiconductor with opposite doping are in contact, a *pn*-junction is formed. This behaves as a semiconductor diode and ideally it has zero resistance when forward

bias is applied and infinite resistance when reverse bias is applied. Due to the difference in carriers concentration at the junction interface, electrons from the n-doped region diffuse to the opposite p-doped region and recombine with the holes. In this way, the semiconductor which was initially neutral become charged because of the charge flow from one side to the other of the junction. The p-doped region acquires a negative charge while the n-doped region acquires a positive one. This creates a region that is free of charge carriers and is called depletion zone. Since it is surrounded by donors and acceptors which do not recombine, an electric field is created across the junction, that counterbalance the charge migration pushing away the eventual free charges in this volume. This electric field is characterized by a *built-in voltage* V_{bi} as shown in Figure 5.2.

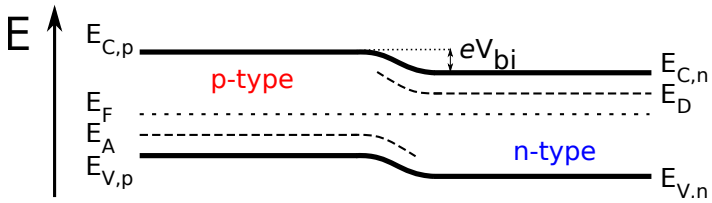

Figure 5.2: Energy levels of a p-n junction. The Fermi energy E_F is at the same level for the p-type and the n-type silicon, thus creating a zone where the conduction and valence bands are bent. This energy shift creates the built-in voltage V_{bi} in the central area (depletion zone). Picture taken from [63].

The *pn*-junction is at the base of any semiconductor detector. It generates a region with no free charge that can be altered using different geometries and applying an external bias voltage. The ionizing radiation passing through the depletion zone creates electron-hole pairs which are separated by the presence of the electric field in the region generating a current which is characteristic of the passing of the particle through the detector.

In principle, the depletion zone can be made thinner or wider applying direct or reverse bias voltage. Generally, a reverse bias voltage is applied. In this way, holes in the p-doped region are attracted towards the electrode outside the depletion zone and the same happens for electrons in the n-doped region. Since only the charges

which are generated in the depletion zone contributes to the signal, the application of a reverse bias improves the intrinsic performance of the junction as a detector. The width of the depletion zone can be expressed as:

$$d = \sqrt{\frac{2\epsilon}{e}\frac{N_A + N_D}{N_A N_D} V_{bi}} \approx \sqrt{\frac{2\epsilon}{eN_{D/A}} V_{bi}} \text{if} N_A \gg N_d \text{or} N_A \ll N_D \tag{5.16}$$

with ϵ the dielectric constant, V the applied voltage, e the electron charge, N_D and N_A the dopant concentrations of donors and acceptors. In order to increase the depletion zone and to allow detecting particles with larger signals, an additional external reverse bias voltage can be applied. In this way the depletion zone size changes following:

$$d = \sqrt{\frac{2\epsilon}{eN_{D/A}}(V_{bi} + V_{bias})} \tag{5.17}$$

where V_{bias} is the required voltage to deplete the full thickness of the diode, also called *depletion voltage*. The resistivity of a semiconductor can be expressed as

$$\rho_{n/p-type} = \frac{1}{eN_{D/A}\mu_{e/h}} \tag{5.18}$$

Equation 5.17 can be expressed in terms of ρ using equation 5.18:

$$d = \sqrt{2\mu_{e/h}\epsilon\rho(V_{bi} + V_{bias})} \tag{5.19}$$

Thus, the depletion dept at same bias voltage is bigger on higher substrate resistivities. The depletion depth is also growing into the less doped region of semiconductor.

As said, electrons and holes are continuously generated by thermal excitation in a semiconductor. Usually they recombine between themselves but, if they are generated inside the *pn*-junction, they are drifted apart by the electric field contributing to a current called leakage current. This quantity depends linearly on the depleted volume and increases with $\sqrt{V}$. Its relation with temperature is given by the following

equation:

$$I_{leak} \propto T^2 e^{-E_g/2kT} \tag{5.20}$$

meaning that leakage current is lower at lower temperatures. This is extremely important in the case of irradiated devices, where radiation induced damage in the bulk leads to large leakage currents and consequently to larger noise. In Figure 5.3 the leakage current for a *pn*-junction is shown: when the reverse bias of the junction increases, the electric field gets stronger and this creates a larger depleted region, improving the performances of the junction as a particle detector. After a value named breakdown voltage V_{bd} the diode breaks down and starts becoming conductive. This value defines the maximum applicable bias value. In the following section, silicon

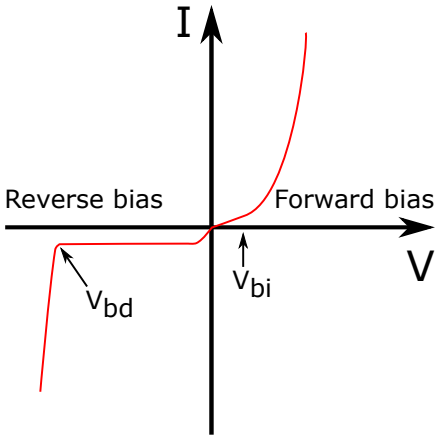

Figure 5.3: Leakage current as a function of the bias voltage for a p-n junction. In reverse bias the leakage current does not change over a large voltage until the breakdown voltage V_{bd} where it rises exponentially. In forward bias the current rises linearly until the intrinsic in-build voltage V_{bi} is overcome. Afterwards, the current rises exponentially. Picture taken from [63].

detectors, which are based on the *pn*-junction described here, will be investigated

5.2 Silicon detectors

As explained in the previous section, the core element of a silicon detector is the reverse biased *pn*-junction, where electron-hole pair are created by ionizing particles

passing through the detector and collected by the n and p doped regions that acts as electrodes. Usually, n-doped and p-doped regions are called n^+ and p^+ respectively. In Figure 5.4 a sketch of a basic silicon detector with p-type bulk is shown. What

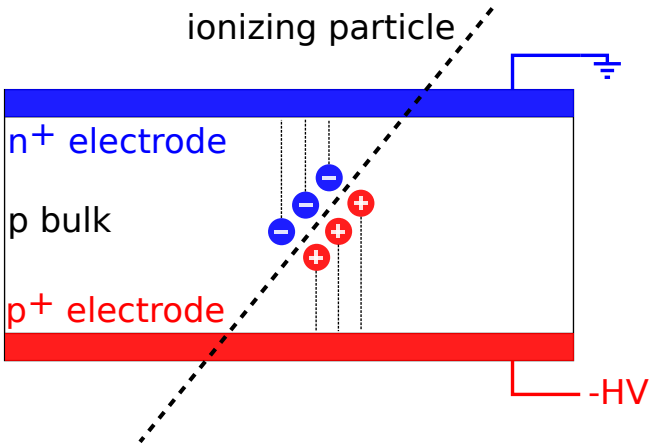

Figure 5.4: Sketch of a n-on-p pad diode with ionizing particle creating e/h pairs in the bulk that are collected by the electrodes. Picture taken from [63].

makes silicon detector popular for HEP, beyond their radiation hardness, is the possibility to have highly segmented electrodes. If the detector is left unsegmented, it is considered as a pad diode (as the one shown in Figure 5.4). This is usually used for prototype tests or for application where segmentation is not required. If the electrode is segmented in parallel strips the detector is called strip detector. The readout system is then connected to the end of each strip. This kind of detector are usually used to get position information with high resolution. To have position information the information between two not aligned strips is combined. In the case of more than one parallel strips having signal, this can lead to an ambiguity on the reconstructed position even with the insertion of a second information from a not aligned strip. This can be solved through pixels detectors, where the electrode is segmented in both directions generating a matrix of pixel. In this way, each pixel had a 2D information on the hit position resolving possible ambiguities existing for strips detectors in a particle crowded environment.

Although, the number of electronic channels needed to readout the sensor is much

higher in a pixel detector than in a strip one covering the same size. Traditionally, a readout chip is pixel-by-pixel interconnected to the sensor through a process called bump-bonding, making what is called a hybrid detector, as it was shown for the HGTD module in Chapter 3.

Signal generation by charged particles

When charged particles pass through matter, they interact with atoms of the material losing part of their energy. They can lose energy both interacting with electrons of the atoms or with their nuclei, being these processes called ionizing or non-ionizing energy loss. The ionizing loss is the responsible of the creation of the electron-hole pairs, while the non-ionizing one introduces defects in the crystal and is the origin of radiation damage, which will be discussed in Section 5.2.3 of this Chapter. For relativistic charged particles in the energy range $0.1 \leq \beta\gamma \leq 1000$ the mean rate of the energy loss is described by the Bethe-Bloch equation:

$$\left\langle -\frac{dE}{dx} \right\rangle = Kz^2 \frac{Z}{A} \frac{1}{\beta^2} \left(\frac{1}{2} \log \frac{2m_e c\beta^2\gamma^2 T_m ax}{I^2} - \beta^2 - \frac{\delta(\beta\gamma)}{2} \right) \tag{5.21}$$

where $K = 4\pi N_A r_e^2 m_e c^2$ with N_A the Avogadro's number, r_e the classical electron radius and $m_e c^2$ the rest mass of the electron, Z is the atomic number, A the atomic mass, I is the mean excitation energy of the medium , T_{max} is the maximum transferable energy in a single collision, $\beta = v/c$, $\gamma = 1/\sqrt{1-\beta^2}$ is the Lorentz factor and $\delta(\beta\gamma)$ is a correction factor for high energy particles. In Figure 5.5 the energy loss for muons, pions and protons in silicon is shown.

Equation 5.21 has a minimum for $\beta\gamma \sim 3$ that hardly increases over some order of magnitude. In this way, high momentum particles still can be considered as a *mip*. For a large momentum range, these particles lose a small fraction of their energy travelling through the material and can be considered as *mip*s for the entire process. In silicon, a *mip* has an average stopping power $\langle \frac{dE}{dx} \rangle = 1.66\,\mathrm{MeVcm^2/g}$.

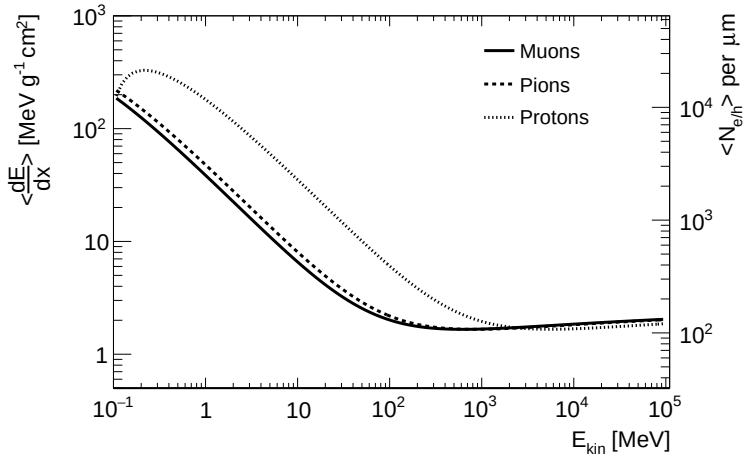

Figure 5.5: Average stopping power for muons, pions and protons in silicon as a function of the kinetic energy. The average number of created electron/hole pairs for micrometer is also shown. Picture adapted from [65].

The energy loss probability distribution is described by a Landau distribution. This distribution is asymmetric with a long tail, shifting the mean energy loss to higher value. The most probable energy loss is

$$\Delta_p = \xi \left[\ln \frac{2mc^2\beta^2\gamma^2}{I} + \ln \frac{\xi}{I} + j - \beta^2 - \delta(\beta\gamma) \right] \tag{5.22}$$

where $\xi = (K/2)/A\rangle z^2(x/\beta^2)$ MeV for a detector with a thickness x in g cm^{-2}. The energy loss in a detector is function of the energy of the passing particle and of detector thickness, with $\Delta_p \propto a \ln x + b$. The energy deposited by ionization generates a number of electron-hole pairs proportional to the detector thickness and inversely proportional to the energy needed to create an electron-hole pair. The distribution of the deposit energy and the Most Probable Value (MPV) scaled to the mean energy loss of a *mip* in silicon for several thicknesses are shown respectively in Figure 5.6 (a) and (b).

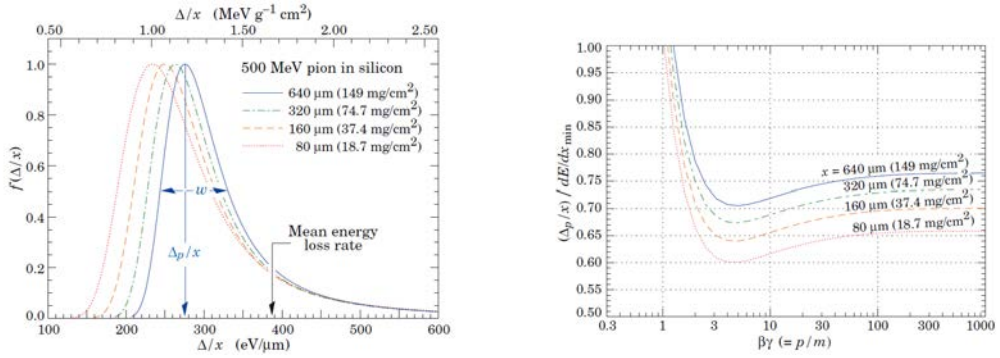

(a) (b)

Figure 5.6: (a) Landau distribution of the deposited energy by 500 MeV pions in silicon for different silicon thicknesses. Distribution are normalized to the most probable value of each distribution. (b) Most probable energy loss scaled to the mean energy loss of a *mip* in silicon for different thicknesses of silicon substrate. Pictured from [66].

5.2.1 Signal generation by photons

The interaction of photons in solid state detectors have to be treated in a different way. Photons, differently from charged particles, do not interact along their path but have a probability to be absorbed that depend on the material and thickness and on the photon energy. The different processes with which photons interact are the following:

- *Photoelectric Effect*:photon is absorbed by an atom which releases an electron whose energy is equal to the energy of the impinging photon minus the ionizing energy. The cross section of this process depends on the atomic number ($\sigma_{pe} \propto Z^n$ with n from 4 to 5), favouring atoms with higher Z. This effect dominates at energy $\leq$100 keV after which it decreases of several order of magnitude.

- *Compton Scattering*:in the energy range between $\sim$ 100 keV and $\sim$ 10 MeV Compton scattering between the photon and an atomic electron is the main process which interest photons. The final state consists of a lower energy photon and a recoil electron with direction and energy defined by the momentum conservation.

- *Pair Production*: if the photon energy is larger than twice the electron mass (1.022 MeV), e^+/e^- pairs can be created in the interaction with the material.

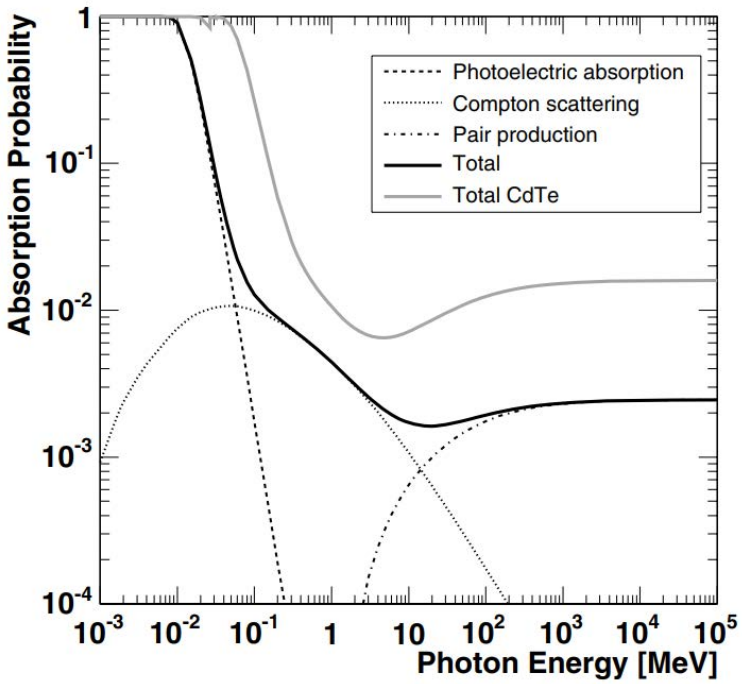

Figure 5.7: Absorption probability of photons in 300 µm silicon as a function of the photon energy. The three contribution from photoelectric effect, compton scattering and pair production are shown. From [67].

5.2.2 Detector Applications

In the high energy physics community silicon detectors are used for different applications. In particular, the possibility to have segmented electrodes have been exploited to produce position sensitive detector for tracking application. In addition, the short charge collection time gives to these detectors a good time resolution when coupled to a suitable readout electronics. In this section, tracking and timing application will be briefly discussed.

Tracking applications

Thin devices with an electrode segmentation in the order of tens of micrometer are suitable for tracking applications. The energy deposited by a *mip* is typically a small fraction of the particle energy, making possible to reconstruct the particle trajectory with several layers of silicon detectors. The ionizing particle will leave a signal in each layer and the position resolution will depend on the electrode segmentation, with better resolution with finer electrodes. Within one pixel is not possible to understand where the particle crossed, thus its position is reconstructed with a, uncertainty which depends on the pixel pitch in each direction. The resolution is given by the standard deviation of the uniform distribution $\sigma = pitch/\sqrt{12}$.

If the particle leaves a signal in more than one pixel, contiguous fired pixels are clustered, and the assigned position depends on the cluster algorithm that is used. Usually, a TOT is recorded by the readout electronics, as a time for which the signal has been larger than the threshold. The TOT is connected with the particle deposited charge in the pixel, which can be used to improve the cluster algorithm.

Timing applications

As already introduced, the design of silicon detectors can be optimize in order to get detectors with a good time resolution. The time resolution of a silicon sensor is given by equation:

$$\sigma_t^2 = \sigma_{Time\ Walk}^2 + \sigma_{Landau}^2 + \sigma_{jitter}^2 + \sigma_{TDC}^2 \tag{5.23}$$

where the time walk, jitter and TDC contributions have been already discussed in Chapter 3.

The Landau term σ_{Landau} takes into account the contribution to the time resolution given by the fluctuation in the density of generated charge. When a *mip* passes through the detector, it deposit energy along its path experiencing a number

of primary interactions, generating a localized cluster of electron-hole pairs for each primary interaction. The signal pulse is then given by the sum of each cluster contribution, drifting under the effect of the electric field. The pulse shape depends on the primary cluster distribution. Its fluctuations affect the time resolution of the sensors. When the bias voltage is sufficiently large, the drift velocity of both electrons and hole saturates, thus the duration of the signal scale with the detector thickness. In this way, also the effect of the signal duration on the time resolution is reduced as well. Thus, the Landau term of time resolution can be reduced reducing the sensor thickness [68].

In conclusion, a good time resolution for a silicon detector can be achieved in the order of tens of picosecond, if the Landau term is reduced minimizing the active thickness of the sensors, the electronics is optimized in order to reduce the time walk and the TDC contributions. In addition, for this devices with charge multiplication improve the S/t_{rise} ration which brings benefits to the jitter and time walk distributions, as explained in Chapter 3. Such devices have been produced based on the LGAD technology in the context of the HGTD detector. The sensors will be discussed in Section 5.3 of this Chapter, and their performances will be presented in Chapter 6.

5.2.3 Radiation damage

Silicon detectors used in HEP experiments are usually exposed to high flux of particles (or high level of radiation), thus is important to understand how the radiation acts on the detector performances. As said, particles penetrating a detector can deposit energy through non-ionizing processes as well, interacting with atoms of the crystal. The resulting radiation damage effects are classified as *bulk effects* or *surface effects*. Usually the bulk effect are the main contribution on the performances deterioration of silicon sensors, while the surface effects tend to be important for the readout electronics. In this section, bulk effect will be described. When a particle passes

through the sensor and deposit energy, if the transferred energy is higher than 25 eV the nucleus can be displaced from its position, producing what is called as a bulk defect, and eventually also displaced nuclei of neighbouring atoms as well (cluster defect). This results in a silicon interstitial and a left over vacancy. It can be partially recovered with annealing, but has a permanent effect which is the introduction of new energy levels that modify the effective doping and can potentially act as generation or recombination centers. The induced damage in the silicon lattice differs from particle type and energy. In a collider experiment such as ATLAS, a wide spectrum of particles of a broad range energy interact with the detectors. An absolute measurement of the radiation induce damage can be obtained through the Non-Ionizing Energy Loss (NIEL) hypotesis [69].

The NIEL Hypotesis

The NIEL hypothesis assumes that the damage of any particle at a given fluence Φ_{eq} can be calculated by:

$$\phi_{eq} = k\Phi = k \int_{E_{min}}^{Emax} \Phi(E) dE \tag{5.24}$$

where k is the hardness factor that scales the displacement damage of each particle and energy to 1 MeV neutron equivalent. The hardness factor k can be written as:

$$k = \frac{\int_{E_{min}}^{Emax} D(E)\Phi(E) dE}{D(E_n = (1\,\mathrm{MeV})) \int_{E_{min}}^{Emax} \Phi(E) dE} \tag{5.25}$$

where the fluence is weighted with the energy dependent displacement damage cross section D(E) (see Figure 5.8) and normalized to the integrated fluence at the damage cross section of the reference particle. Using the NIEL hypothesis is then possible to evaluate the 1 MeV neutron equivalent fluence on a detector at any point of its lifetime in the experiment. This allows to evaluate the behavior of sensors in the experiment studying the damages on sensors exposed to different fluences. In this thesis, several irradiation campaign to study performances of silicon sensors have been carried out

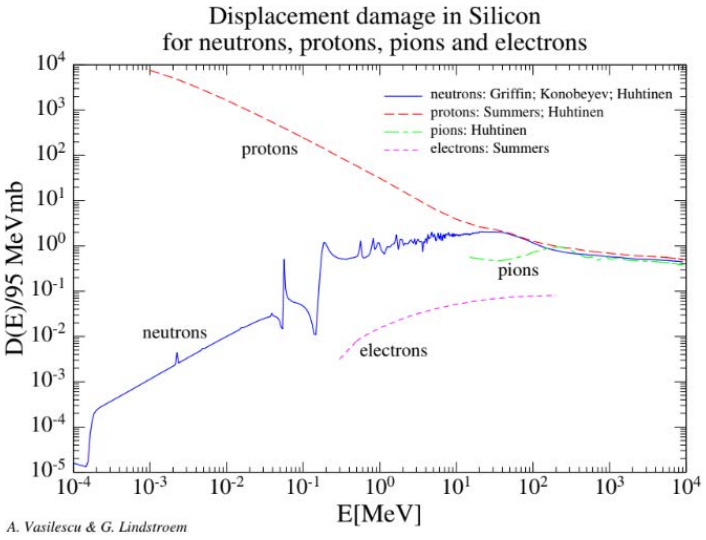

Figure 5.8: Displacement damage cross section $D(E)$ as a function of particle energy for electrons, pions, protons and neutrons, normalized to 1 MeV neutron. Adapted from [70].

with 1 MeV neutrons in the TRIGA reactor of the Jožef Stefan Institute (JSI) in Ljubljana (k =0.9), some sensors were also irradiated aProton Syncrotron (PS) at CERN with protons (k =0.7). From now on, all the fluences will be quoted in 1 MeV equivalent in the rest of the thesis.

Doping Concentration

In the detector bulk the radiation damage can be described as a change on the effective doping of the sensor. On unirradiated devices, the effective doping of a *p-type* sensor can be described as the difference of the acceptor and donor dopants concentrationn $N_{eff,0} = N_a - N_D$. After irradiation, detector irradiated to a fluence Φ presents an effective doping of:

$$N_{eff}(\Phi) = N_{eff,0} - N_c(1 - e^{-c\Phi}) + g_c\Phi \tag{5.26}$$

where N_c and c describe the size and speed of acceptor removal phenomenon which reduces the doping concentration, and g_c decribes the radiation induced acceptor

creation in the bulk [71].

Trapping

The charged defects in the bulk can also act as trapping centres for charge carriers. As a consequence, the collected charge Q during drift time is reduced. This can be expressed as a function of the fluence in the folloing way:

$$Q(\Phi) = Q_0 e^{-t_c/\tau} \text{ with } \tau = \beta_T \Phi \tag{5.27}$$

with Q_0 the initial charge (as the one of unirradiated device), t_c the charge collection time and τ the trpping time. τ is inversely proportional to the fluence by a factor β_T that depends on the charge carrier type and on radiation type, i.e. if is neutron or charged hadrons [72]. Even if the trapping time is similar for electrons and holes, trapping is more effective on holes since their collection time is higher than the one of electrons because the different mobility. Thus, holes contribution to the signal will eventually become negligible at high enough fluence.

Leakage Current

As said previously in this section, the bulk damage induced by radiation creates new energy levels in silicon. When these energy levels are created within the band gap, the energy to promote an electron to the conduction band and then act as a generation centre is also reduced. The effect is an increasing of the leakage current I_{leak} that is proportional to the fluence and to the depleted volume V:

$$I_{leak}(\Phi) - I_{leak}(0) = \alpha \Phi V \tag{5.28}$$

where α is a proportional factor known as the current-related damage rate. From Figure 5.9, the value for α after an annealing of 80 minutes at 60 °C is 3.99× [73].

The leakage current in the sensor depends strongly on the operational temperature, as

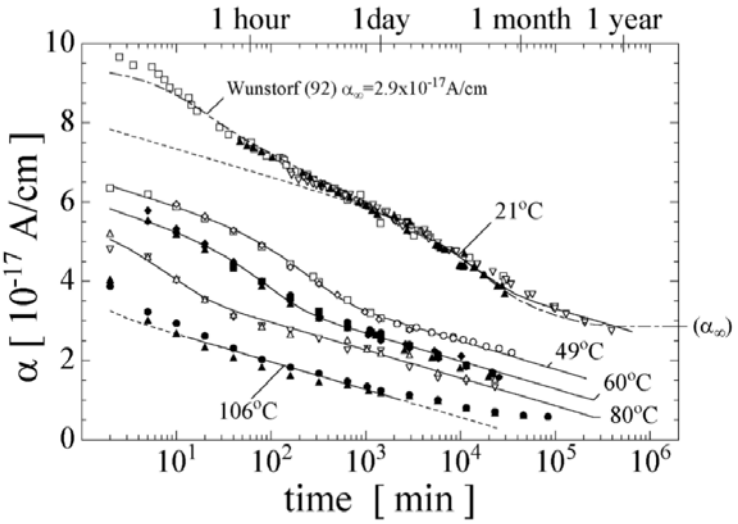

Figure 5.9: Simulation (dashed lines) and measurements (points) of the current-related damage parameter α time evolution for different annealing temperatures. Adapted from [73].

already shown in equation 5.20. Although, on irradiated devices a self-heating effect could be present due to the increasing of the leakage current, which generates an increase in the device temperature leading to a *thermal runaway* that can potentially destroy the device. In order to avoid this, irradiated devices can be operated at cold temperatures to compensate the effect of the increase of the leakage current and the consequent power consumption. In this work, all the measurements for irradiated devices whose results are presented in Chapter 6 have been performed at $T = -30\,^{\circ}\mathrm{C}$[1] for this purpose and to mimics the operational temperature of the HGTD detector.

Annealing

The bulk defects induced by radiation are not static, but they can move within the crystal. During this they can react with other defects or impurity and also eventually form new defect structure. This process is called annealing. Its evolution depends on the temperature and can be accelerated warming up the silicon sensor, or slowed

[1] $T = -20\,^{\circ}\mathrm{C}$ when was not possible to reach lower temperatures.

down cooling it [73]. As shown in Figure 5.9, the annealing is always beneficial on the current-related parameter α, mitigating the increasing of the leakage current induced by radiation. On the effective doping concentration N_{eff}, initially annealing has a beneficial effect, which is given by a reduction of N_{eff} that results in a larger resistance and in a larger depletion depth at the same bias voltage. Afterwards, instead, the effect is opposite with a long term reverse annealing where N_{eff} is pushed to larger values, as shown in Figure 5.10. Irradiated silicon sensors are annealed usually for 80 minutes at 60 °C before the rise of the reverse annealing. After that, they are kept at low temperature both during operation and storage.

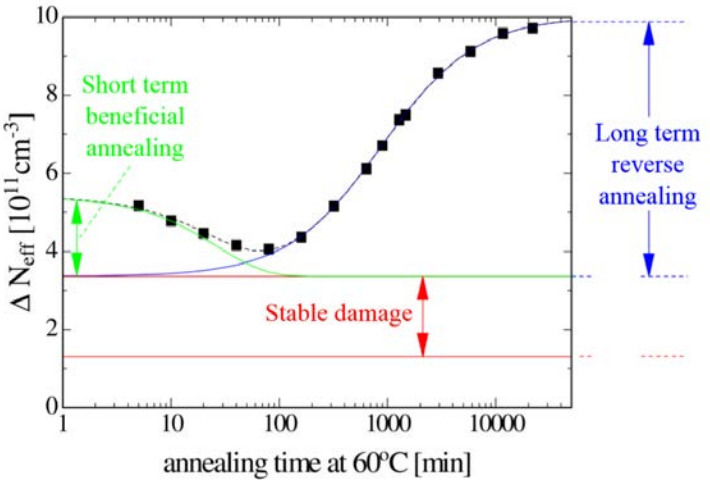

Figure 5.10: Evolution of the radiation induced change in the effective doping concentration $_{eff}$ with respect to the annealing time at 60 °C for a diode irradiated to a fluence of $1.4 \times 10^{13} \mathrm{n}_{eq}/\mathrm{cm}^2$. Adapted from [73].

5.3 Low Gain Avalanche Detectors (LGADs)

Solid state detectors have been developed since the beginning of semiconductor industry. The most common detectors with intrinsic charge multiplication are the **APDs!** (**APDs!**), proposed for the first time in the 1950s. An Avalanche Photodiode (APD) is a semiconductor device that use the photoelectric effect to generate an electric pulse after being illuminated by photons. It consists of a reverse biased

pn-junction with an intense electric field. The electrons which are generated can gain enough energy to initiate an avalanche mechanism. **APDs!** can be operated in linear or Geiger mode. In the first one, typical gain are of the order of 100 while in the latter case the gain is typical larger than 1000 and the electric pulse reaches saturation immediately. Their main application are imaging and single photon counting with **APDs!** operating in linear and Geiger mode respectively. These detectors are optimized to detect photons from infra-red to ultra-violet in a low light environment. In the case of a *mip*, this generates charge along its trajectory in the full detector thickness, therefore the amount of the primary charge is much larger than in the photon detection case, with about 75 electron-hole pairs per micrometer, as discussed in Section 5.2.

The LGAD technology has been initially developed by CNM Barcelona as a potential technology for radiation hard tracking detectors. The idea to have LGAD as tracking detectors was born from having charge multiplication already in unirradiated devices and profit to the signal enhancement due to the charge multiplication during detector lifetime in a harsh radiation environment, counterbalancing the signal degradation induced from radiation damage. For timing application, the use of detectors with an intrinsic gain enhance the slew rate which results in beneficial effects on the time resolution. Since the detector thickness also affect timing performance, thin LGAD devices for timing have been developed. The LGAD technology adapts the design of **APDs!** for the detection of *mips*. This technology target a gain of 10-20, much lower than the one targeted from **APDs!**. The charge multiplication is achieved with the introduction of an extra doped layer of acceptors ($p+$) material, usually Boron or Gallium, close to the *pn*-junction. The section of an LGAD sensor can be found in Figure 5.11. The resulting profile is characterized by a large increase in doping concentration in proximity of the junction, which creates a large electric field. In LGAD sensors, the electric field is divided in two zones: the drift volume, where low values of the electric field are present ($E \sim 30\,kV/cm$), and a thin multi-

plication zone with few micrometers depth where a very high electric field is present (E $\sim$ 300 kV/cm). In the n-on-p design, the multiplication process is started from the electrons drifting towards the $n{+}{+}$ electrode, making this design offering the best control over the multiplication process.

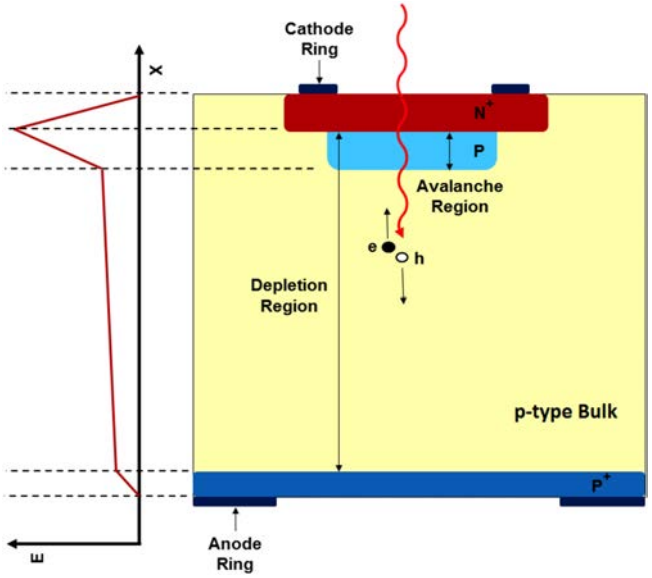

Figure 5.11

5.3.1 Why low gain?

Silicon detectors with high gain such as APDs or **SIPM!** (**SIPM!**) have capability to detects single or few photons respectively, and in order to perform such task they need a high gain. However, high gain level can bring drawbacks such as the increase of sensor noise, difficulties in sensor segmentation and high power consumption after irradiation. Detection of charged particles instead of photons had the advantage of a much larger initial signal, since a *mip* creates about 75 electron-hole pairs per micrometer, allowing the use of detector with low gain. LGAD technology is then the optimal solution for the problems induced by the high gain.

5.3.2 Why thin sensors?

The current which is generated by a *mip* particle into a LGAD sensor has a peculiar shape, depending only on the gain of the sensor. Assuming a fixed value of the gain, the signal steepness depends on the sensor thickness, favouring thin sensors for their faster rising edge (slew rate) which improves the time resolution. In Figure 5.12 the simulated current for a 50 µm-thick Ultra Fast Silicon Detector (UFSD) is shown. The initial electrons (red) drift toward the $n{+}{+}$ electrode, go through the gain layer and generate additional electron-hole pairs. The gain electrons (violet) are absorbed by the cathode and the gain holes (light blue) drift toward the anode and generate a large current. The gain increases the signal amplitude producing a slew rate following:

$$\frac{di_{Gain}}{dt} \sim \frac{dV}{dt} \propto \frac{G}{d} \tag{5.29}$$

Thus, the slew rate is proportional to the ratio of gain value over the sensor thickness. Therefore, thin detectors with high gain provide the best time resolution. Specifically, the maximum signal amplitude is controlled only by the gain value, while signal rise time depends only by the sensor thickness, as shown in Figure 5.13. Although,

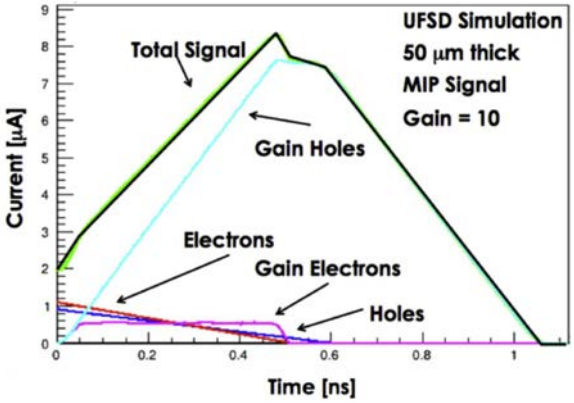

Figure 5.12: Simulated current signal for a 50 m-thick silicon detector. Figure taken from [74].

sensors have to be thin but not too much. An optimal value for sensor thickness has been found for $\sim$ 50 µm combined with a gain of $\sim$ 20 and a time resolution of 35 ps.

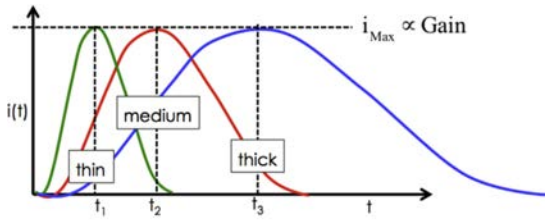

Figure 5.13: Current rise time for three different detector thicknesses with the same gain. Figure taken from [74].

5.3.3 Major effects on the time resolution

As anticipated previously in this document, three major effects determine the time resolution. Those are: time walk from amplitude variations, jitter from the electronic noise and Landau fluctuations originating from the non uniform charge deposition along the particle path. As explained in Chapter 3, time walk and jitter depend on the type of readout electronics, both depending on the inverse of the signal slope dV/dt. Jitter can be minimized chosing sensors with a high signal-to-noise ratio, while time walk using reconstruction algorithms such as CFD or TOT corrections. On the other side, the Landau contribution is due to the fact that a passing particle deposits its charge along the path inside the sensor in a non uniform way. This contribution depends on the thickness of the sensor, benefiting for thin sensors, and the setting of the threshold. As expected from equations 3.6 and 3.7 the resolution improves with the increase of the gain, which is proportional to the collected charge, due to the reduced noise jitter.

For the HGTD detector, LGAD sensors with an active thickness of 50 µm has been adopted as the best compromise between capacitance and deposited charge, which was favouring large thicknesses, and signal slope and Landau fluctuation, which were favouring a small one. Sensors with an active thickness of 30 µm have been also studied as an option for an improved time resolution but were discarded due to the higher capacitance, higher power dissipation and similar performances to the 50 µm-thick sensors after irradiation.

5.3.4 LGADs for the HGTD

At the present time, LGAD sensors have been produced by several manufacturing sites: Hamamatsu Photonics (HPK) Japan, CNM Spain, Fondazione Bruno Kessler (FBK) Italy, Micron UK, Brookaven National Laboratory (BNL) USA, National Nano Device Laboratory (NDL) and Institute of High Energy Physics (IHEP)-Institute of Microelectronics of the Chinese Academy of Sciences (IME) China.

As a dopant for the p-type multiplication layer, Boron is typically used. Additional Carbon implantation have been investigated for improved radiation hardness. As a substitute of Boron, Gallium has been studied as well. However, so far this has not demonstrated clear benefits, hence is not considered as a candidate for production.

In this document, several productions of CNM LGADs have been tensed and results on their performances will be presented in Chapter 6 for efficiency, charge collection and time resolution, both in beam test, laboratory and laser measurements. A brief introduction on the CNM production runs for which results will be presented in this thesis will be given in the next subsection.

5.3.5 CNM Production runs

In this section, a brief presentation of all the production runs for which results are shown in Chapter 6 will be given.

CNM Production Run 10478

The CNM LGAD production run 10478 from 2017 consisted of a total of five Boron-doped wafers, two of them, wafer 4 and wafer 5 for which results are shown in this document, are 100 mm Si-on-Si wafers with 50 µm-thick high resistivity wafer bonded to a 300 µm-thick support. Wafer 5 is a Carbon enriched wafer which has been produced in order to study possible advantages in terms of radiation hardness.

The wafer mask contains several single pad square diodes of 1 mm×1 mm, 1.3 mm×1.3 mm and 2 mm×2 mm, 2×2, 3×3 and 8×8 matrices of different pixels size and 2×1 arrays with different spacing. For wafer 4 sensors, an opening in the backside metallization was introduced in order to perform laser measurements, since the topside is metalized. From this production run, a selection of 1 mm×1 mm sensors has been used for measurements with radioactive source and, in case of wafer 4 sensors, also with laser.

CNM Production Run 10924

The CNM LGAD production run 10924 from 2017 consisted of seven Gallium-doped 50 µm-thick wafers with different implantation doses. A selection of 1 mm×1 mm single pad sensors has been measured with charged particles and laser.

CNM Production Run 12914

The CNM LGAD production run 12914 from 2020 consisted of a total of four Boron-doped wafers. These are Si-on-Si with 50 µm-thick high resistivity wafers with same implant dose. The wafer mask contains several single pad square diodes of 1 mm×1 mm, 1.3 mm×1.3 mm and, 2×2 and 5×5 matrices of different pixel size with different values of Inter Pad distance (IP distance). The different values for the IP distance are achieved modifying the width of the Junction Termination Extension (JTE), while the distance between them remains the same.

In this document, a set of 1.3 mm×1.3 mm single pad from this run has been measured with charged particles in laboratory to study charge collection and time resolution and a set of 2×2 arrays with 1.3 mm×1.3 mm pads has been measured with laser to study the behavior of the IP distance at different fluences.

CNM Production Run 13002

The CNM LGAD production run 13002 from 2021 consisted of four Boron-doped wafers with different implantation doses. These are 50 µm-thick wafers on 525 µm low resistivity epitaxial wafer substrate. The wafer mask contains only single pad sensors with pad sizes of 1.3 mm×1.3 mm and 3 mm×3 mm. In this document, a selection of single pad sensors with 1.3 mm×1.3 mm pads have been selected to be measured with charged particles and laser.

Chapter 6

Performance results for LGAD sensors before and after irradiation

Severals LGADs sensors have been studied during last years at IFAE and CNM laboratories. Different dopings and wafer technologies were analyzed in order to study their properties with respect to the increasing level of irradiation. In this chapter, results for different kind of measurements will be shown. At first, the different setups will be described. Section 6.9 is be dedicated to the description of CNM LGAD runs from 2017 with different doping materials. Measurements results with **MIP!**, using TCT ad from test beams will be presented. Section 6.3 describes a more recent CNM LGAD run from 2019 with higher dose than the previous one. A full electrical characterization and stability measurements are presented. Performance results will be shown for charge collection and time resolution for measurements with **MIP!**s. A set of 2×2 LGAD arrays will be characterized using the TCT to study the behavior of the distance between pads with respect to irradiation. At last, in section 6.4 results from LGAD sensors from low resistivity epitaxial layer from 2020 will be shown.

As before, a full electrical characterization ans stability measurements are presented. Measurements with **MIP!**s for charge collection and time resolution will be presented and compared with the Si-on-Si ones, such as a preliminary study on gain and time resolution made with TCT[1].

6.1 Setups

The aim of this section is to describe the different setups for the measurements for which results will be shown in this chapter. In order, setup for measurements with Sr-90 radioactive source, TCT setups for measurements with laser and test beam setups will be introduced.

6.1.1 Setup for measurements with ^{90}Sr β source

The LGAD response to **MIP!**s was studied using 2 MeV electrons from a Sr-90 radiation source, which is encapsulated in a plastic container and mounted on a 3D-printed support. Two LGADs sensors are mounted back to back on an aluminium L-shaped support frame and are aligned with respect to the source, mounted on a second support frame, as it is shown in Figure 6.1 on the right. The system is operated inside a climate chamber[2] at T=−30 °C. To avoid condensation on the sensor surface dry air is provided to the internal side of the climate chamber. The bias voltage to the sensor is supplied by a sourcemeter[3], while a low voltage supply[4] provides the 2.25 V needed for the signal first amplification stage (on the board), and the 12 V needed for an external second stage amplifier. Part of the experimental setup (oscilloscope, climate chamber and low voltage power supply) is shown in Figure 6.1 on the left. The output of the second stage amplifier is connected to an oscilloscope[5] which run

[1]These last measurements with TCT were performed by the CNM group.
[2]Votsch VT4002
[3]Keithley 2410 1100 V SourceMeter
[4]Rohde Swartz HMP4040 Programmable power supply 384 W
[5]Keysight DSO9404A

the acquisition software (see Appendix **??** for detailed information). LGADs sensors

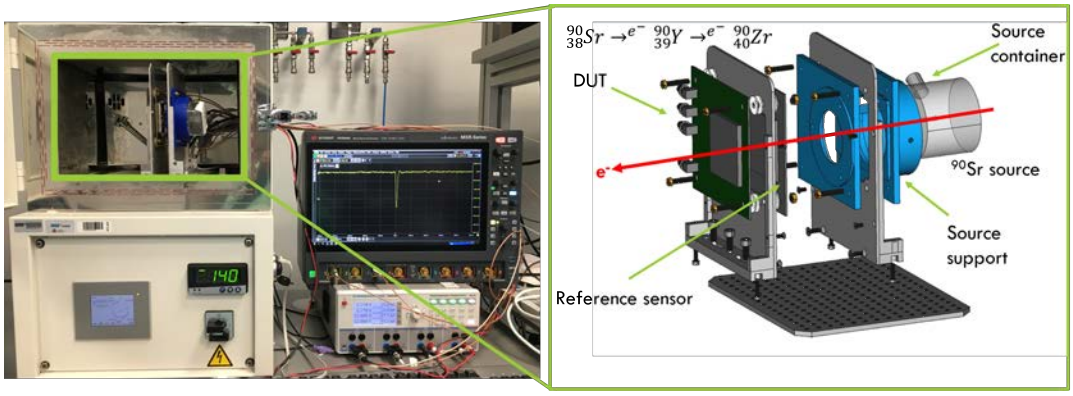

Figure 6.1: Setup for measurements with the Sr-90 source. On the left of the photo is possible to see the climate chamber, in which sensors are helded on a support (shown on the right) which allows to held also the radiactive source used for the measurements. Reference sensor and DUT are mounted back-to-back on a metal support. On the right side of the climate chamber, low voltage power supply and oscilloscope are visible. On the oscillosope screen a typical sensor signal is shown. Two high voltage power supply (not shown in the picture) are used to bias the sensors.

are assembled on 10 cm×10 cm read-out boards using a double-sided conductive tape, see Figure 6.2. These boards were developed at the University of California Santa Cruz (UCSC). The LGAD front-side metal pad layer was coupled to the input of an on-board transimpedance first-stage amplifier via multiple wirebonds to reduce the inductance, while the guard ring was grounded. For further amplification, an external second-stage amplifier with a gain of 10 and 2 GHz bandwidth is used.

Waveform data were analyzed using the LGADUtils framework [75] which has been developed at IFAE. At first, the oscilloscope binary data were converted into a ROOT ntuple containing the raw information for each DUT. The second step is the determination of the pulse polarity, the maximum and the minimum, the start and stop of the singal. As a third step noise and pedestal of the signal were computed in the range of the 10 to the 90% points before the start of the pulse. They were defined respectively as the mean and standard deviation of a Gaussian fit. As a consequence, the pedestal value was then subtracted from all the points of the waveform on an event-by-event basis. The last step was the computation of several waveform prop-

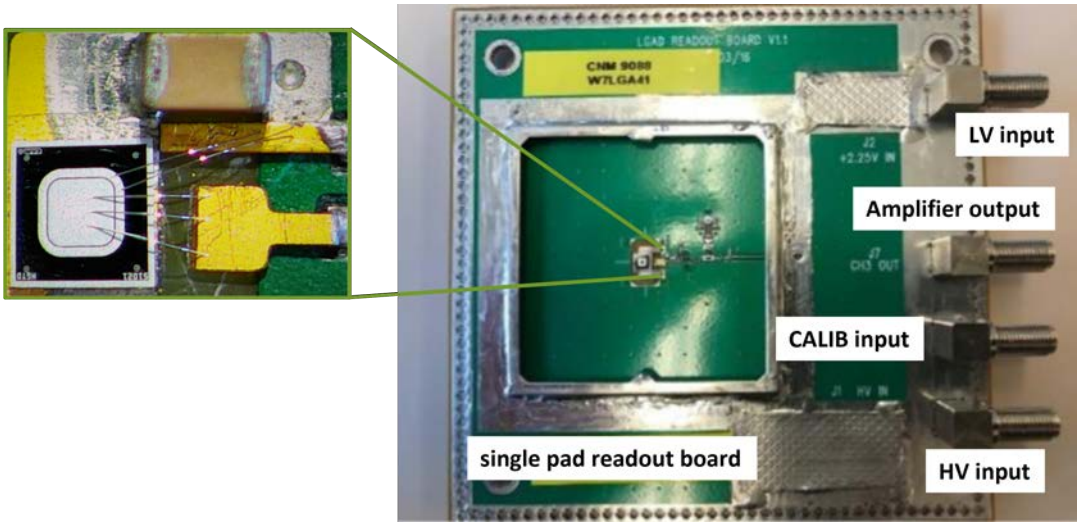

Figure 6.2: Picture of the single channel board with its connection used for measurements with radiactive source. On the left, a zoom on the sensor is shown: as it can be seen, the pad is connected to the readout line with three wire-bonds while the guard ring is grounded. Sensor is biased from the back (ohmic) side with negative voltage.

erties, such as the charge, the rise time, the jitter, the signal-to-noise ratio and the TOA at different thresholds. In the rest of this section, particular attention will be given to the computing of charge collection and time resolution which represents the core results of this document.

Collected charge calculation

For each event, the collected charge of the sensor is computed as the integral of the waveform signal around the peak. All those value fill a distribution of the collected charge for each bias voltage (BV) value. An example of this distribution is shown in Figure 6.3 for the unirradiated reference sensor used for these measurements. The distribution is fitted with an iterative fit procedure in order to find the optimal number of bins and fit interval using a Landau-Gauss convoluted function. The MPV value of the fit function is taken ans the collected charge value for the sensor at the given bias voltage and the σ of the fit function as its error.

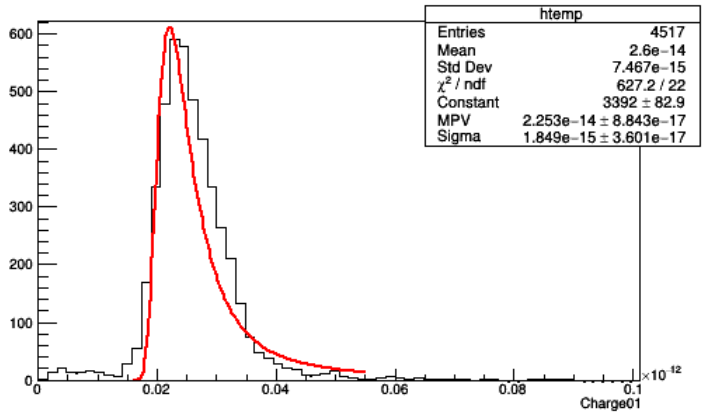

Figure 6.3: Collected charge distribution for the reference LGAD sensor at T=−30 °C. The distribution is fitted with a Landau X Gauss convoluted function and its MPV parameter is got as charge most probable value for the given bias voltage.

Time resolution calculation

Time resolution of LGAD sensors has been computed using a CFD method. The software analysis tool allow us to determine the TOA of the recorded waveforms for each event in a run, as the time crossing a given threshold. The set threshold corresponds to a certain fraction, here called f_{CFD}, of the signal maximum in steps of 0.05. The time resolution is calculated from the difference distribution of the TOAs of reference sensor and Device Under Test (DUT) for all the f_{CFD}, following the relation $t_{diff} = t(f_{CFD})_{Ref} - t(f_{CFD})_{DUT}$, as shown in Figure 6.4. The optimal fraction from the CFD method, for which signal is discriminated and the TOA has been determined, is defined by the dominant contribution to the time resolution. For unirradiated sensor, the dominant contribution is given by the Landau term while, for irradiated ones, jitter is the dominant effect. For each DUT, an optimization of the CFD fraction value has been carried out. On another hand, reference sensor has been calibrated separately in the past to determine its time resolution as a known parameter of this system. The calibration of the reference sensor used in these measurements and the determination of its time resolution is shown in ref. [76]. For the reference LGAD sensor used in this document, a time resolution of 35.7 ps has been determined for

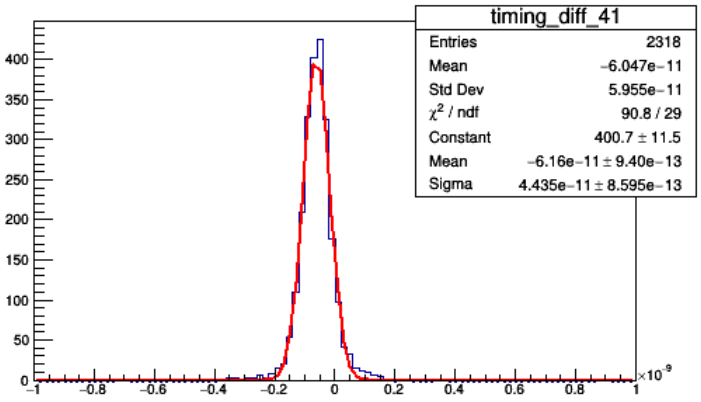

Figure 6.4: Time differences distribution between reference LGAD sensor and DUT at T=−30 °C for a given bias voltage and CFD percentage. The CFD percentage used for the reference sensor is 25%.

an optimal f_{CFD} =0.15 at T=−30 °C. The time resolution of LGAD DUTs has been determined using the performance of the reference device and the values listed below. The time difference between the TOA of the reference sensor for a f_{CFD} =0.15 and the TOA of the DUT at all the value of CFD fraction are computed and fitted with a Gaussian function, see Figure 6.4. The time resolution fo the DUT is obtained from the relation:

$$\sigma_i = \sqrt{\sigma^2_{DUT_{fCFD_i}} + \sigma^2_{refLGAD_{f_{CFD}=0.15}}} \tag{6.1}$$

where σ_i is the sigma of the Gaussian fit function of the distribution on Figure 6.4.

6.1.2 Transient Current Tecnique setup

The TCT [77, 78] consists of measuring of time-resolved current waveforms induced by the drift of charges inside a sensor. The current is proportional to the number of charges, to their drift velocity and to the weighting field of the readout electrode. Different detector properties can be determined by the analysis of recorded waveforms. The TCT allows to perform measurements with good position resolution ($\sim$ 10 µm). A pulsed laser source mimics the behavior of charged particles by illuminating the sensor with a large number of photons in a short time interval. An InfraRed (IR) laser

is used because its absorbtion lenght in silicon is of the order of mm, much larger than the detector thickness. In this way it can simulate the passing of a charged particle. Note, however, that the total charge deposited by the laser pulse is much larger than the charge corresponding to a **MIP!**. The TCT setup consists of:

- two laser sources, Red (660 nm) and Infrared (1064 nm)
- an optical system to focus the laser beam
- a current amplifier
- a waveform digitizer[1]
- a set of movable stages that allows to move the sensor on the perpendicular plane with respect to the laser beam and along the beam axis
- a Peltier element and controller to regulate operational temperature of the DUT
- a dry air filter to avoid condensation for measurements at low temperature

In Figure 6.5, a picture of the TCT setup with its components is shown. More detailed informations about the TCT setup available at the IFAE laboratory and its components can be found in appendix A.

6.1.3 Test beam setup

Test beam campaigns were conducted both at CERN **SPS!** (**SPS!**) H6A line using 120 GeV pion beam and at DESY TB 22 line using 5 GeV electron beam. The two setups are similar, with the only difference that at DESY only three DUTs could be tested in order to reduce the multiple scattering. A picture of the test beam setup at DESY TB22 is shown in Figure 6.6. A more detailed description of the setup and its components is given in [80]. Position dependent measurements were performed

[1] A DRS oscilloscope [79].

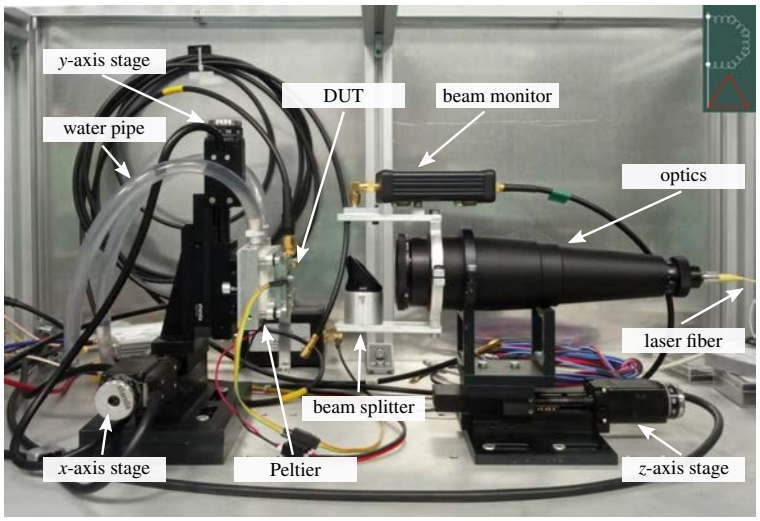

Figure 6.5: Transient Current Technique setup.

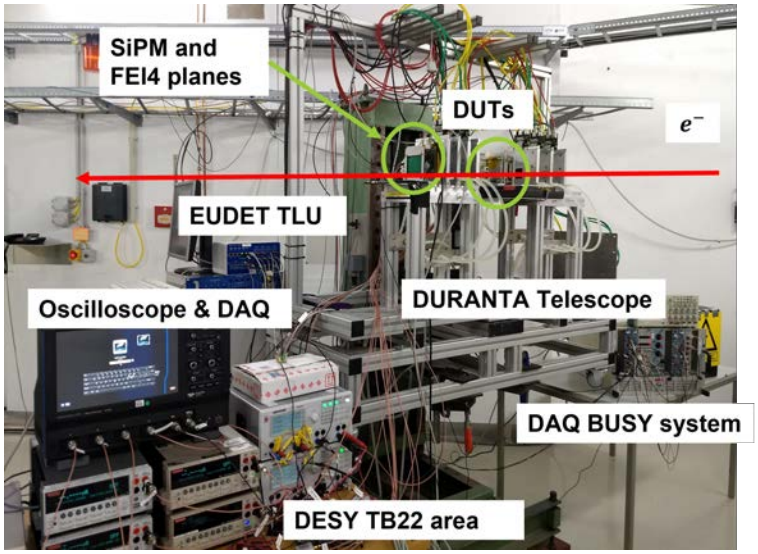

Figure 6.6: Picture of the beam test setup at DESY TB 22 area with its components. The direction of electron beam is shown by the red arrow. A detailed description of all the components can be found in reference [**?**].

using a EUDET-type telescope [81] consisting of two arms each of them made of three MIMOSA pixel plane of $10.6 \times 21.2\,\mathrm{mm}^2$, providing particle track information with a resolution of few micrometers. DUTs were placed in the space between the two arms of the telescope as shown in figure 6.6. The tracking information allows to reconstruct the trajectory of particles and to identify the specific position where DUT has been hit. Native data from the telescope containing the track information were reconstructed with the EUTelescope software [82] using the General Broken Line (GBL) algorithm to take into account the scappering of the 5 GeV electron beam. As for data from measurements with Sr-90 radioactive source, waveforms are analyzed with LGADUtils framework and ROOT ntuple provided by the conversion of oscilloscope data are merged with track information from the telescope.

6.2 Investigation of CNM LGAD production with Boron, Boron plus Carbon and Gallium doping material

In the past years, several doping materials have been explored by the CNM Barcelona for LGAD sensors. In the 2017, Boron[1], Boron plus Carbon[2] and Gallium[3] [83, 84]. Their charge collection and time resolution at cold temperatures have been studied for both neutron and proton irradiation. Results are presented in [76] and will be listed here briefly.

6.2.1 Electrical characterization and stability measurements

IV behavior of these sensors for different fluences has been studied at T=−30 °C on a probe station and it is shown in Figure 6.7. As shown also in [76], Gallium samples present a high leakage current with respect to the other ones due to the

[1]Production run 10478 W4
[2]Production run 10478 W5
[3]Production run 10924 W6

high charge multiplication. The sensors, once depleted, are close to the breakdown, having less room to operate with respect to Boron and Boron plus Carbon sensors. Gallium devices present also a high variation in the gain layer depletion voltage, see Fig. 2c in [76], explained by the fact that Gallium penetrates less than Boron in silicon because of the bigger atoms, and is diffused faster than boron during annealing process. The rate of self triggers is shown in Figure 6.8 as a function of the bias

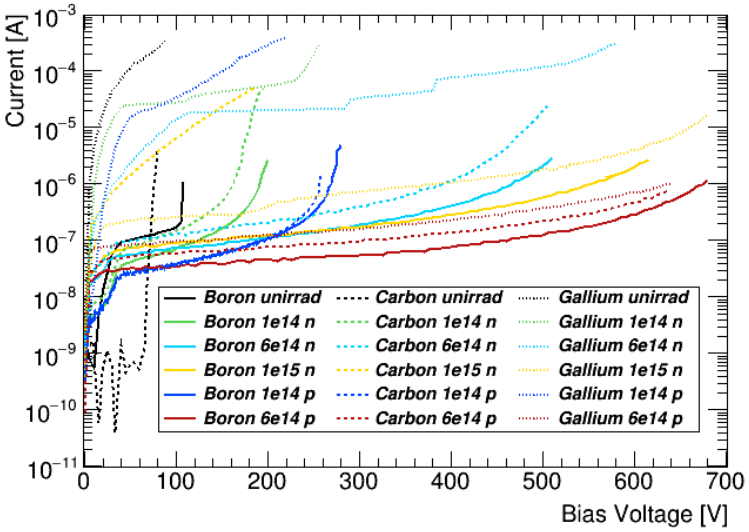

Figure 6.7: IV behavior measured on probe station at $-30°$ of Boron, Boron + Carbon and Gallium doped sensors.

voltage for different neutron and proton fluences. As shown, no self trigger is present for the unirradiated devices in their operational range and that Boron plus carbon devices start autotriggering before than boron ones, while gallium deviced even start autotriggering at higher voltages.

6.2.2 Measurements with ^{90}Sr β source

From data taking with source, collected charge and time resolution were studied as a function of the bias voltage, these results are shown in Figure 6.9 (a). Boron plus Carbon sensors have a larger charge collection that boron and gallium ones at the same bias voltage. In this Carbon enrichment looks like helping in the reduction of

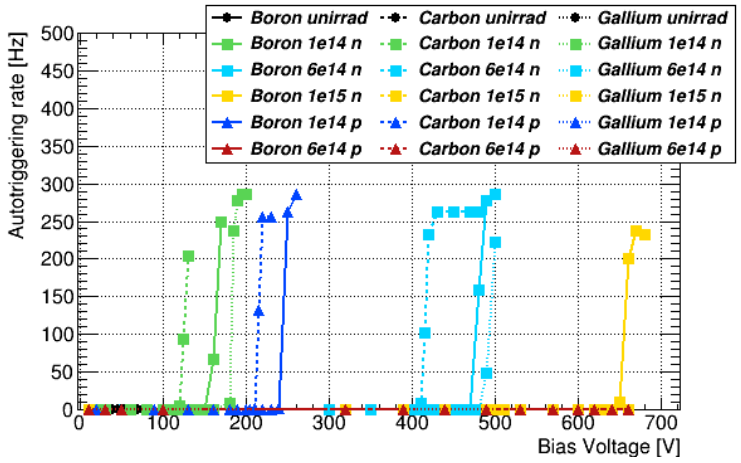

Figure 6.8: Rate of fake triggers on sensors doped with B, B+C or Ga.

the gain as a consequence of the irradiation. Time resolution results shown in Figure 6.9 (b), presents results better than 50 ps for both unirradiated and irradiated sensors. Boron and Boron plus Carbon sensors show similar performances, while gallium ones achieve higher value of time resolution due to the higher leakage current.

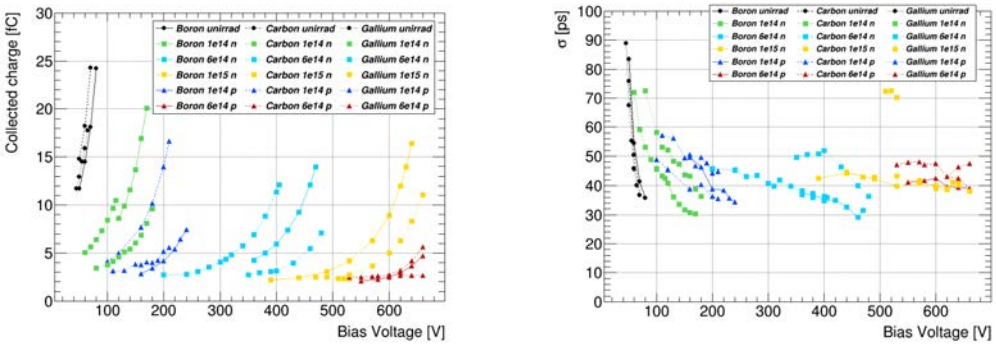

(a) (b)

Figure 6.9: Collected charge (left) and time resolution (right) before and after irradiation measured with beta source for sensor doped with Boron, Boron + Carbon and Gallium. All the measurements are taken at −30° in a dry environment.

6.2.3 TCT measurements for Boron and Gallium doped single pad LGAD sensors

In this section, gain measurements of the Boron doped sensors from CNM production run 10478 and Gallium doped sensors from production run 10924 will be presented.

Measurements setup

A sketch of the setup is shown in Figure 6.10 (a). The sensor is located in a metal box mounted on the x-y movable stage as shown in Figure 6.10 (b). In this setup, the DUT is biased from the topside while the backside (ohmic) is grounded. The pad and the guard ring of the sensor are wire-bonded to two different connectors and connected to the HV source (see Figure (b)). The connector on the left which is not cabled is not used for those measurements and does not present any connection with the sensor. In particular, the pad is biased through a Bias-T element which sends back the output signal of the sensor to the Cividec amplifier and then to the data acquisition (DAQ) system. The metal box presents a circular opening to allow the shooting of the laser beam on the back of the sensor surface, where is present the opening in the metal layer which allows this kind of measurements.

Measurements procedure

A selection of 50 µm thick Boron and Gallium doped 1 mm×1 mm LGAD sensor from production runs 10478 and 10924, have been used to study the gain as a function of bias voltage. The sensors used for the measurements are listed in Table 6.1. Sensors have been irradiated with neutron[1] and proton[2] up to fluences of $10^{15} \mathrm{n}_{eq} \mathrm{cm}^{-2}$. The unirradiated pin diode does not present any multiplication layer, consequently does

[1]Irradiation performed at JSI Lubjiana
[2]Irradiation performed at CERN PS

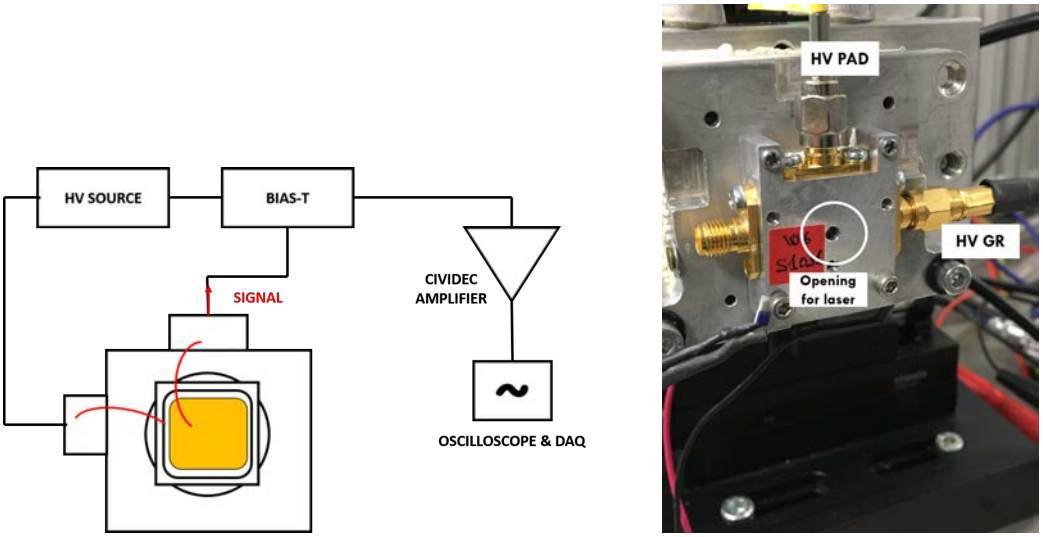

(a) (b)

Figure 6.10: Sketch of the setup used for measurements (a) and picture of the metal box in which the sensor is located, mounted on the x-y movable stage (b).

not have charge multiplication and gain, and it will be used for the calculation of the gain of the sensor for each bias voltage value.

Production Run	Sensor	Dopant	Fluence	Type	Size
10478	W4S1022	Boron	Unirradiated	-	1×1 mm^2
10478	W4S1067	Boron	1e14	proton	1×1 mm^2
10478	W4S1095	Boron	1e14	neutron	1×1 mm^2
10478	W4S1016	Boron	6e14	neutron	1×1 mm^2
10478	W4S1068	Boron	1e15	neutron	1×1 mm^2
10924	W6S1041	Gallium	Unirradiated	-	1×1 mm^2
10924	W6S1044	Gallium	1e14	proton	1×1 mm^2
10924	W6S1007	Gallium	1e14	neutron	1×1 mm^2
10924	W6S1012	Gallium	6e14	neutron	1×1 mm^2
10924	W6S1039P	-	Unirradiated Pin Diode	-	1×1 mm^2

Table 6.1: List of the sensors used for gain measurements.

TCT measurements were performed at $-20\,^{\circ}$C in a dry environment. The IR laser was shoot at the center of the back of the sensor to avoid possible edge effects, and the signal induced by the laser pulses was acquired. For each bias voltage value an average of 300 waveforms was collected. The laser pulse width was set at 60%[1] with

[1]The minimum pulse width for this system is 350 ps and the maximum is 4000 ps, where the minimum value corresponds to a pulse width of 100% and the smallest intensity.

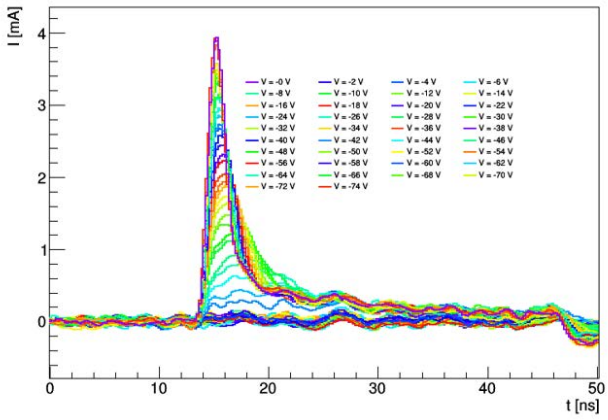

Figure 6.11: Example waveforms at different bias voltages for an unirradiated LGAD sensor.

a pulse frequency of 200 Hz [85]. An example for the recorded waveforms at different bias voltages for an unirradiated LGAD sensor is shown in Figure 6.11.

Gain results

The collected charge of each sensor is determined for each bias voltage from the integral of the waveform around the peak, in the range 12 ns to 24 ns (see Figure 6.11). For each bias voltage, the gain is calculated as:

$$G_i = \frac{Q_i}{< Q_{PIN} >} \tag{6.2}$$

where Q_i is the charge collected by the sensor at each bias voltage and $< Q_{PIN} >$ is the averaged collected charge of the pin diode. Gain results, presented also in [76], for the different LGADs are shown in Figure 6.12, where continuous lines correspond to Boron sensors and dashed lines correspond to Gallium ones. Boron LGADs show a higher gain at the same bias voltage with respect to Gallium doped ones. Moreover, proton irradiation presents a higher damage with respect to neutrons at the same fluence. Results for Gallium doped LGAD irradiated to $10^{15} \mathrm{n}_{eq}\mathrm{cm}^{-2}$ are not shown since the sensor died during the ramp up of HV because of a spike produced apparently

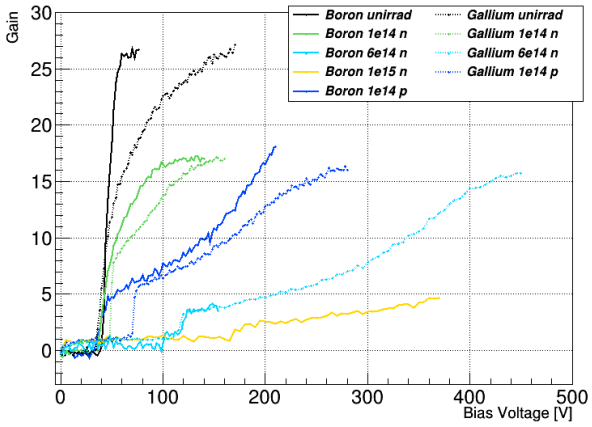

Figure 6.12: Gain behavior of Boron (continuous line) and Gallium (dashed line) doped sensors as function of bias voltage.

by the left humidity inside the box.

6.2.4 Performance in beam test

CNM LGAD sensors were tested in several beam test by the HGTD community, together with sensors from other vendors. The results presented in this document belong to the beam tests carried out during the year 2019 at DESY TB 22 with 5 GeV electrons. The setup is the one described in 6.1, with dry ice used for cooling down the temperature to $-30\,^{\circ}$C. Figure 6.13 shows the hit efficiency for the Gallium and Boron doped sensors at different values of required charges, together with the unirradiated reference sensor used for measurement (black line). The efficiency is computed in the central $0.5\times0.5\,\mathrm{mm}^2$ area of the sensor as the number of tracks associated to a waveform signal with a charge higher than the cut value divided by the total number of tracks associated to a waveform signal, considering only single track events:

$$\epsilon = \frac{n_{tracks(Q>Q_{cut})}}{n_{tracks}} \tag{6.3}$$

For the Boron doped sensors a low efficiency value has been found for both proton and neutron irradiation. This is given by the fact that the sensors died in the beam

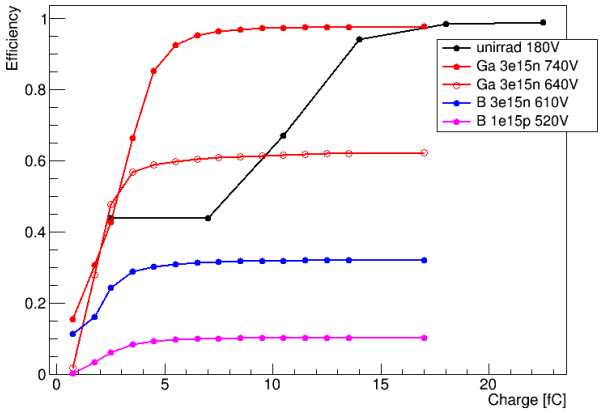

Figure 6.13: Hit efficiency as a function of the charge cut for a set of CNM LGAD sensors with different doping material.

test before having a bias voltage value high enough to get a reasonable value of the efficiency. Since the Ga 3e15n sensor presents a hit efficiency higher than 90% for a required Q >5 fC, in the rest of the section the property of this sensors will be investigated, such as charge collection and time resolution as a function of the bias voltage. In Figure 6.14 the hit efficiency of the Gallium doped sensor irradiated to 3×10^{15} n_{eq}/cm^2 is shown as a function of the bias voltage. For bias voltage higher than 680 V, efficiency is higher than 95%. As a function of the bias voltage,

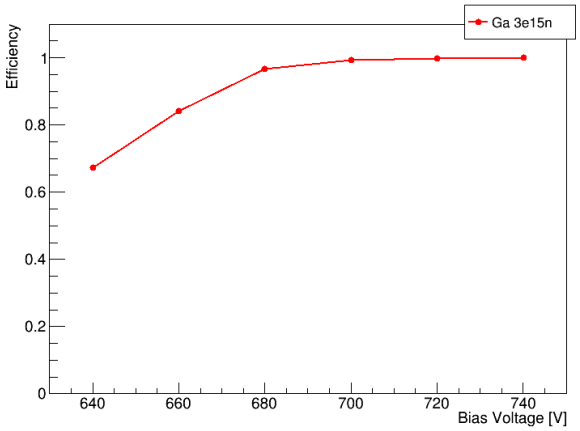

Figure 6.14: Hit Efficiency as a function of the bias voltage for the Gallium doped LGAD irradiated up to 3×10^{15} n_{eq}/cm^2.

charge collection and time resolution were studied. Results can be seen in Figure

6.15 (a) and (b). The sensor reaches the 4 fC requirement for an optimal ALTIROC performance, in particular it collects 5.3 fC at 740 V. The time resolution has been computed as explained in section 6.1 with CFD method. Since for irradiated sensor the dominant effect to the time resolution is the noise, a fraction at the 50% is used for this calculation. Time resolution was found to be 48.7 ps at 740 V, where the contribution for the reference sensor is already subtracted. This sensor meets then the HGTD timing requirements of 70 ps at the end of the HL-LHC. Figure 6.15 (c) shows the behavior of time resolution as a function of the collected charge For this

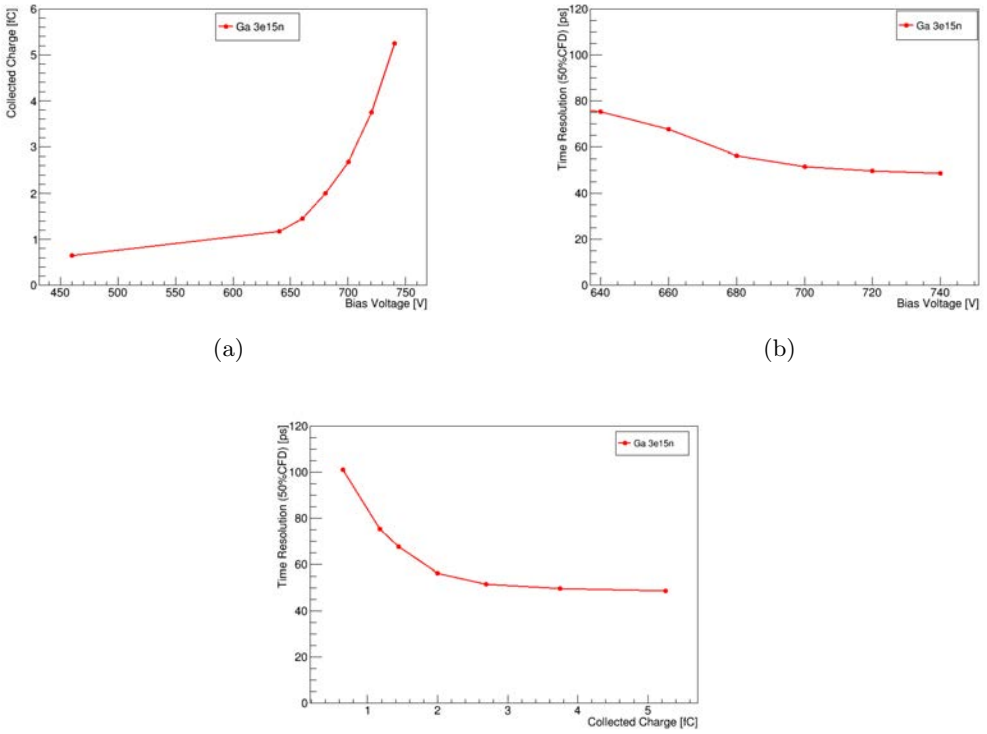

Figure 6.15: Charge collection and time resolution of the Gallium doped sensors irradiated to 3×10^{15} n_{eq}/cm^2. In top left figure (a) collected charge as a function of bias voltage is shown. Top right figure (b) shows time resolution as a function of the bias voltage while bottom figure (c) shows the time resolution as a function of the collected charge.

sensor, 2D efficiency maps were produced with different charge cuts. In Figure 6.16 the efficiency as a function of the reconstructed particle position is shown for a bias

voltage of 740 V. The efficiency is defined as in 6.3 as the ratio between the number of tracks associated to a signal with more than 2 fC collected charge (equivalent to a signal above 15 mV) and the total number of the reconstructed tracks extrapolated to the sensitive area of the sensor. A cut on 2 fC was used because this is the minimum required charge by the ALTIROC discriminator. In the central $0.5 \times 0.5\,\mathrm{mm}^2$ area, the average efficiency is 99,74% with 2 fC cut, see Figure 6.16 (a), whereas the edges are less efficient. Since for optimal ALTIROC performances 4 fC collected charge is required, a second map requiring tracks associated to signal with more than 4 fC collected charge has been produced, see Figure 6.16 (b). In this case, the average efficiency in the central $0.5 \times 0.5\,\mathrm{mm}^2$ area is 89.56%. The blurred edges in both Figures are determined by the movement of the box which contain the sensors due to the evaporation of the dry ice used for cooling.

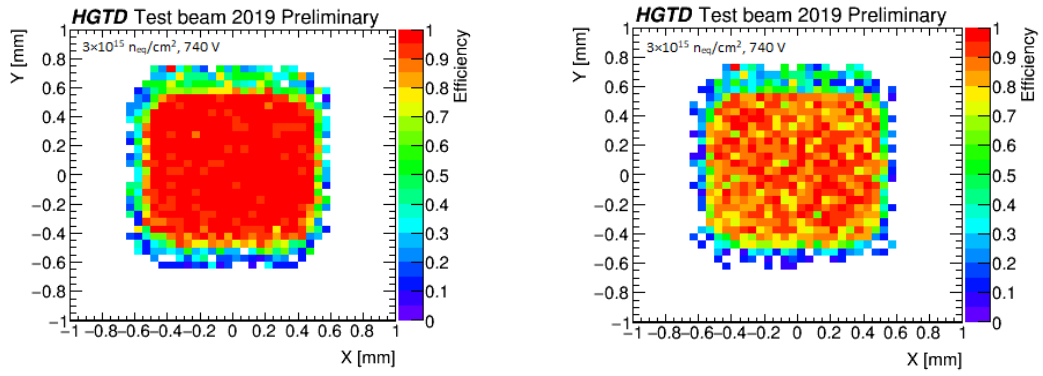

(a) (b)

Figure 6.16

6.2.5 Conclusions

As shown in laboratory measurements results with Sr-90 radioactive source, Boron and Boron plus Carbon devices perform similarly in terms of time resolution and charge collection before and after irradiation. Carbon infused devices collect more charge at the same bias voltage, diminishing the effect of gain reduction after irradi-

ation with respect to Boron ones. However, Boron plus carbon start auto-triggering earlier in voltage than other implants, which makes these devices not operable at high voltages. Thus, the determining factor for carbon is stability, and not radiation hardness. A full studied with more detailed information for those sensors can be found in reference [76]. However, in this first run with Carbon the implantation process was not optimal, and its benefits are not clear compared to later production with other manufacturers [86], see section **??**. From TCT measurements is clear that Boron doped devices present a higher gain respect to the Gallium doped ones at the same bias voltage. Moreover, proton irradiation results in a higher damage respect to the neutron one at same fluence. From beam test data taking, few results belonging to 2019 campaigns were presented in this chapter. A full study of both CNM and HPK LGAD sensors can be found in [**?**] where results from 2018 and 2019 campaign carried both at CERN and DESY are presented. Gallium sensor irradiated at $3\times10^{15}\mathrm{n}_{eq}/\mathrm{cm}^2$ meets the HGTD requirements in terms of charge collection, time resolution and hit efficiency, a full study on this sensor can be found also in [87]. However, the replacement of Boron by Gallium does not show clear benefits. Thus, considering also results from laboratory measurements, where Gallium devices present 20% less gain respect to the Boron ones, this line is not pursue. Several beam test campaign were carried out also during 2020 and 2021, being devoted to the study of LGAD sensors performances from several vendors and irratiated up to $2.5\times10^{15}\mathrm{n}_{eq}/\mathrm{cm}^2$ which is the radiation level expected at the end of the HL-LHC programme. Those beam test were also used to investigate the sensors mortality rates when exposed to high flux of particles. The analysis of those results is currently ongoing by the HGTD community.

6.3 Characterization of Si-on-Si wafer LGAD sensors from CNM run 12916

LGAD sensors for which measurements are shown in this section belong to CNM production run 12916, named AIDA2020v2, for which has been used a Si-on-Si wafer with a doping dose of 1.8×10^{13} atoms/cm^3. This dose is higher than the one for sensors discussed in the previous section 6.2. Sensors have been irradiated with neutron[1] up to fluences of 2.5×10^{15} n_{eq}/cm^2. In this section, results for Si-on-Si LGAD sensors irradiated with neutrons will be shown. At first, in section 6.3.1 the electrical characterization before and after irradiation (IV and CV curves) and stability measurements will be discussed. In section 6.3.2, results for charge collection and time resolution of data taking with Sr-90 radioactive source will be shown, to analyze if this technology fullfill the requirements for the HGTD detector, shown in Table 3.1. Lastly, in section **??** TCT measurements for 2×2 LGAD arrays to analyze the behavior of the Inter Pad distance as a function of the increased fluence and bias voltage will be shown.

6.3.1 IV, CV and Stability measurements

Electrical characterization before and after irradiation

Initially, devices have been electrically characterized before irradiation by the CNM group on a probe station at T=20 °C in a dry environment. The leakage current was studied as a function of the bias voltage, in order to determine the depletion and breakdown voltages. For IV measurements, sensors are biased from the topside with positive voltage and the backside of the sensors is grounded. Pad and guard ring are readout separately and total current is plotted. From CV measurements, ask albert to remind the connections. In Figure 6.17 are shown the IV (a) ad CV (b) behaviors

[1] Irradiation performed with 1 MeV neutrons in the TRIGA reactor in Ljubljana.

of those sensors before irradiation. For all the DUTs, the gain layer depletion is present at V_{gl} ~38 V, the fully depletion voltage at V_{fd} ~42 V and the breakdown voltage around V_{bd} ~85 V.

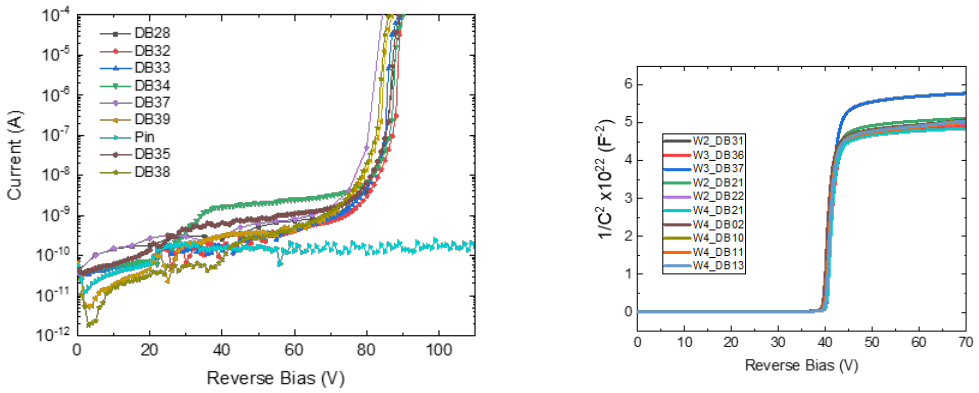

(a) (b)

Figure 6.17: IV (a) and CV (b) curves of the unirradiated Si-on-Si LGAD sensors from CNM production run 12916 at room temperature. As shown in the plots, for those sensors V_{gl} ~38 V, V_{fd} ~42 V and V_{bd} ~85 V.

After neutron irradiation, sensors have been characterized again from me on probe station at T=−30 °C in a dry environment. IV curves are shown in Figure 6.18, while the tested sensors and their fluences and breakdown voltages are listed in Table 6.2.

Production Run	Sensor	Dopant	Fluence	Type	Size	V_{bd}
12916	W1DB07	Boron	Unirradiated	neutron	1.3×1.3 mm^2	~50 V
12916	W1DB08	Boron	1e14	neutron	1.3×1.3 mm^2	~140 V
12916	W1DB05	Boron	6e14	neutron	1.3×1.3 mm^2	~500 V
12916	W1DB05	Boron	6e14	neutron	1.3×1.3 mm^2	~500 V
12916	W1DB06	Boron	1e15	neutron	1.3×1.3 mm^2	~640 V
12916	W1DB03	Boron	1e15	neutron	1.3×1.3 mm^2	~640 V
12916	W1DB33	Boron	2.5e15	neutron	1.3×1.3 mm^2	~720 V
12916	W1DB28	Boron	2.5e15	neutron	1.3×1.3 mm^2	~720 V

Table 6.2: List of sensors from CNM production run 12916 irradiated with neutron and studied with radioactive source.

As shown in the figure, breakdown voltage of irratiated sensor increased up to 700 V. The unirradiated sensor, which showed a V_{bd} ~85 V at room temperature, now breaks at V_{bd} ~50 V. The effect of this and its consequencies will be discussed further in next sections.

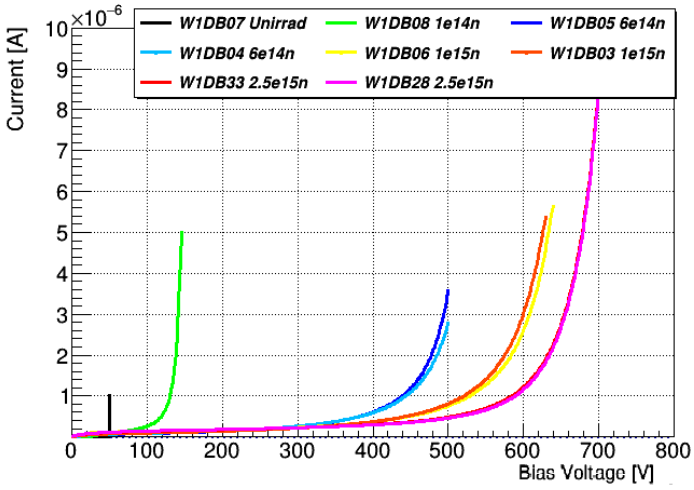

Figure 6.18: IV curves for unirradiated and irradiated SI-on-Si LGAD sensors from CNM production run 12916.

Gain layer depletion voltage as a function of irradiation level

The gain layer depletion voltage varies with respect to the fluence, due to the loss of dopant in Silicon. This has been studied as a function of the fluence to determine the C factor of the devices for this run. Lower is the number, better the sensor responds to irradiation and less will be the gain reduction. The V_{gl} value does not depend from the temperature, then for unirradiated devices the values from the CV measurements at room temperature shown in Figure 6.17 (b). For irradiated devices, there are non-idealistic conditions to study the CV behavior of the sensors. What can be done, is studying the $\frac{dI}{dV}$ as a function of the bias voltage. Around the V_{gl} voltage value, the $\frac{dI}{dV}$ curve will show a peak that can be fitted with a gaussian function, with mean value of the fit as the V_{gl} value for the sensor under test. The behavior of the V_{gl} values as a function of the fluence is shown in Figure 6.19. The distribution is fitted with an exponential function:

$$f(x) = e^{A+C \cdot V} \tag{6.4}$$

with V the voltage and A constant. The slope of the function is the so called acceptor removal factor $C = 7.26 \times 10^{-16}$.

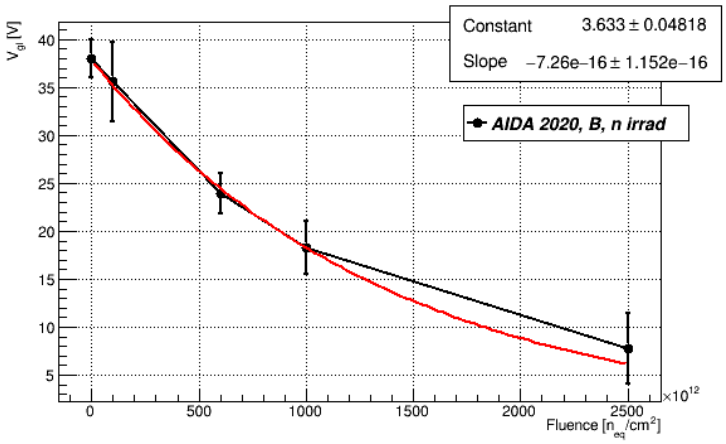

Figure 6.19: V_{gl} as a function of the fluence for the LGAD sensors from CNM production run 12916.

Stability measurements

Another important parameter to study before measuring LGAD sensors with radioactive source is the determination of the operating voltage points. This can be done throught some measurements which determine the rate of self triggers, so called autotriggering, of the sensors without a presence of an external source of particles. This effect is an intrinsec property of sensors with internal gain, which present spurious events for high enough bias voltages. The onset of autotriggering regime appears before the breakdown voltage and limits the operating voltage of the sensor. As the gain is reduced in the irradiated sensors, the operating point can be pushed closer to the breakdown value. For these measurements, a trigger selection on signals larger than 10 mV corresponding to $5\sigma_{noise}$ is applied, where the noise level is $\sim$2 mV for all the sensors, see Figure 6.20. Since the waveforms generated by autotriggering events are identical to real signal ones, is critical to measure this rate as a function of the bias voltage and operate the sensor below it. An acceptable operating voltage point is defined for autotriggering rate lower than 1 kHz. This limit comes from the average rate of data recorded in ATLAS. An excessive self-triggering would increase the dead time of the HGTD detector hindering its operation. The time between consecutive

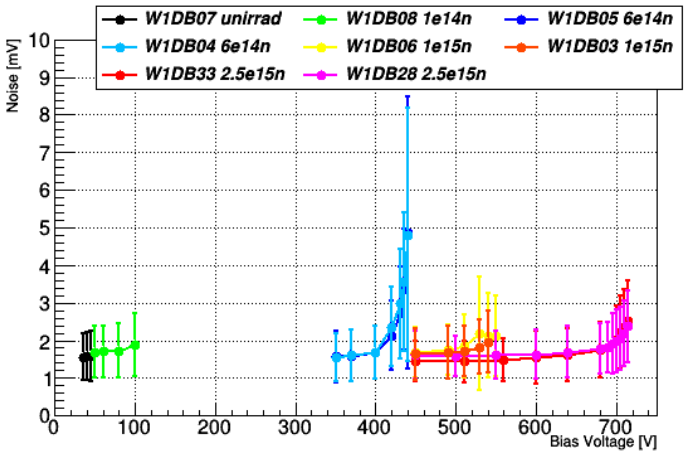

Figure 6.20

autotriggering events is studied with an oscilloscope[1] and DAQ system explained in Appendix **??**. The autotriggerng rate is defined as the inverse of this time difference. Refer to appendix for how the measurements is taken with the DAQ system. In Figure 6.21 the autotriggering of the set of sensors listed in Table 6.2 as a function of the bias voltage is shown. The unirradiated sensor presents a high autotriggering rate which severely limits the operational range of the device before irradiation, since as said, the full depletion is in the order of 42 V. This affects the sensor timing performance, as will be shown in the next section. However, after irradiation the gain is reduced and the operational range is extended.

6.3.2 Measurements with ^{90}Sr β source

The sensors listed in Table 6.2 were also characterized with Sr-90 radioactive source in the IFAE laboratory with the β-measurements setup explained in 6.1.

[1] put agilent name series num

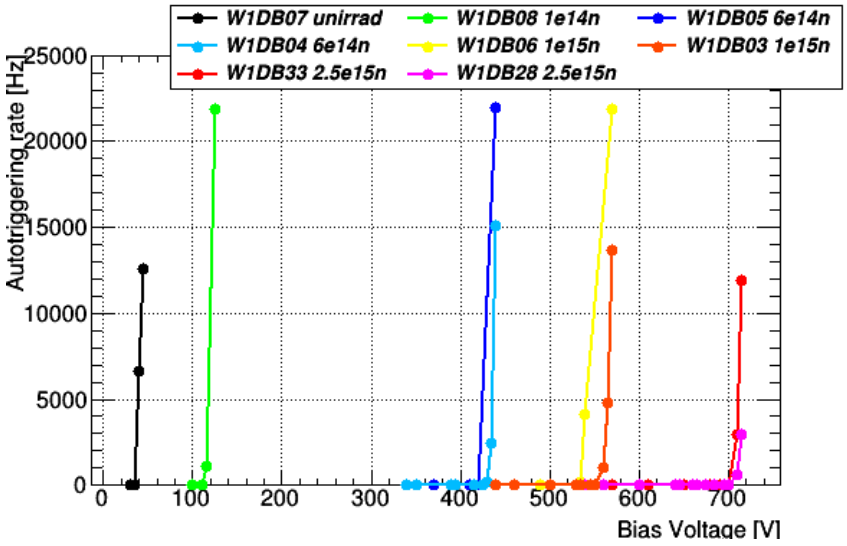

Figure 6.21

Collected charge

The collected charge as a function of the bias voltage is shown in Figure 6.22. Sensors irradiated to the highest fluence reach the target[1] of 4 fC for bias voltages higher than 680 V.

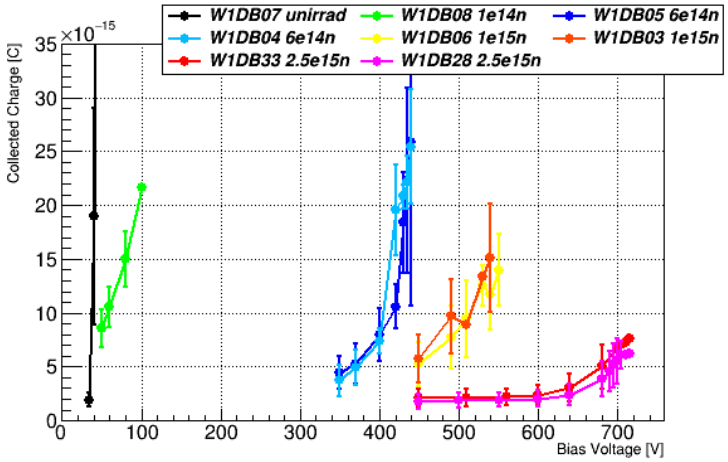

Figure 6.22: Collected charge as a function of bias voltage for unirradiated and irradiated SI-on-Si wafer LGAD sensors from CNM production run 12916.

[1]The 4 fC low limit is given by the HGTD sensor and electronics requirements.

Time resolution

For all the dataset, the time resolution on the unirradiated and irradiated sensors has been determined with this optimization method discussed at the beginning of this chapter. Time resolution as a function of the bias voltage is shown in Figure 6.23. All the irradiated sensors reach a time resolution below 40 ps up to the highest fluence

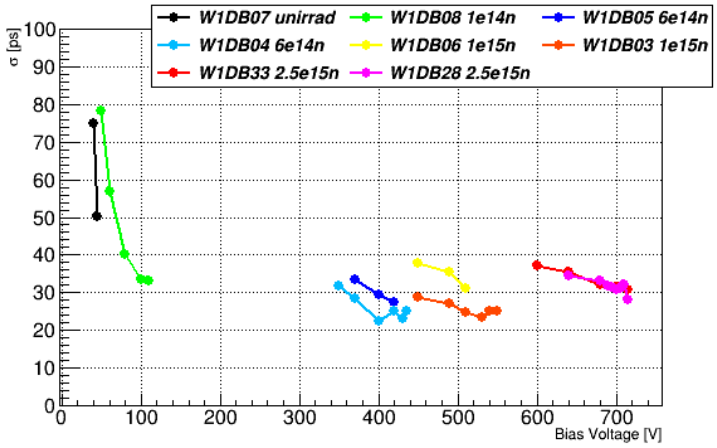

Figure 6.23: Time resolution as a function of bias voltage for unirradiated and irradiatel SI-on-Si LGAD sensors from CNM production run 12916.

value. Although, as discussed in section 6.3.1, the unirradiated sensor performances suffer from the small operational range between V_{fd} and V_{bd} values at cold temperatures, and from the consequent high rate of self triggers for those bias voltage values. Performances before irradiation for those Si-on-Si sensors are marginal due to this restricted operational voltage range. For comparison, the behavior of time resolution as a function of the collected charge for irradiated sensors is shown in Figure 6.24. From this plot it can be seen a minimum value of 4 fC for collected charge and a value lower than 40 ps for time resolution can be obtained for all the irradiated sensors up to 2.5×10^{15} n_{eq}/cm^2.

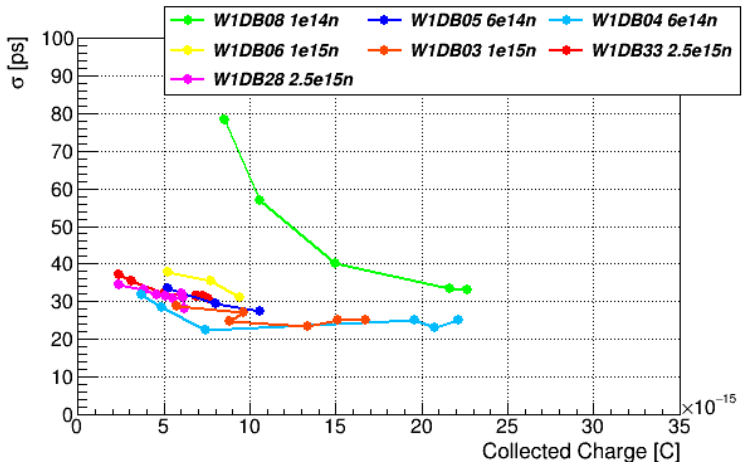

Figure 6.24: Time resolution as a function of the collected charge for unirradiated and irradiatel SI-on-Si LGAD sensors from CNM production run 12916.

6.3.3 Inter pad distance of 2 × 2 B doped LGAD arrays

In this section, measurements of the IP distance behavior as a function of fluence and bias voltage of a set of 2×2 LGAD arrays from production run 12916 will be presented.

Measurements setup

A sketch of the setup is shown in Figure 6.25 (a). As for the previous measurements shown in section 6.2.3, the sensor is located in a metal box mounted on the x-y movable stage. The backside of the sensor (ohmic) is grounded and the four pads and guard ring are biased from the topside with the same HV source. Two of the four pads, named PAD A and PAD B, are wire bonded two connectors C1 and C2, while the other two pads and the guard ring (GR) are connected to connector C3 and will not be read out by the oscilloscope. Pads A and B are biased through two Bias-T element which send the signal output to the Cividec amplifier and then to the DAQ system. The sensor is centered with respect to the opening in the metal box to allow the shooting of the laser in the central region between the two pads.

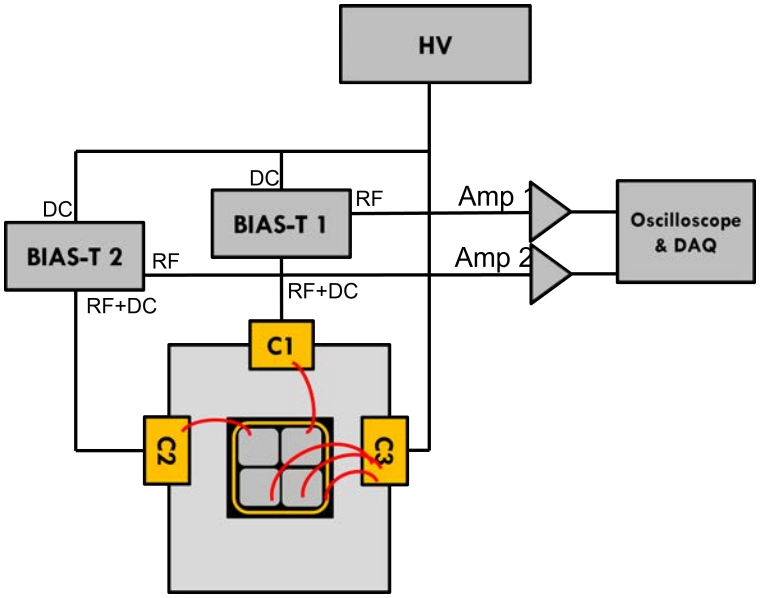

Figure 6.25: Sketch of the setup used for measurements with 2×2 arrays. The connections for pads and guard ring are shown in the picture.

Measurements procedure

Four 50 µm thick LGAD 2×2 arrays with 1.3 mm × 1.3 mm from CNM production run 12916 were selected to study the IP distance behavior as a function of bias voltage and fluence. Sensors are listed in Table 6.3. Those have been irradiated with neutron[1] up to fluences of 2.5×10^{15} n_{eq}/cm^2. At first, sensors have been electrically characterized

Production Run	Sensor	Dopant	Fluence	Type	Pad Size	Nominal IP
12916	W1A242	Boron	1e14	neutron	1.3×1.3 mm^2	57 µm
12916	W1A236	Boron	6e14	neutron	1.3×1.3 mm^2	57 µm
12916	W1A237	Boron	1e15	neutron	1.3×1.3 mm^2	57 µm
12916	W1A239	Boron	2.5e15	neutron	1.3×1.3 mm^2	57 µm

Table 6.3: List of the 2×2 LGAD arrays used for inter pad distance measurements.

on probe station at the CNM laboratory at T=−30 °C in a dry environment to identify the operating range for each sensor. IV curves are shown in Figure 6.26. For each sensor, the IV is done biasing the four pads and the guard ring from the topside of the sensor and its backside is grounded. One pad per time is read out during

[1]Irradiation performed with 1 MeV at TRIGA reactor in JSI Lubjiana

IV measurements. TCT measurements have been performed at −20 °C in a dry

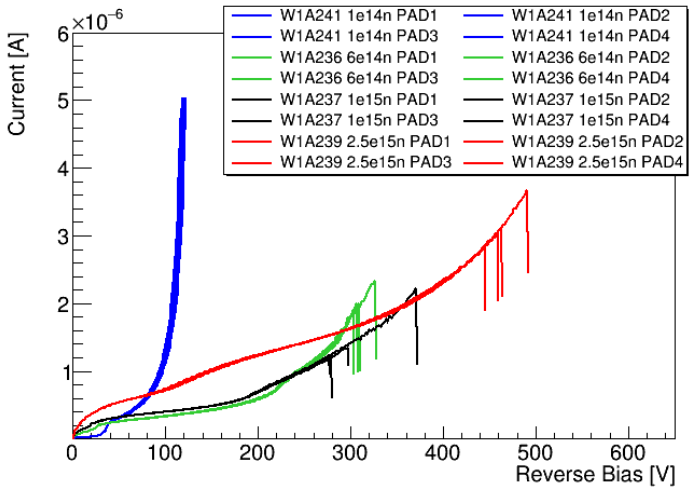

Figure 6.26: IV curves of 2×2 LGAD arrays at T=−20 °C on probe station in a dry environment.

environment. The IR laser was shoot on the backside of the sensor through the opening in the metal layer and an area of 0.5 mm×0.5 mm between pads A and B has been scanned with 50 µm steps in both x and y directions. In Figure 6.27, a sketch of the interested area for the x-y scanning is shown. An average of 1000 waveforms has been collected for each x-y position. The laser pulse was set at 60% with a pulse frequency of 200 Hz.

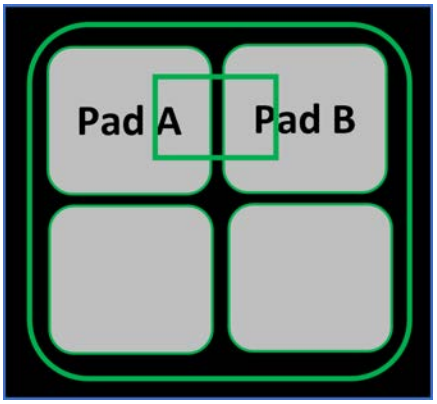

Figure 6.27: Sketch of the x-y scanned area for inter pad distance measurements.

Inter Pad distances results

As for the previous measurements, the collected charge is obtained integrating the waveform around the peak for each x-y position of the scan. From offline analysis a 2D map of the x-y scanned area is produced for each pad output, see Figure 6.28 for the PAD B output, with collected charge in color scale expressed in arbitrary units (AU). The negative value of charge shown in the region of PAD A is due to the discharching of the PAD B capacitor, as can be seen from the study in [88].

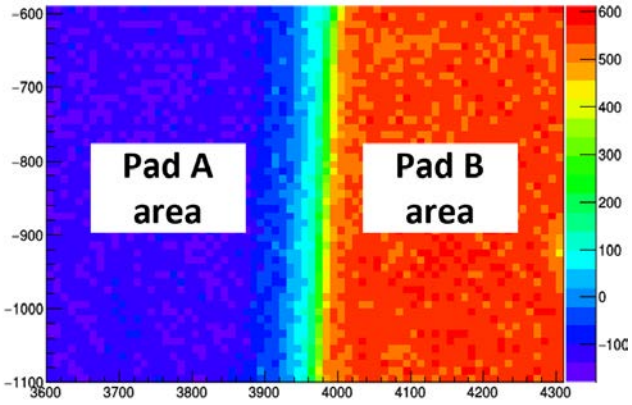

Figure 6.28: 2D map of the scanned X-Y area with IR laser only for PAD B output. On color scale, collected charge is considered in AU.

The projection of the 2D map for each of the pad is fitted with a (reverse) error function

$$f = p_3 + p_2 \cdot \frac{(1 \pm Erf(\frac{x-p_o}{p_1}))}{2} \tag{6.5}$$

with p_3 the baseline, p_2 the amplitude, p_1 the sigma and p_0 the x position at the 50% of the height of the fit function. An example of fit can be seen in Figure 6.29, where the projection of the two pads are plotted together with their fit functions and parameters. For each sensor and each bias voltage, the IP distance can be estimated as the difference of the p_0 fit parameters of the two pad, following the relation:

$$IP_{DISTANCE} = |p_{0(PADA)} - p_{0(PADB)}| \tag{6.6}$$

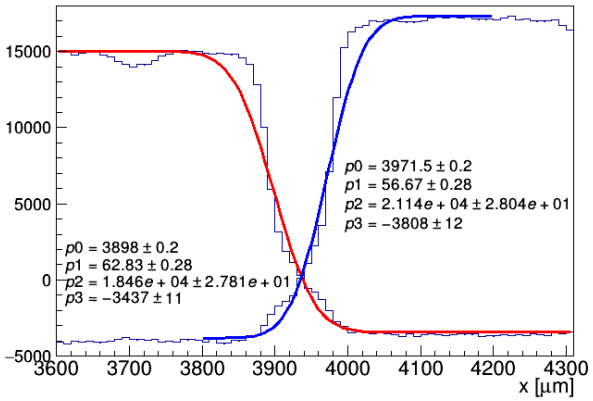

Figure 6.29: 2D map projection of the two pads with fit functions.

The nominal value of the IP distance before irradiation, that is the gap at the sensor design level, is 57 µm. The behavior of the IP distance is shown in Figure 6.30, for sensors irradiated from 10^{14} n_{eq}/cm^2 to 2.5×10^{15} n_{eq}/cm^2. Results from the unirradiated device are not reported since the early breakdown voltage of unirradiated sensors from this run did not allow to run the TCT measurements in stable conditions. From the Figure is possible to see two different behaviors. At low fluences (blue line), part of the carries generated underneath the gain layer drift to the JTE and don't produce charge multiplication. The effect, translated into an higer IP distance, is reduced as the bias voltage is increased. However, the effect of the JTE is reduced at higher fluences. At the same time, at higher fluences some multiplication is achieved by carries drifting to the JTE area and smaller inter-pad distances are measured at higher voltages (green, black and red lines). This behavior was also observed on LGADs from other vendors [89] and verified by simulations.

6.3.4 Conclusions and Outlook

Measurements with Si-on-Si single pad LGAD sensors with Sr-90 radioactive source show that the target charge of 4 fC and a time resolution lower than 40 ps can be achieved up to 2.5×10^{15} n_{eq}/cm^2 for BV higher than 680 V. Although, unirradiated devices show marginal timing performances due to the restricted operational voltage

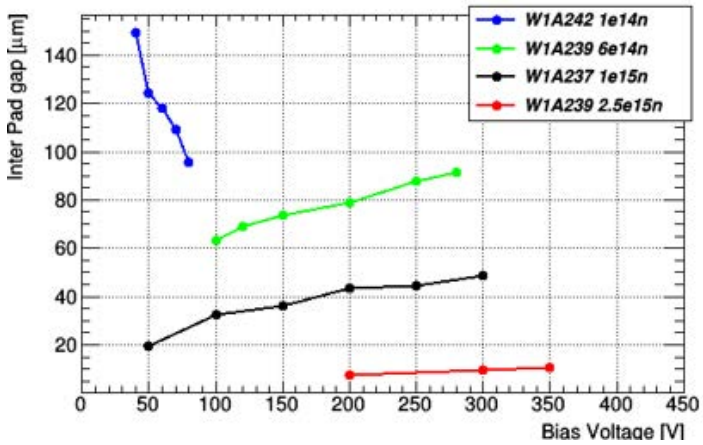

Figure 6.30: Inter pad distances as a function of bias voltage for Boron doped irradiated LGAD sensors.

range at cold temperature. For the 2 × 2 LGAD arrays the IP distance has been studies as a function of bias voltage up to 2.5 × 10^{15} n_{eq}/cm^2. As shown, the behavior differentiates between low and high fluences, for which the value of the IP distance tends to the nominal one. These results were verified through simulation. In order to study if LGAD performances before irradiation can be improved maintaing performances after irradiation, a set of sensor from low resistivity epitaxial wafer have been investigated. Results for these devices are shown in the next section.

6.4 Characterization of low resistivity epitaxial wafer LGAD sensors from CNM run 13002

6.4.1 IV, CV and stability measurements

Electrical characterization before and after irradiation

Devices have been electrically characterized before irradiation by the CNM group on a probe station at T=20 °C in a dry environment. Sensors are biased from the topside with positive voltage and the backside of the sensors is grounded. Sensors

which have been characterized before irradiation are listed in Table 6.4. Three wafers have been produced with different implantation dose, as listed. Two sensors for each wafer were characterized in order to study the V_{gl}, V_{fd} and V_{bd} voltages and IV and CV behaviors are shown in Figure 6.31 (a) and (b). For all the wafers V_{gl} ~30 V and V_{fd} ~35 V, while the V_{bd} varies from ~420 V for the highest dose wafer sensors (W4) to ~500 V for the lowest dose ones (W2).

Production Run	Sensor	Dopant	Dose	Size	V_{bd}
13002	W2N18-6	Boron	1.9×10^{13} at/cm^3	1.3×1.3 mm^2	~500 V
13002	W2N18-8	Boron	1.9×10^{13} at/cm^3	1.3×1.3 mm^2	~500 V
13002	W3N09-7	Boron	1.95×10^{13} at/cm^3	1.3×1.3 mm^2	~480 V
13002	W3N09-4	Boron	1.95×10^{13} at/cm^3	1.3×1.3 mm^2	~480 V
13002	W4N09-1	Boron	2.0×10^{13} at/cm^3	1.3×1.3 mm^2	~420 V
13002	W4N09-2	Boron	2.0×10^{13} at/cm^3	1.3×1.3 mm^2	~420 V

Table 6.4: List of sensors from CNM production run 13002 electrically characterized before irradiation.

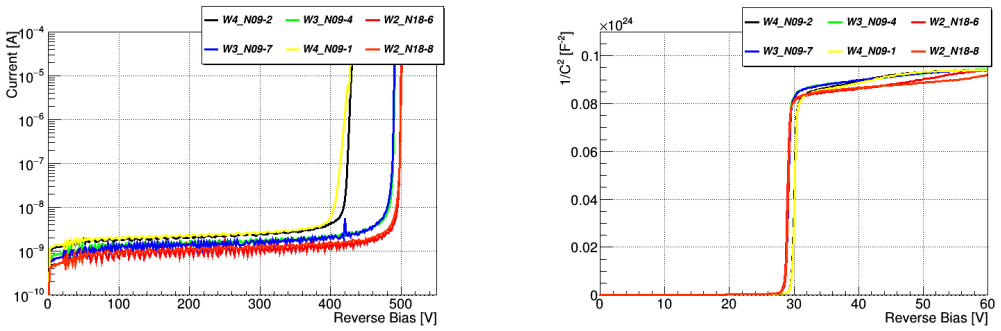

(a) (b)

Figure 6.31: IV (a) and CV (b) curves of the unirradiated low resistivity epitaxial wafer LGAD sensors from CNM production run 13002 at room temperature. As shown in the plots, for those sensors V_{gl} ~30 V, V_{fd} ~35 V and V_{bd} ~. keep log scale or linear of IV?

A set of sensors from W4 has been irradiated with neutrons[1] in order to study charge collection and time resolution with β source and compare results with Si-on-Si LGAD technology. Sensors from W4 are listed in 6.5 and IV curves before and after irradiation are shown in Figure 6.32.

[1]Irradiation performed with 1 MeV neutrons in the TRIGA reactor in Ljubljana.

Production Run	Sensor	Dopant	Fluence	Type	Size	V_{bd}
13002	W4N09-2	Boron	Unirradiated	neutron	$1.3\times1.3\,mm^2$	~420 V
13002	W4N09-4	Boron	1e14	neutron	$1.3\times1.3\,mm^2$	~500 V
13002	W4N18-1	Boron	5e14	neutron	$1.3\times1.3\,mm^2$	>700 V
13002	W4N18-2	Boron	8e14	neutron	$1.3\times1.3\,mm^2$	>700 V
13002	W4N09-3	Boron	1e15	neutron	$1.3\times1.3\,mm^2$	>700 V
13002	W4N18-3	Boron	2e15	neutron	$1.3\times1.3\,mm^2$	>700 V
13002	W4N09-6	Boron	5e15	neutron	$1.3\times1.3\,mm^2$	>700 V
13002	W4N09-5	Boron	1e16	neutron	$1.3\times1.3\,mm^2$	>700 V

Table 6.5: List of sensors from CNM production run 12916 irradiated with neutron and studied with radioactive source.

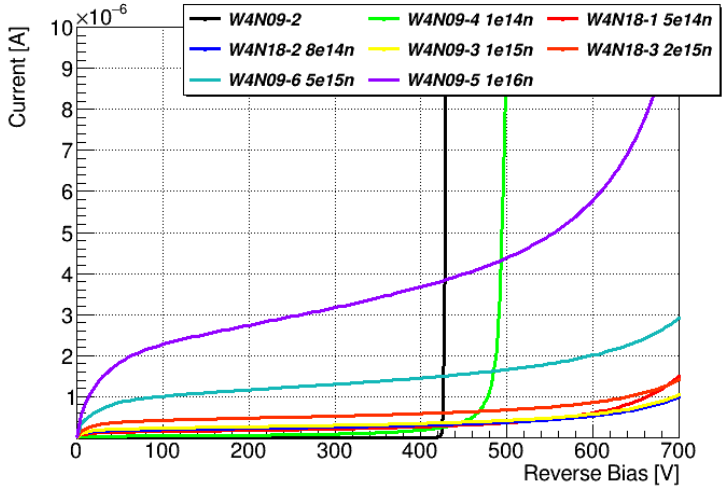

Figure 6.32: Caption

Gain layer depletion voltage as a function of irradiation level

As for the CNM production run 12916, also for sensors from production run 13002 the acceptor removal factor was extracted from the behavior of the V_{gl} as a function of the fluence. This is shown in Figure 6.33. As before, the V_{gl} value for the unirradiated sensor can be extracted from the CV measurements at room temperature, while the values for the irradiated sensors are extracted from the behavior of the $\frac{dI}{dV}$ as a function of the voltage. Note that for sensors irradiated at fluences higher than $10^{15}n_{eq}$/cm2 was not possible to identify the V_{gl} values, since no bump was visible in order to be fitted. This is compatible with what will be shown in charge collection

measurements with Sr-90 radioactive source in next section. The acceptor removal factor for LGAD sensors with low resistivity epitaxial wafer has been calculated as $C = 8.533 \times 10^{-16}$. This value is higher than the one calculated for Si-on-Si sensors. Indeed, it will be seen in next section that these sensors present less gain and collected charge then the one of the previous production.

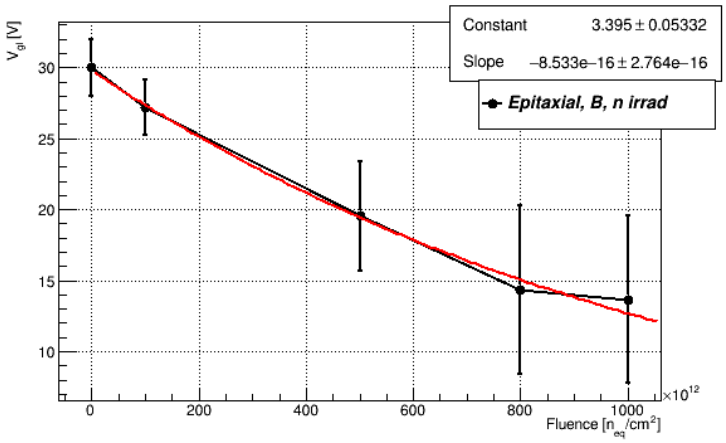

Figure 6.33: V_{gl} as a function of the fluence for the LGAD sensors from CNM production run 13002.

Stability measurements

Rate of self triggers was studied with no external source as a function of the bias voltage for the sensors shown in Table 6.5. Results for autotriggering measurements are shown in Figure 6.34, where a fake rate of triggers over 1 kHz is shown only for the unirradiated and the irradiated sensors to $10^{14} n_{eq}/cm^2$. For the higher irradiated sensors, no autotriggering was showing up. This can be related to the not high enough voltage value given by the high breakdown of these sensors. For safety, measurements were not carried at voltage values higher that 770 V. A threshold of 10 mV is used for the measurements. As can be seen in Figure 6.35, this is well above the noise of the sensors for all the bias voltages used for data taking.

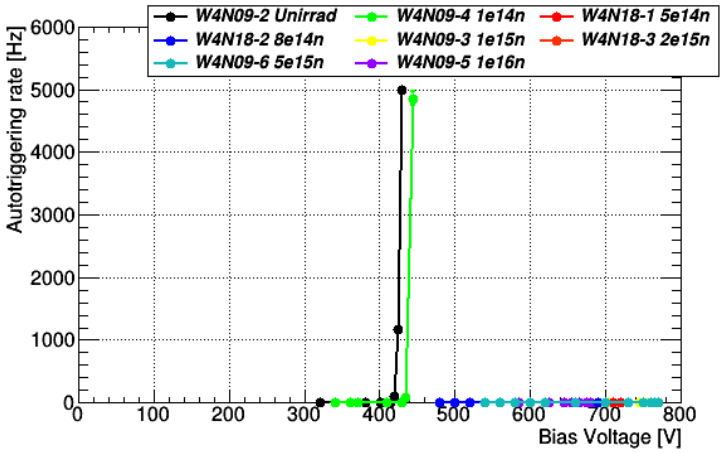

Figure 6.34: Rate of fake triggers as a function of the bias voltage.

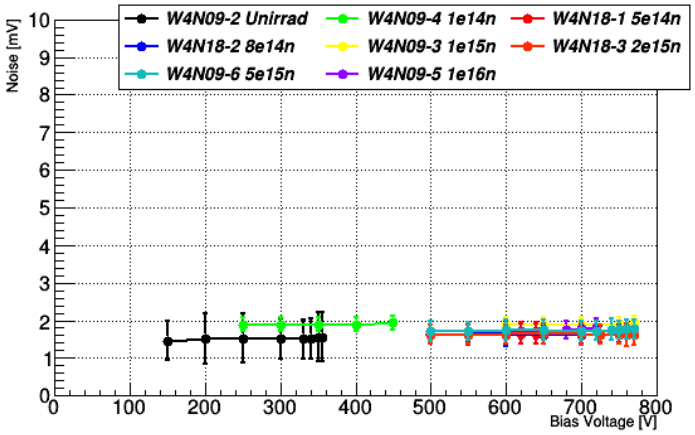

Figure 6.35: Noise of the sensors as a function of the bias voltage.

6.4.2 Characterization with ^{90}Sr β source

Collected charge

Collected charge for the sensors has been computed as explained at the beginning of this chapter. In Figure 6.36, it is shown as a function of the bias voltage for low resistivity epitaxial wafer LGAD sensors. The sensor irradiated at the highest fluence does not show any gain up to 720 V, but the high leakage current (see Figure 6.32) prevented safely reaching higher voltages. The sensor irradiated at $10^{15} \mathrm{n}_{eq}/\mathrm{cm}^2$ reaches a collected charge of 4 fC for bias voltages higher than 700 V.

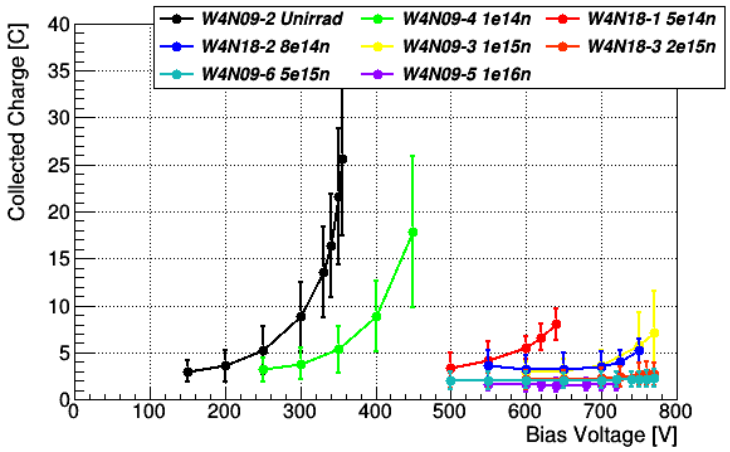

Figure 6.36: Collected charge as a function of the bias voltage for unirradiated and irradiated low resistivity epitaxial wafer LGAD sensors from CNM production run 13002.

Time resolution

Time resolution is computed as explained at the beginning of this chapter, keeping the same reference sensor for time resolution calculation. The optimal time resolution obtained with the CFD optimization algorithm is shown in Figure 6.37 as a function of the bias voltage. The time resolution of unirradiated and irradiated sensors feature values around 40 ps.

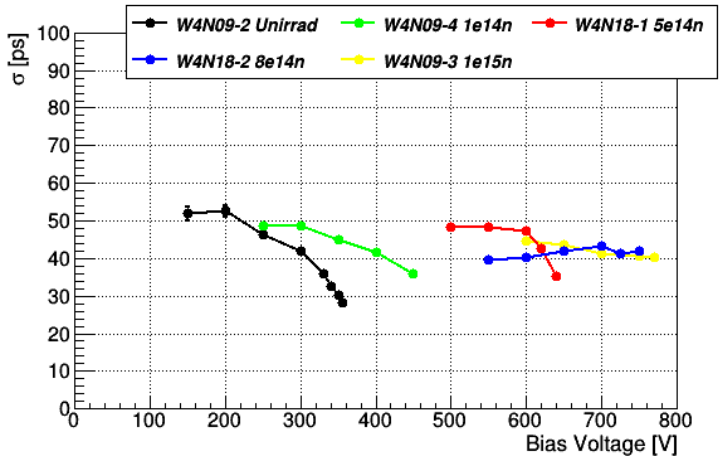

Figure 6.37: Time resolution as a function of the bias voltage for unirradiated and irradiated low resistivity epitaxial wafer LGAD sensors from CNM production run 13002.

6.4.3 Gain and time resolution measurements with TCT

TCT measurements on LGAD sensors from low resistivity epitaxial wafer were performed by the CNM group using IR laser beam. Measurements were performed at T=−20 °C for the sensor listed in Table 6.4. For time resolution measurements, the signal of the DUT is splitted and one of the two is delayed of 50 ns, in order to obtain the time resolution of the sensor from the time difference of a laser pulse and the same pulse which has been delayed, following the relation:

$$\sigma_{DUT} = \frac{\sigma_{tot}}{\sqrt{2}} \tag{6.7}$$

Results for gain and time resolution as a function of the bias voltage for different irradiated sensors are shown in Figure 6.38 and 6.39. Results obtained are consistent with the ones from Sr-90 data.

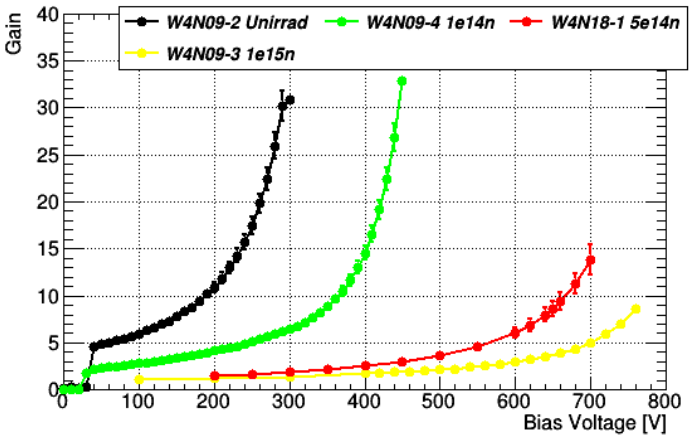

Figure 6.38: Gain as a function of the bias voltage for neutron irradiated LGAd sensors from CNM production run 13002.

6.4.4 Conclusions and comparison of results with Si-on-Si sensors

Measurements with low resistivity epitaxial wafer LGAD sensors with Sr-90 radioactive source show that the target collected charge of 4 fC can be achieved up to 10^{15}

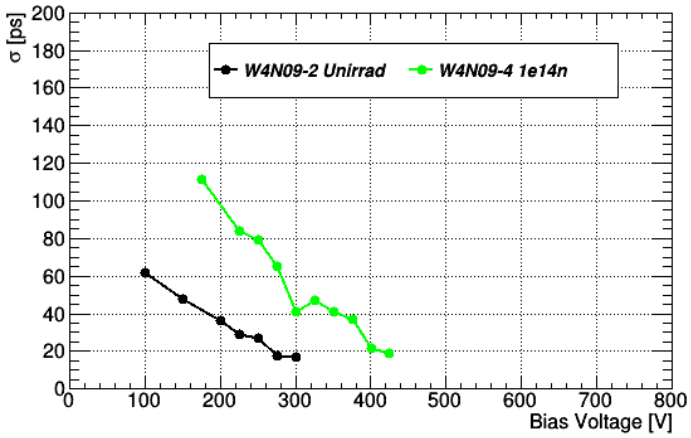

Figure 6.39: Time resolution as a function of the bias voltage for neutron irradiated LGAd sensors from CNM production run 13002.

n_{eq}/cm^2 at 750 V, and time resolution features values around 40 ps. TCT results for gain and time resolution show compatible value with Sr-90 data. Comparing these results with the one obtained for Si-on-Si LGAD sensors showed in Section 6.3, those ones show better performances at the same bias voltage and fluences. This can be explained by the difference of the wafer resistivity, since the low resistivity of 100 Ω cm of the epitaxial wafers requires a higher bias voltage to be operated. On the other hand, Si-on-Si devices show marginal performances before irradiation due to the restricted operational voltage range. Although, both productions present a high acceptor removal factor, which requires to push to very high voltages sensors after irradiation to hit the HGTD requirements. In the next section, a general overview of the other LGAD vendors will be given.

6.5 Outlooks

In this chapter results for several CNM LGAD production runs have been shown for different type of measurements. At first, CNM LGAD with Boron, Gallium and Boron plus Carbon doping have been shown for Sr-90 measurements, TCT measurements and test beams. From those results, it had been understood that the key factor of

Carbon enrichment in LGAD sensors is an improvement of stability of the sensors. Those sensors collect more charge respect to the Boron doped one at the same bias voltage, with a lower effect of gain reduction due to irradiation. Even though, sensor from this first production with Carbon started autotriggering before, not showing clear benefits respect to sensors from other manufacturers. Gallium research line has not been pursued since the replacement of Boron does not show clear benefits from results for testbeam, TCT and Sr-90 measurements.

Secondly, results from the AIDA2020v2 Boron doped Si-on-Si sensors are shown for laboratory measurements with Sr-90 radioactive source. Those sensors reach the target collected charge of 4 fC and time resolution of 40 ps for bias voltages higher than 680 V at a fluence of $2.5\times10^{15}\mathrm{n}_{eq}/\mathrm{cm}^2$, even if the early breakdown voltage at cold temperature makes the unirradiated device having marginal performances. In any case, the acceptor removal factor is relatively high and the gain loss with irradiation is not optimal compared to other sensors from other vendors (see IME).

At last, to check if any improvement before irradiation are visible, a set of sensors from low resistivity epitaxial wafer have been tested with Sr-90 source and TCT. Results obtained from the two type of measurements are compatible with each other, but their larger operational range respect to Si-on-Si LGADs does not show clear benefits. The target collected charge and time resolution can be reached only at 700 V for a fluence of $10^{15}\mathrm{n}_{eq}/\mathrm{cm}^2$, after which no more gain is visible. It was interesting to study epitaxial wafer behavior for their availability and lower cost with respect to the Si-on-Si ones, but the low resistivity of the wafers (100 cm) requires an higher voltage to be operated in order to maintain performances.

In the end, HGTD community have decided to continue in the Boron plus Carbon research line, since more clear benefits on performances after irradiation than the ones showed in this document are visible from LGAD sensors from other vendors.

Conclusions and Outlook

The HL-LHC presents a challenge to the ATLAS and CMS experiments due to the ... increase in radiation damage and pileup. ATLAS is upgrading its detectors to more radiation hard technologies to face the high luminosity era. The new tracker, the ITk, is expected to maintain, or improve, the performance of the detector despite the luminosity increase. But in the forward region the expected position resolution of the tracker is not enough to disentangle the pileup tracks from the ones originating in the primary vertex. Thus ATLAS will install the HGTD in the $2.4 < |\eta| < 4.0$ region that will provide track time resolution.

The HGTD is based on LGAD sensors. The first production of LGAD sensors at CNM was fully characterized in the context of this thesis.

The timing information provided by the HGTD will be used mainly to identify the pileup track (which originate at a different time window). This feature of HGTD will improve the overall physics performance of ATLAS. In this thesis the impact of the HGTD in the identification of the process $H \rightarrow \tau\tau$ was studied. The main background of this signal is $Z \rightarrow \tau\tau + jets$. Since a Monte Carlo sample of this signal is not available, the effect on the background suppression was studied comparing the impact of the "ITk only"scenario versus the pileup suppression using HGTD. The time information of a jet is obtained from the jet track timing and if the clustered time is sufficiently different ($\pm 1.5\sigma$ away) from the event t_0 (time of the hard scattered) then the jet is tagged as pileup. This process results in the removal of about 2.4

more pileup tracks than using the ITk information alone. Of course, it is important to know the detrimental effect which cut will have on the hard scattered tracks. For this, the Monte Carlo simulation of the signal is needed.

The core of this thesis is the study of the LGAD sensors produced at CNM. The LGAD technology was originally developed at CNM and later identified as a potential solution for timing in HEP. The LGAD sensors rely on a multiplication layer that provide low (~ 10) gain which in thus results in a enhanced timing performance. However, early on, one of the problem that was identifies was the fact that the multiplication layer would degrade after irradiation, (though the acceptor removal effects that affects the p-type multiplication layer). In order to maintain the multiplication layer after irradiation different doping materials were investigated. In this thesis, the first set of devices produced in 2017 at CNM on 100 mm ... wafers with different dopands and material in the multiplication layer (Boron, Boron + Carbon and Gallium) were fully investigated before and after irradiation with proton and neutron. Laboratory results with Sr90 source show that Boron and Boron + Carbon devices perform similarly in terms of charge collection and time resolution both before and after irradiation. At the same bias voltage, Carbon infused devices tend to collect more charge, diminishing the effect of the gain reduction after irradiation with respect to the Boron ones. However, they start to auto-triggering earlier in voltage and are not operable at high voltages.

TCT results show that Gallium devices collect less charge than Boron sensors at the same bias voltage, and that the proton irradiation results in a larger reduction of the multiplication layer compared to irradiation with neutrons. LGAD sensors with Gallium as the multiplication layer dopand were irradiated up to $3\times10^{15}\mathrm{n}_{eq}\mathrm{cm}¿^{2}$. Though the sensor could reach the target charge collected, very high voltage was needed (about 700 V). Furthermore the comparison between Gallium and Boron showed a 20% less gain in the former, which resulted in the Gallium devices not being investigated further. Results between TCT and measurements with Sr90 radioactive

source are in agreement.

However, the LGAD Boron-doped devices required a larger bias voltage to operate after irradiation.

In 2019 LGADs on Si-on-Si wafer with Boron in the multiplication layer were produced at CNM. In order to improve the performance with respect to the previous production, the multiplication layer doping was increased. This resulted in sensors with low breakdown voltage before irradiation, in which the timing performance was poor ($\sim$ 50 ps) because of the small V_{bd}. However, after irradiation the sensor did provide the target charge at 680 V. This voltage is, neverthless, too high to ensure good sensor operation due to the discharge through the bulk that destroy the device ("single event burnout").

TCT measurements were carried on the 2019 2×2 LGAD arrays in order to study the behavior of the inter-pad with respect to the fluences and bias voltages. A set of sensors irradiated from $10^{14} n_{eq} cm^2$ to $2.5 \times 10^{15} n_{eq} cm^2$ were measured with an IR laser and the behavior of the inter pad distance was studied. Results show two different behaviors. At low fluences, the IP distance part of the carries which are generated underneath the gain layer drift to the JTE and don't produce charge multiplication. The effect is translated into a larger IP distance, which is reduced with the increasing of the bias voltage. At high fluences the effect is the opposite: some multiplication is achieved by the carried drifting to the JTE are and smaller distances are measured. These results are compatible with ones from other vendors and verified by simulation.

The last production included in this thesis is from 2020. The LGADs were fabricated in 150 mm epitaxial wafer (which is less expensive than Si-on-Si). The sensors showed insignificant gain even before irradiation. The timing measurements using a Sr90 source showed that a time resolution of about 40 ps could be achieved at 750 V for devices irradiated up to $10^{15} n_{eq} cm^2$. This is far from the needed performances by HGTD.

In summary, though CNM is the original developer of the LGAD technology, the various CNM sensors included in this thesis fail to satisfy the HGTD requirements in terms of time resolution at moderate bias voltage to avoid irreversible damage in sensors after irradiation. While CNM was also the first site to produce B + C sensors then showed only marginal improvements compared to B-only devices. However, other fabrication sites (like FBK and IHEP-IME) produced LGADs with B + C that showed large improve results over the B only devices meaning they provided the charge required by HGTD at a moderate HV ($\sim$ 500 V). CNM recently provided another batch of LGAD sensors on 150 mm epitaxial wafer with B + C that are being tested.

Appendix A

Transient Current Technique

In the high energy physics community the characterization of sensors is usually carried out through radioactive source and test beams measurements. The first one, has the advantage that can be carried out in laboratory in a table-top set up, but the low energy radiation is emitted in a large angle, and even if it is collimated does not provide a good position resolution. The second one, has the advantage of providing a good position resolution for MIPs when combined with a pointing telescope for track reconstruction. Although, this kind of measurement can be performed for a limited time and in a limited number of facilities.

The TCT consists in the measurement of time-resolved current waveforms induced by the drift of charges inside a sensor. The current is proportional to the number of charges, their drift velocity and the weighting field of the readout electrode following the Shockley-Ramo theorem:

$$i(t) = q\,\overrightarrow{v}_{drift} \cdot \overrightarrow{E}_W \tag{A.1}$$

with q the moving charge, $\overrightarrow{v}_{drift}$ the free electrons drift velocity and $\overrightarrow{E}_W$ the weighting field of the readout electrode. By the analysis of waveform, different detector properties can be extracted. The TCT gives the opportunity to perform measure-

ments with good position resolution ($\leq$10 µm). The signal is generated by low energy photons which do not ionize along their path, in contrast to what happens with charged particles, but penetrate the sensors until they are eventually absorbed. The probability of photons to be absorbed is related to the detector material and photon wavelenght. To mimic the behaviour of charged particles the pulsed laser is used to illuminate the sensor with a large number of photons in a short time interval. The TCT setup available at the IFAE Pixel group laboratory is shown in Figure A.1.

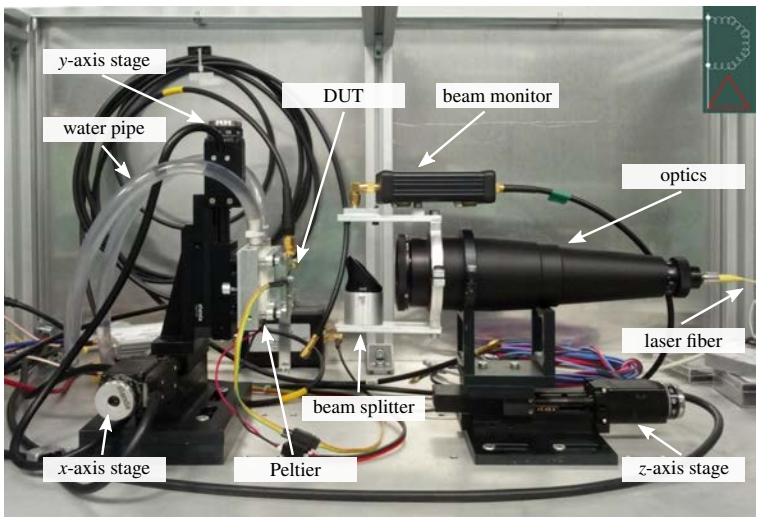

Figure A.1: Transient current technique set-up at IFAE.

The minimal TCT setup consists of a laser source, an optical system to focus the laser beam, a current amplifier and a waveform digitizer.

Laser Sources

Two different laser sources are available at IFAE. An IR source with a wavelength of 1064 nm and a red one with a wavelength of 660 nm. The absorption depth, that is the distance after which the number of photons is reduced by a factor $1/e$, in silicon is about 1 mm for the IR light and about 3 for red light.

The red laser creates electron hole pairs only on the proximity of the surface behaving as an α-particle that is immediately stopped. On the other hand, the IR

laser can be compared to a . Since the typical thickness of the silicon detectors used as DUT is between 50 and 300 , the intensity drop within the detector can be neglected, being the ionization uniform along the full thickness.

The duration and repetition rate of the laser pulses can be adjusted through a control software. The repetition rate is usually set to 500 Hz see figure **??**, while the duration is set to the minimum achievable value of 440 ps, see figure **??**. The laser intensity is set through a **DAC!** (**DAC!**) parameter called pulse width, see figure **??**. The intensity is larger when the pulse width is lower. At the start up this value is set to 2%, while for data acquisition should be larger than 60%. If the laser head is on and correctly connected to the DAQ PC the USB Status will display the word CONNECTED in green, while the On/Off symbol turns green when the laser output is enabled and red when it is disabled. The laser output can be enabled clicking the LASER ON/OFF button or setting the repetition rate. It is disabled automatically when changing from one tab to another of the LASER control software. If disabled through the LASER ON/OFF button the laser control software usually crashes. Be aware that the at the moment of powering on the laser it will automatically start firing pulses with a pulse width of 2%.

The source is coupled with an optical fiber that is plugged into an optical system providing a beam spot of 810 . The laser sources also provide an electric signal synchronous to the laser pulse to trigger the readout system usually connected to the fourth channel of the DRS4 evaluation board used as waveform digitizer.

The laser intensity has to be increased to the maximum, that means setting the pulse width **DAC!** to 0, to make the spot visible, as well as the repetition rate, to be set to 500 kHz. The red laser results visible if the spot is sufficiently focused on the target, for the IR laser a wavelength shifter card can be used to convert the IR to a visible frequency, shading of the area may be needed to be able to see the laser spot.

Amplifiers

Two pairs of broadband current amplifiers optimized for TCT measurements are available at IFAE. A pair of Particulars AM-02 amplifiers with a gain of 53 dB and a bandwidth of 2 GHz with a low band cutoff frequency of 10 kHz and a pair of CIVIDEC C2-TCT amplifiers operating in the same frequency band with a gain of 40 dB. The current input/output ratio can be obtained through the formula $G_{db} = 20 \log_{10} (I_{Out}/I_{In})$, resulting in an amplification factor of 100 for the CIVIDEC amplifiers and about 450 for the Particulars ones. Usually, the CIVIDEC amplifiers are preferred because of the lower noise.

Bias-T

The Bias-T element gives the possibility to connect an amplifier to the high voltage contact of the detector. It decouples the high voltage needed to bias the detector from the low voltage input of the amplifier. It is an essential part of any TCT system where both contacts, grounded and high voltage one, are read at the same time. Particulars Bias-T offers wide band width with almost no pulse distortion and can tolerate high voltages of up to 2 kV (depending on its version). Biasing detetors through Bias-T is many cases the only option, particularly when grounding or shielding of the detector requires chasis of the detector to be at ground potential.

Waveform Digitizer

After being amplified the signals are digitized to be stored in the DAQ PC. The digitizer used is a 4-channels DRS4 Evaluation Board with 700 MHz analog bandwidth, a sampling rate of 5 GSPS for a 200 ns sampling depth. The fourth channel is usually connected to the laser head output signal synchronous to the laser pulse that is used for triggering purpose.

Movable Stages

Three single axis Standa motorized translational stages allow to remotely control the DUT and the focus position. The focusing lens system is mounted on one of the stages, with the stage moving axis aligned with the laser beam direction in order to move forward or backward the focus position. The other two stages are mounted orthogonally to each other and to the beam axis. They hold the mounting plate that hosts the DUT and the Peltier element.

The stages have a position resolution better than 1 so that the pointing resolution of the TCT set-up is given by the laser spot focus size.

Data Acquisition System

Scanning TCT operations

Bibliography

[1] "Observation of a new particle in the search for the standard model higgs boson with the ATLAS detector at the LHC," *Physics Letters B*, vol. 716, pp. 1–29, sep 2012.

[2] "Observation of a new boson at a mass of 125 GeV with the CMS experiment at the LHC," *Physics Letters B*, vol. 716, pp. 30–61, sep 2012.

[3] J. Haffner, "The cern accelerator complex. complexe des accélérateurs du cern." `https://cds.cern.ch/record/1621894/?ln=it`.

[4] T. A. Collaboration, "The ATLAS experiment at the CERN large hadron collider," *Journal of Instrumentation*, vol. 3, pp. S08003–S08003, aug 2008.

[5] *CMS Physics: Technical Design Report Volume 1: Detector Performance and Software*. Technical design report. CMS, Geneva: CERN, 2006. There is an error on cover due to a technical problem for some items.

[6] *ALICE transition-radiation detector: Technical Design Report*. Technical design report. ALICE, Geneva: CERN, 2001.

[7] *LHCb reoptimized detector design and performance: Technical Design Report*. Technical design report. LHCb, Geneva: CERN, 2003.

[8] G. Apollinari, I. Béjar Alonso, O. Brüning, P. Fessia, M. Lamont, L. Rossi, and L. Tavian, *High-Luminosity Large Hadron Collider (HL-LHC): Technical Design Report V. 0.1*. CERN Yellow Reports: Monographs, Geneva: CERN, 2017.

[9] L. Rossi and O. Brüning, "High Luminosity Large Hadron Collider: A description for the European Strategy Preparatory Group," Tech. Rep. CERN-ATS-2012-236, CERN, Geneva, Aug 2012.

[10] K. Jakobs, "Physics at the lhc and slhc," *Nuclear Instruments and Methods in Physics Research Section A: Accelerators, Spectrometers, Detectors and Associated Equipment*, vol. 636, no. 1, Supplement, pp. S1–S7, 2011. 7th International ""Hiroshima"" Symposium on the Development and Application of Semiconductor Tracking Detectors.

[11] "High luminosity lhc project schedule." `https://hilumilhc.web.cern.ch/content/hl-lhc-project`.

[12] M. S. Alam *et al.*, "ATLAS pixel detector: Technical design report," 5 1998.

[13] A. Collaboration, "Atlas insertable b-layer technical design report," Tech. Rep. CERN-LHCC-2010-013 ; ATLAS-TDR-19, CERN, Geneva, Sep 2010.

[14] J. Jackson, "The atlas semiconductor tracker (sct)," *Nuclear Instruments and Methods in Physics Research Section A: Accelerators, Spectrometers, Detectors and Associated Equipment*, vol. 541, no. 1, pp. 89–95, 2005. Development and Application of Semiconductor Tracking Detectors.

[15] A. Vogel, "Atlas transition radiation tracker (trt): Straw tube gaseous detectors at high rates," *Nuclear Instruments and Methods in Physics Research Section A: Accelerators, Spectrometers, Detectors and Associated Equipment*, vol. 732, pp. 277–280, 2013. Vienna Conference on Instrumentation 2013.

[16] I. Perić, L. Blanquart, G. Comes, P. Denes, K. Einsweiler, P. Fischer, E. Mandelli, and G. J. Meddeler, "The fei3 readout chip for the atlas pixel detector," *Nuclear Instruments & Methods in Physics Research Section A-accelerators Spectrometers Detectors and Associated Equipment*, vol. 565, pp. 178–187, 2006.

[17] M. G.-S. et al., "The fe-i4 pixel readout integrated circuit," *Nuclear Instruments & Methods in Physics Research Section A-accelerators Spectrometers Detectors and Associated Equipment*, vol. 636, 2011.

[18] I. Gorelov, G. Gorfine, M. Hoeferkamp, S. Seidel, A. Ciocio, K. Einsweiler, M. Gilchriese, A. Joshi, S. Kleinfelder, R. Marchesini, O. Milgrome, N. Palaio, F. Pengg, J. Richardson, G. Zizka, M. Ackers, P. Fischer, M. Keil, S. Meuser, T. Stockmanns, J. Treis, N. Wermes, C. Gößling, F. Hügging, J. Wüstenfeld, R. Wunstorf, D. Barberis, R. Beccherle, M. Cervetto, G. Darbo, G. Gagliardi, C. Gemme, P. Morettini, P. Netchaeva, B. Osculati, F. Parodi, L. Rossi, K. Dao, D. Fasching, L. Blanquart, P. Breugnon, D. Calvet, J.-C. Clemens, P. Delpierre, G. Hallewell, D. Laugier, T. Mouthuy, A. Rozanov, C. Trouilleau, I. Valin, M. Aleppo, A. Andreazza, M. Caccia, T. Lari, C. Meroni, F. Ragusa, C. Troncon, G. Vegni, T. Rohe, G. Boyd, H. Severini, P. Skubic, J. Snow, P. Šıcho, L. Tomasek, V. Vrba, M. Holder, D. Lipka, M. Ziolkowski, D. Cauz, S. D'Auria, C. del Papa, H. Grassman, L. Santi, K. Becks, P. Gerlach, C. Grah, I. Gregor, T. Harenberg, and C. Linder, "A measurement of lorentz angle and spatial resolution of radiation hard silicon pixel sensors," *Nuclear Instruments and Methods in Physics Research Section A: Accelerators, Spectrometers, Detectors and Associated Equipment*, vol. 481, no. 1, pp. 204–221, 2002.

[19] M. C. Aleksa, W. P. Cleland, Y. T. Enari, M. V. Fincke-Keeler, L. C. Hervas, F. B. Lanni, S. O. Majewski, C. V. Marino, and I. L. Wingerter-Seez, "ATLAS Liquid Argon Calorimeter Phase-I Upgrade: Technical Design Report," tech. rep., Sep 2013. Final version presented to December 2013 LHCC.

[20] *ATLAS tile calorimeter: Technical Design Report.* Technical design report. ATLAS, Geneva: CERN, 1996.

[21] *ATLAS muon spectrometer: Technical Design Report.* Technical design report. ATLAS, Geneva: CERN, 1997.

[22] C. Ferretti and H. Kroha, "Upgrades of the atlas muon spectrometer with smdt chambers," *Nuclear Instruments and Methods in Physics Research Section A: Accelerators, Spectrometers, Detectors and Associated Equipment*, vol. 824, pp. 538–540, 2016. Frontier Detectors for Frontier Physics: Proceedings of the 13th Pisa Meeting on Advanced Detectors.

[23] *ATLAS magnet system: Technical Design Report, 1.* Technical design report. ATLAS, Geneva: CERN, 1997.

[24] A. Yamamoto, Y. Doi, Y. Makida, K. Tanaka, T. Haruyama, H. Yamaoka, T. Kondo, S. Mizumaki, S. Mine, K. Wada, S. Meguro, T. Sotoki, K. Kikuchi, and H. ten Kate, "Progress in atlas central solenoid magnet," *IEEE Transactions on Applied Superconductivity*, vol. 10, no. 1, pp. 353–356, 2000.

[25] L. Adamczyk, E. Banaś, A. Brandt, M. Bruschi, S. Grinstein, J. Lange, M. Rijssenbeek, P. Sicho, R. Staszewski, T. Sykora, M. Trzebiński, J. Chwastowski, and K. Korcyl, "Technical Design Report for the ATLAS Forward Proton Detector," tech. rep., May 2015.

[26] L. Adamczyk, E. Banaś, A. Brandt, M. Bruschi, S. Grinstein, J. Lange, M. Rijssenbeek, P. Sicho, R. Staszewski, T. Sykora, M. Trzebiński, J. Chwastowski, and K. Korcyl, "Technical Design Report for the ATLAS Forward Proton Detector," tech. rep., May 2015.

[27] C. Grieco, "ATLAS Forward Proton Detector," *PoS*, vol. LHCP2018, p. 031, 2018.

[28] "Technical Design Report for the Phase-II Upgrade of the ATLAS TDAQ System," tech. rep., CERN, Geneva, Sep 2017.

[29] V. Izzo, "ATLAS upgrades," *PoS*, vol. LHCP2020, p. 094, 2021.

[30] A. Collaboration, "Technical design report for the atlas inner tracker pixel detector," Tech. Rep. CERN-LHCC-2017-021, ATLAS-TDR-030, CERN, Geneva, Sep 2017.

[31] "Technical Design Report for the ATLAS Inner Tracker Strip Detector," tech. rep., CERN, Geneva, Apr 2017.

[32] "Technical Design Report for the Phase-II Upgrade of the ATLAS Muon Spectrometer," tech. rep., CERN, Geneva, Sep 2017.

[33] "Technical Design Report for the Phase-II Upgrade of the ATLAS TDAQ System," tech. rep., CERN, Geneva, Sep 2017.

[34] J. Lange, M. C. Areste, E. Cavallaro, F. Förster, S. Grinstein, I. L. Paz, M. Manna, G. Pellegrini, D. Quirion, S. Terzo, and et al., "3d silicon pixel detectors for the high-luminosity lhc," *Journal of Instrumentation*, vol. 11, p. C11024–C11024, Nov 2016.

[35] J. Lange, S. Grinstein, M. Manna, G. Pellegrini, D. Quirion, S. Terzo, and D. V. Furelos, "Radiation Hardness of Small-Pitch 3D Pixel Sensors up to HL-LHC Fluences," *Springer Proc. Phys.*, vol. 213, pp. 421–425, 2018.

[36] "Expected Performance of the ATLAS Inner Tracker at the High-Luminosity LHC," tech. rep., CERN, Geneva, Oct 2016. All figures including auxiliary figures are available at https://atlas.web.cern.ch/Atlas/GROUPS/PHYSICS/PUBNOTES/ATL-PHYS-PUB-2016-025.

[37] "Technical Design Report: A High-Granularity Timing Detector for the ATLAS Phase-II Upgrade," tech. rep., CERN, Geneva, Jun 2020.

[38] "Expected Performance of the ATLAS Inner Tracker at the High-Luminosity LHC," tech. rep., CERN, Geneva, Oct 2016. All figures including auxiliary figures are available at

https://atlas.web.cern.ch/Atlas/GROUPS/PHYSICS/PUBNOTES/ATL-PHYS-PUB-2016-025.

[39] G. Pellegrini, P. Fernández-Martínez, M. Baselga, C. Fleta, D. Flores, V. Greco, S. Hidalgo, I. Mandić, G. Kramberger, D. Quirion, and M. Ullan, "Technology developments and first measurements of low gain avalanche detectors (lgad) for high energy physics applications," *Nuclear Instruments and Methods in Physics Research Section A: Accelerators, Spectrometers, Detectors and Associated Equipment*, vol. 765, pp. 12–16, 2014. HSTD-9 2013 - Proceedings of the 9th International "Hiroshima" Symposium on Development and Application of Semiconductor Tracking Detectors.

[40] C. Agapopoulou, S. Blin, A. Blot, L. C. Garcia, M. Chmeissani, S. C. di Lorenzo, C. d. L. Taille, P. Dinaucourt, A. Fallou, J. G. Rodriguez, and et al., "Performance of a front end prototype asic for picosecond precision time measurements with lgad sensors," *Journal of Instrumentation*, vol. 15, p. P07007–P07007, Jul 2020.

[41] C. Allaire, J. Benitez, M. Bomben, G. Calderini, M. Carulla, E. Cavallaro, A. Falou, D. Flores, P. Freeman, Z. Galloway, E. Gkougkousis, H. Grabas, S. Grinstein, B. Gruey, S. Guindon, A. H. Correia, S. Hidalgo, A. Kastanas, C. Labitan, D. Lacour, J. Lange, F. Lanni, B. Lenzi, Z. Luce, N. Makovec, G. Marchiori, L. Masetti, A. Merlos, F. McKinney-Martinez, I. Nikolic-Audit, G. Pellegrini, R. Polifka, D. Quirion, A. Rummler, H.-W. Sadrozinski, A. Seiden, L. Serin, S. Simion, E. Spencer, S. Trincaz-Duvoid, M. Wilder, A. Zatserklyaniy, D. Zerwas, and Y. Zhao, "Beam test measurements of low gain avalanche detector single pads and arrays for the ATLAS high granularity timing detector," *Journal of Instrumentation*, vol. 13, pp. P06017–P06017, jun 2018.

[42] N. Cartiglia, A. Staiano, V. Sola, R. Arcidiacono, R. Cirio, F. Cenna, M. Ferrero, V. Monaco, R. Mulargia, M. Obertino, F. Ravera, R. Sacchi, A. Bellora,

S. Durando, M. Mandurrino, N. Minafra, V. Fadeyev, P. Freeman, Z. Galloway, E. Gkougkousis, H. Grabas, B. Gruey, C. Labitan, R. Losakul, Z. Luce, F. McKinney-Martinez, H.-W. Sadrozinski, A. Seiden, E. Spencer, M. Wilder, N. Woods, A. Zatserklyaniy, G. Pellegrini, S. Hidalgo, M. Carulla, D. Flores, A. Merlos, D. Quirion, V. Cindro, G. Kramberger, I. Mandić, M. Mikuž, and M. Zavrtanik, "Beam test results of a 16ps timing system based on ultra-fast silicon detectors," *Nuclear Instruments and Methods in Physics Research Section A: Accelerators, Spectrometers, Detectors and Associated Equipment*, vol. 850, pp. 83–88, 2017.

[43] M. e. a. Tanabashi, "Review of particle physics," *Phys. Rev. D*, vol. 98, p. 030001, Aug 2018.

[44] Y. e. a. Fukuda, "Measurement of the flux and zenith-angle distribution of upward throughgoing muons by super-kamiokande," *Phys. Rev. Lett.*, vol. 82, pp. 2644–2648, Mar 1999.

[45] Q. R. e. a. Ahmad, "Direct evidence for neutrino flavor transformation from neutral-current interactions in the sudbury neutrino observatory," *Phys. Rev. Lett.*, vol. 89, p. 011301, Jun 2002.

[46] K. e. a. Eguchi, "First results from kamland: Evidence for reactor antineutrino disappearance," *Phys. Rev. Lett.*, vol. 90, p. 021802, Jan 2003.

[47] S. Weinberg, "A model of leptons," *Phys. Rev. Lett.*, vol. 19, pp. 1264–1266, Nov 1967.

[48] A. Salam, "Weak and Electromagnetic Interactions," *Conf. Proc. C*, vol. 680519, pp. 367–377, 1968.

[49] N. Cabibbo, "Unitary symmetry and leptonic decays," *Phys. Rev. Lett.*, vol. 10, pp. 531–533, Jun 1963.

[50] F. Englert and R. Brout, "Broken symmetry and the mass of gauge vector mesons," *Phys. Rev. Lett.*, vol. 13, pp. 321–323, Aug 1964.

[51] P. W. Higgs, "Broken symmetries and the masses of gauge bosons," *Phys. Rev. Lett.*, vol. 13, pp. 508–509, Oct 1964.

[52] G. A. et al., "The ATLAS simulation infrastructure," *The European Physical Journal C*, vol. 70, pp. 823–874, sep 2010.

[53] S. A. et al., "Geant4—a simulation toolkit," *Nuclear Instruments and Methods in Physics Research Section A: Accelerators, Spectrometers, Detectors and Associated Equipment*, vol. 506, no. 3, pp. 250–303, 2003.

[54] S. Alioli, P. Nason, C. Oleari, and E. Re, "NLO vector-boson production matched with shower inttPOWHEG/tt," *Journal of High Energy Physics*, vol. 2008, pp. 060–060, jul 2008.

[55] S. Alioli, P. Nason, C. Oleari, and E. Re, "A general framework for implementing NLO calculations in shower monte carlo programs: the POWHEG BOX," *Journal of High Energy Physics*, vol. 2010, jun 2010.

[56] P. Nason and C. Oleari, "NLO higgs boson production via vector-boson fusion matched with shower in POWHEG," *Journal of High Energy Physics*, vol. 2010, feb 2010.

[57] T. Sjöstrand, S. Mrenna, and P. Skands, "PYTHIA 6.4 physics and manual," *Journal of High Energy Physics*, vol. 2006, pp. 026–026, may 2006.

[58] T. Sjöstrand, S. Mrenna, and P. Skands, "A brief introduction to PYTHIA 8.1," *Computer Physics Communications*, vol. 178, pp. 852–867, jun 2008.

[59] A. e. a. Andreazza, "Measurement of the $H \to \tau^+\tau^-$ cross-section in 13 TeV Collisions with the ATLAS Detector," tech. rep., CERN, Geneva, Apr 2017.

[60] M. Testa, "Tagging and suppression of pile-up jets in the forward region using timing information with the ATLAS detector at s = 14 TeV at HL-LHC," tech. rep., CERN, Geneva, Jan 2022.

[61] C. Grupen and B. Shwartz, *Particle Detectors*. Cambridge Monographs on Particle Physics, Nuclear Physics and Cosmology, Cambridge University Press, 2 ed., 2008.

[62] C. Canali, C. Jacoboni, F. Nava, G. Ottaviani, and A. Alberigi-Quaranta, "Electron drift velocity in silicon," *Phys. Rev. B*, vol. 12, pp. 2265–2284, Sep 1975.

[63] F. Frster, "Novel silicon detector technologies for the HL-LHC ATLAS upgrade." `https://cds.cern.ch/record/2730681`.

[64] G. Ottaviani, L. Reggiani, C. Canali, F. Nava, and A. Alberigi-Quaranta, "Hole drift velocity in silicon," *Phys. Rev. B*, vol. 12, pp. 3318–3329, Oct 1975.

[65] I. Lopez Paz, "The one-armed ATLAS Forward Proton detector," Mar 2018. Presented 22 May 2018.

[66] C. Patrignani *et al.*, "Review of Particle Physics," *Chin. Phys. C*, vol. 40, no. 10, p. 100001, 2016.

[67] N. Wermes, L. Rossi, P. Fischer, and T. Rohe, *Pixel Detectors, From Fundamentals to Applications*. Springer-Verlag, 2006.

[68] W. Riegler and G. A. Rinella, "Time resolution of silicon pixel sensors," *Journal of Instrumentation*, vol. 12, pp. P11017–P11017, nov 2017.

[69] A. Vasilescu, "The NIEL scaling hypothesis applied to neutron spectra of irradiation facilities in the ATLAS and CMS STC.," 1999.

[70] L. G. Vasilescu, A., "Displacement damage in silicon."

[71] G. Lindström, M. Moll, and E. Fretwurst, "Radiation hardness of silicon detectors – a challenge from high-energy physics," *Nuclear Instruments and Methods*

in Physics Research Section A: Accelerators, Spectrometers, Detectors and Associated Equipment, vol. 426, no. 1, pp. 1–15, 1999.

[72] G. Kramberger, V. Cindro, I. Mandić, M. Mikuž, and M. Zavrtanik, "Effective trapping time of electrons and holes in different silicon materials irradiated with neutrons, protons and pions," *Nuclear Instruments and Methods in Physics Research Section A: Accelerators, Spectrometers, Detectors and Associated Equipment*, vol. 481, no. 1, pp. 297–305, 2002.

[73] M. Moll, "Radiation Damage in Silicon Particle Detectors." `https://mmoll.web.cern.ch/thesis/`, note = "PhD Thesis, Universitat Hamburg", year = "1999";.

[74] N. C. et al., "Design optimization of ultra-fast silicon detectors," *Nuclear Instruments and Methods in Physics Research Section A: Accelerators, Spectrometers, Detectors and Associated Equipment*, vol. 796, pp. 141–148, 2015. Proceedings of the 10th International Conference on Radiation Effects on Semiconductor Materials Detectors and Devices.

[75] "LGADUtils: A C++ based framework for waveform analysis."

[76] L. Castillo García, "Overview of CNM LGAD results: Boron, Carbon-enriched and Gallium Si-on-Si wafers," *Proceedings from the* 12^{th} *Workshop on Picosecond Timing Detectors for Physics, to be published on Instruments: Special issue Timing Detectors*, vol. ,.

[77] "Particulars, advanced measurements systems,"

[78] G. Kramberger, "Advanced Transient Current Technique Systems," *PoS (Vertex 2014) 32*.

[79] U. H. S. Ritt F, R. Dinapoli, "Application of the DRS Chip for Fast Waveform Digitizing," *Nucl. Instr. and Meth. in Physics Research A,*, vol. 623,.

[80] tech. rep.

[81] H. Jansen *et al.*, "Performance of the EUDET-type beam telescopes," *EPJ Tech. Instrum.*, vol. 3, no. 1, p. 7, 2016.

[82] "EUTelescope Offline track reconstruction and DUT analysis software," tech. rep., 2010.

[83] G. Pellegrini, "Status of LGAD productions at CNM." RD50 Workshop, June 2017, Krakow.

[84] S. Hidalgo, "CNM activities on LGADs for ATLAS/CMS Timing Layers." RD50 Workshop, June 2018, Hamburg.

[85] E. Cavallaro, "Novel CMOS Devices for High Energy Physics and Medical Application." `https://www.tesisenred.net/handle/10803/666621#page=1`.

[86] G. Kramberger, "LGADs for Timing Detectors at HL-LHC."

[87] L. Castillo García, "A High-Granularity Timing Detector for the Phase-II upgrade of the ATLAS Calorimeter system: detector concept, description and R&D and beam test results," *2020 JINST 15 C09047.*

[88] S. Bharthuar, J. Ott, K. Helariutta, V. Litichevskyi, E. Brücken, A. Gädda, L. Martikainen, S. Kirschenmann, T. Naaranoja, and P. Luukka, "Study of interpad-gap of hpk 3.1 production lgads with transient current technique," *Nuclear Instruments and Methods in Physics Research Section A: Accelerators, Spectrometers, Detectors and Associated Equipment*, vol. 979, p. 164494, 2020.

[89] P. Skomina, "Studies of effective inter-pad distance of different HPK and FBK LGADs." RD50 Workshop, June 2021.

List of abbreviation and acronyms

AFP ATLAS Forward Proton

ALFA Absolute Luminosity For ATLAS

ALICE A Large Ion Collider Experiment

ALTIROC ATLAS LGAD Time Read Out Chip

APD Avalanche Photodiode

ASIC Application-Specific Integrated Circuit

ATLAS A Toroidal LHC ApparatuS

AU arbitrary units

BDT Boosted Decision Tree

BIST Barcelona Institute of Science and Technology

BNL Brookaven National Laboratory

BSM Beyond the Standard Model

BV bias voltage

CERN Conseil Europeen pour la recherche Nucleaire

CFD Constant Fraction Discriminator

CMS Compact Muon Solenoid

CNM Centro Nacional de Micróelectronica

CSC Cathode-Strip Chambers

DAQ data acquisition

DESY Deutsches Elektronen-Synchrotron

DUT Device Under Test

ECAL Electromagnetic CALorimeter

EMEC ElectroMagnetic End-Cap

EOC End Of Column

EW Electroweak interaction

FBK Fondazione Bruno Kessler

FCAL Forward Calorimeter

GBL General Broken Line

GR guard ring

IFAE Institut de Fisica d'Altes Energies

IHEP Institute of High Energy Physics

IME Institute of Microelectronics of the Chinese Academy of Sciences

HPK Hamamatsu Photonics

LHC Large Hadron Collider

LHCb Large Hadron Collider beauty

HCAL Hadronic CALorimeter

HEC End-Cap

HEP High Energy Physics

HGTD High Granularity Timing Detector

HL-LHC High Luminosity LHC

HS Hard Scattered

HV high voltage

IBL Insertable B-Layer

ID Inner Detector

IP Interaction Point

IP distance Inter Pad distance

IR InfraRed

ITk Inner Tracker

JSI Jožef Stefan Institute

JTE Junction Termination Extension

LAr Liquid Argon

LGAD Low Gain Avalanche Detector

LUCID LUminosity Cherenkov Integrating Detector

LV low voltage

MDT Monitored Drift Tube

mip *minimum ionizing particle*

MPV Most Probable Value

NDL National Nano Device Laboratory

NIEL Non-Ionizing Energy Loss

PS Proton Syncrotron

PU Pile Up

QCD Quantum cromodynamics

ROI Region of Interest

RPC Resistive Plate Chambers

SCT SemiConductor Tracker

SiPM Silicon Photo-Multiplier

SiT Silicon Tracker

SM Standard Model

SSB Spontaneous symmetry breaking

TCT Transient Current Technique

TDC Time to Digital Converter

TileCal Tile Calorimeter

TGC Thin Gap Chambers

TOA Time Of Arrival

TOE Time Of End

TOF Time Of Flight

TOT Tome Over Threshold

TRT Trasition Radiation Tracker

UCSC University of California Santa Cruz

UFSD Ultra Fast Silicon Detector

VBF Vector Boson Fusion

VBS Vector Boson Scattering

Chiara Grieco

Physicist

Passeig de Les Acacies 7, 5a 1a
Cerdanyola del Vallès, Barcelona. Spain
+39 3476854695
cgrieco@ifae.es, chiara.grieco@cern.ch, chiaragrieco90@gmail.com
ORCID: 0000-0002-3955-4399

Education

2017–Now **PhD in Physics**, *Institut de Fisica d'Altes Energies (IFAE)*, UAB Campus, Barcelona, Low Gain Avalanche Detectors for the ATLAS High Granularity Timing Detector.
Thesis director: S. Grinstein, L. Castillo García and M. del Pilar Casado Lechuga

Jul–Sept 2017 **Summer Intern**, *Fermi National Accelerator Laboratory*, Chicago, USA, Characterization of straw tubes for the Mu2e gas chamber.
Supervisor: M. Kargiantoulakis

2013–2017 **Master Degree in Physics**, *Università degli Studi di Napoli "Federico II"*, Naples, Italy, Performance studies of resistive pad MicroMegas prototype for high rate applications.
Thesis director: M. Alviggi and C. Di Donato

2009–2013 **Bachelor Degree in Physics**, *Università degli Studi di Napoli "Federico II"*, Naples, Italy, Characterization of a MicroMegas for the ATLAS upgrade.
Thesis director: M. Alviggi and C. Di Donato

Research activities

since 2017 **Member of the ATLAS Collaboration**.

Oct 2017–Now **PhD candidate in Physics**, *Institut de Fisica d'Altes Energies*, UAB Campus, Barcelona, Main supervisor: S. Grinstein.
Expected end date - June 2022

- Qualification task for ATLAS authorship:
  - Study of the performance of the Silicon Tracker of the ATLAS Forward Proton Detector
  - Participation in detector installation in the LHC tunnel and in several testbeams, calibration of sensors in the lab both at IFAE and CERN
  - Analysis of the results from LHC data taking for 2016 and 2017, presented in a conference with a poster and published in Proceeding of Science (Pos (LHCP18) 031)
- Deep involvement in test beams: preparation, setup, data taking, shifts, data analysis
- Preliminary Monte Carlo study of the effect of the HGTD detector effect in pile-up suppression for the process $Z \rightarrow \tau\tau + jets$ as the main background of the process $H \rightarrow \tau\tau$
- Mentoring of bachelor and master students

- Complete characterization of LGADs sensors for High Granularity Timing Detector:
  - Electrical characterization before and after irradiation
  - Stability studies to define the operational voltages for data taking
  - Preparation and use of a ^{90}Sr setup to measure the collected charge and time resolution of un-irradiated and irradiated single pad sensors and contribution to the development of the data analysis framework
  - Use of Transient-Current-Tecnique (TCT) setup for gain, collected charge and inter pad gap measurements for 2×2 LGAD arrays as a function of fluence and bias voltage
- Oral communication skills expressed in regular presentation in regular presentations in ATLAS (HGTD groups) and in various conferences and workshops
- Regular report to collaboration meetings

Jul–Sept 2017 **Summer Intern**, *Fermi National Accelerator Laboratory*, Chicago, USA, Supervisor: M. Kargiantoulakis.

- Characterization of Mu2e Tracker's straw tubes
- Study of the time resolution and energy spectrum (both data taking and analysis)
- A comparison between differences on the signal obtained with ^{90}Sr and ^{55}Fe has been carried out
- Study on the best way to connect preamplifiers to straw tubes in order to save time
- A preliminary analysis of crosstalk between neighbouring channels to study different approaches that could be used to reduce it

Oct 2016–Jul 2017 **Master Thesis student**, *Università degli Studi di Napoli "Federico II" and CERN*, Supervisors: M. Alviggi and C. Di Donato.

- Full characterization of a new prototype of MicroMegas gas detector with resistive pads readout developed in the RD51 collaboration at CERN
- Participation in test beam data taking at CERN with muon and pion beams
- Study of collected charge, spatial resolution at different beam angle incidency and efficiency of the detector as a function of the bias voltage
- Measurements with ^{55}Fe radioactive source of the transparency and gain have been carried out at CERN RD51 laboratory
- Analysis of all the results
- Regular report to group meetings

May-Oct 2013 **Bachelor Thesis student**, *Università degli Studi di Napoli "Federico II"*, Napoli, Italy, Supervisors: M. Alviggi and C. Di Donato.

- Full characterization of a MicroMegas detector for the ATLAS muon detector upgrade, developer by RD51 collaboration at CERN
- MBT0 and R20 prototypes were characterized with cosmic rays in University of Naples's laboratory. Properties studied as a function of voltage, using two different gas mixtures of Argon and CO_2.
- A study was performed to characterize clusters has the aim to use the MicroMegas as μ-TPC (Micro -Time Proportional Chamber). This work is a preliminary step for the study of clusters needed to perform a tracking inside the detector.

Publications

Main author

2 **Overview of CNM LGAD results: Boron Si-on-Si and epitaxial wafers**, *Proceeding of the 12TH International Conference on Position Sensitive Detectors (PSD12)*, Under review by JINST.

In this paper a full comparison between Si-on-Si and Low Resistivity Epitaxial wafers LGAD sensors will be given, comparin results for MIPs and laser measurements before and after irradiation

1 **ATLAS Forward Proton Detector**, *Proceeding of Science*, PoS (LHCP2018) 031.

The purpose of the AFP detector is to measure proton scattered at very small angles. In 2017 AFP participated in the ATLAS high-luminosity data taking. This paper presents the AFP detector and its performances during 2016 and 2017.

Direct contribution

9 **Performance in beam tests of irradiated Low Gain Avalanche Detectors for the ATLAS High Granularity Timing Detector**, Under review by JINST.

This paper presents results obtained with data recorded during HGTD test beams campaign during 2018 and 2019 both at CERN and DESY. Collected charge, time resolution, efficiency and charge uniformity are presented for CNM and HPK LGAD sensors.

8 **Characterization of Irradiated Boron, Carbon-Enriched and Gallium Si-on-Si Wafer Low Gain Avalanche Detectors**, *Proceeding of Workshop on pico-second timing detector for physics*, Instruments 2022, 6(1), 2.

In this paper, a full characterization of Boron, Carbon-enriched and Gallium doped LGAD sensors has been tested with Sr-90 radioactive source. Results for charge collection and time resolution are presented for different levels of irradiation

7 **A High-Granularity Timing Detector for the Phase-II upgrade of the ATLAS Calorimeter system: detector concept, description, R&D and beam test results**, *Proceeding of INSTR2020*, 2020 JINST 15 C09047.

In this paper, HGTD detector is presented and results from the R&D campaign for LGADs sensors are shown.

6 **Beam test results of NDL Low Gain Avalanche Detectors (LGAD)**, *Proceeding of HST12*, NIM A, Volume 978, November 2020, 164956.

This paper reports on beam test results for two proto-types LGADs (BV60 and BV170) developed for the HGTD and manufactured by the Institute of High Energy Physics (IHEP) of Chinese Academy of Sciences (CAS) collaborated with Novel Device Laboratory (NDL) of the Beijing Normal University.

5 **Radiation Campaign of HPK Prototype LGAD sensors for the High Granularity Timing Detector (HGTD)**, *Proceeding of HST12*, NIM A, Volume 979, November 2020, 164382.

Results of HPK LGADs sensors irradiated up to $3 \times 10^{15} n_{eq}/cm^2$ for collected charge and time resolution are presented.

4 **First characterization of 3D pixel detectors irradiated at extreme fluences**, *Proceeding of HST12*, NIM A, Volume 979, November 2020, 164458.

In this paper, 3D strip and pad detectors irradiated with neutrons up to a fluence of $3 \times 10^{17} n_{eq}/cm^2$ (1 MeV neutron equivalent) are characterised for the first time: the charge collection measurements with Transient Current Technique (TCT) are carried out at several voltages and the results are reported.

3 **Layout and Performance of HPK Prototype LGAD Sensors for the High-Granularity Timing Detector**, *Proceeding of HST12*, NIM A, Volume 980, November 2020, 164379.

The layout and performance of the various versions of LGAD prototypes produced by Hamamatsu (HPK) have been studied by the ATLAS Collaboration. The breakdown voltages, depletion voltages, inter-pad gaps, collected charge as well as the time resolution have been measured and the production yield of large size sensors has been evaluated.

2 **Performance of a Front End prototype ASIC for picosecond precision time measurements with LGAD sensors**, *2020 JINST 15 P07007*, Vol 15, July 2020.

This paper presents the results on the first prototype of a front-end ASIC, named ALTIROC0, which contains the analog stages (preamplifier and discriminator) of the read-out chip. The combined performance of the ASIC and the LGAD sensor, which was measured during a beam test campaign in October 2018 with pions of 120 GeV energy at the CERN SPS, is around 40 ps for all measured modules. All tested modules show good efficiency and time resolution uniformity.

1 **Small-pad resistive micromegas for operation at very high rates**, *TIPP 2017*, Proceedings of International Conference on Technology and Instrumentation in Particle Physics 2017., Springer Proceedings in Physics, vol 213. Pages 138–142.

A first prototype of Micromegas detector with readout and resistive pads connected by resistors embedded in an insulating layer, has been constructed at CERN and first performance studies are presented.

I am the author of 75 publications, a full list can be obtained in this link: `https://inspirehep.net/authors/1633990`.

Conferences, schools and workshop

Talks

14 October 2021 **ATLAS Collaboration Week "Towards Run 3"**, *CERN*, Low Gain Avalanche Detector for the ATLAS High Granularity Timing Detector.

12-17 September 2021 **The 12th International Conference on Position Sensitive Detectors**, *Birmingham, United Kingdom*, Overview of CNM LGAD results with B, Ga and C diffused Si-on-Si and epitaxial wafers.

27-31 January 2020 **8th Beam Telescope and Test Beam Workshop**, *Tbilisi, Georgia*, A High-Granularity Timing Detector for the Phase-II upgrade of the ALTAS Calorimeter system: beam test results.

14–15 March 2018 **ATLAS Forward Physics and Detector workshop**, *CERN, Geneva*, The Silicon Tracker of the ATLAS Forward Proton Detector.

Posters

13-17 May 2019 **6th EIRO Forum School of Intrumentation**, *ESA, Noordwijk, The Netherlands*, Low Gain Avalanche Detectors for ATLAS High Granularity Timing Detector.

4–9 June 2018 **The Sixth Annual Large Hadron Collider Physics conference (LHCP 2018)**, *Bologna, Italy*, ATLAS Forward Proton detector.

28 February 2018 **LHCC session**, *CERN, Geneva*, AFP - ATLAS Forward Proton detector.

Other

1 July 2021 **ATLAS Collaboration week**, *Phase II + NSW Upgrade Session*.
Convener of the session

Outreach

Feb 2022 **Dia de la dona i la ciencia**, *Outreach Talk for 100fiques BIST event*.
Agrupaciò Escolar Anselm Clave, Mollet Del Valles, Barcelona

Feb 2021 **Dia de la dona i la ciencia**, *From Universe to particle physics*.
Escola Sant Gervasi Cooperativa. Mollet del valles, Barcelona

Jan 2020 **Bojos per la Física (Beam Line for Schools)**, *Fast timing pixel detectors for High Energy Physics Experiments*.
IFAE Barcelona

Sept 2019 **Matì de la Recerca**, *CERN and LHC: exploring the energy frontier*.
Escola Pia Mataró. Matarò (Barcelona)

Feb 2019 **Dia de la dona i la ciencia**, *CERN and LHC: exploring the energy frontier*.
Institut Ramon Barbat i Miracle. Tarragona

May 2017 **Futuro remoto**.
Città della Scienza. Napoli

Software skills

Programming **C/C++**, *Good knowledge*.
phyton, *Basic*.
Editors **MS Office, LaTeX**.
Data analysis **ROOT**.
Other **Windows, Linux**.

Languages

Italian **Native**
English **Professional Proficiency** *Level B2 certificate from Cambridge University in July 2017*
Spanish **Professional Proficiency** *Level C1 certificate by Instituto Cervantes in December 2020*

Academic experiences

2020-2022 **Italian speaking training for spanish people**, *Barcelona, Spain*.
2019-2022 **University and high school support**, *Barcelona, Spain*.
2013–2017 **University support near three students**, *Napoli, Italy*.
2009–2015 **High school support with several students**, *Napoli, Italy*.

Work experience

2014–2018 **Employee in a bakery**.
2009–2011 **Appearance in TV series**.